JOURNAL OF CONDENSED MATTER NUCLEAR SCIENCE

Experiments and Methods in Cold Fusion

VOLUME 17, October 2015

JOURNAL OF CONDENSED MATTER NUCLEAR SCIENCE

Experiments and Methods in Cold Fusion

JOURNAL OF CONDENSED MATTER NUCLEAR SCIENCE

Volume 17, October 2015

ISSN 2227-3123

Orders, claims, author inquiries and journal inquiries

Please contact the Editor-in-Chief, CMNSEditor@iscmns.org or webmaster@iscmns.org

J. Condensed Matter Nucl. Sci. 17 (2015) 1–123
 ISSN 2227-3123

JOURNAL OF CONDENSED MATTER NUCLEAR SCIENCE

Volume 17 2015

CONTENTS

Editorial

This new volume of the Journal of Condensed Matter Nuclear Science gives us another chance at discovering new experimental work, and new developments in the theoretical aspects of this extraordinary science. All the pieces of the puzzles are not there yet, so that we cannot fully understand what makes all this possible. Is there one mechanism, or several ones? Nobody knows yet. It might take many more years of hard work with large institutions before a clear picture emerges, and all pieces of the puzzle fall in place. But the fun and the pleasure are still present after more than a quarter century, and for a scientist this is very satisfactory.

Sincerely,

Jean-Paul Biberian
(*Editor-in-Chief*)
October 2015

J. Condensed Matter Nucl. Sci. 17 (2015) 1–26

Research Article

Strained Layer Ferromagnetism in Transition Metals and its Impact Upon Low Energy Nuclear Reactions

Louis F. DeChiaro*
Naval Surface Warfare Center, 5493 Marple Road, Suite 156, Dahlgren, VA 22448, USA

Lawrence P. Forsley
Global Energy Corporation, Annandale, VA 22003, USA

Pamela Mosier-Boss
Space and Naval Warfare Systems Center (SPAWAR) Pacific, San Diego, CA 92152, USA

Abstract

Spin-polarized Density Functional Theory (DFT) calculations have been performed to model the lattice structures for the Transition Metal Group, Columns I and II, and a number of sp elements in the Periodic Table. Our results suggest that most of the transition metals can exhibit ferromagnetic ordering if the lattice is placed in sufficiently high tensile stress. These results are applied to the study of some layered structures employed by a number of Low Energy Nuclear Reaction (LENR) research teams and may help to explain some of the anomalous results and the difficulty in reproduction of those results.
 ISSN 2227-3123

Keywords: DFT, Epitaxial, Ferromagnetism, LENR

1. Introduction

Although much work remains to be done in the understanding and reduction to practice of Low Energy Nuclear Reactions (LENR), the body of experimental data accumulated over the past 25 years contains a wealth of clues to inspire and guide the LENR community. For example, since the early 1990s it has been known [1] that the amount of excess heat measured in a typical electrochemical LENR experiment can be increased by the appropriate application of a DC magnetic field. The Bockris Group at Texas A&M also reported [1] increased excess heat when their cells were stimulated with very high frequency (VHF) and ultra high frequency (UHF) electromagnetic fields. Finally, Letts and Hagelstein [2] reported excess heat when they focused the beams of two visible frequency lasers upon the cathodes

*E-mail: louis.dechiaro@navy.mil; Tel.: 1-540-653-8040.

 ISSN 2227-3123

in their Fleischmann–Pons cells, especially when the frequency difference between the two lasers corresponded to the THz atomic vibrational frequencies preferred by the PdH and PdD lattices. They also found that the best results were obtained when a DC magnetic field measuring about 700 Gauss was applied across the face of their Pd foil cathodes. As a result of these observations, a number of LENR community members believe that there are profound connections among LENR phenomena, atomic vibrations, and electromagnetic fields.

Experimental evidence also suggests that certain metal oxides may have a role in the LENR mechanism(s). For example, as we discuss in detail below, the layered structures used successfully by Iwamura et al. [3] contain thin films of CaO in addition to the expected Pd. And one of the well-known Arata structures [4] contains nanoparticles of Pd embedded in a nonconducting matrix of zirconium dioxide. However, the choice of oxide is apparently not arbitrary, because the Iwamura team also reported that using thin films of MgO instead of CaO yielded negative experimental results.

This paper presents the results of Density Functional Theory (DFT) computations performed to study itinerant ferromagnetism in elemental transition metals and strained layer superlattices of binary composition. Section 2 provides a short introduction to Density Functional Theory. Section 3 discusses the basic results, including the cross checks done to ensure credibility and physicality of the DFT output, extraction of values for the equilibrium lattice constant, and the lifting of the degeneracy between spin-up and spin-down electron energy eigenvalues. Section 4 presents our results on the ground state lattice energy and absolute magnetization versus lattice constant and introduces the concept of normalized asymptotic magnetization per unpaired valence electron spin. Section 5 discusses the experimental results reported by the Mitsubishi Heavy Industries (MHI) team led by Yasuhiro Iwamura and interprets them in light of the DFT spin-polarized results of this work. Section 6 presents the results of a DFT supercell study of the CaO:Pd interface and illustrates the degree of spin polarization of the various atomic species in the structure. Section 7 discusses the experimental results of Yoshiaki Arata in light of our DFT findings, and Section 8 contains the results of a DFT supercell study of the ZrO_2:Pd interface that may affect the Arata results in roughly the same way that the CaO:Pd interface affects the MHI results. Finally, Section 9 summarizes our results.

2. Density Functional Theory

Density Functional Theory (DFT) is a mathematical procedure that can be used to simulate small clusters of atoms and calculate from first principles (with essentially no adjustable parameters) many important physical properties such as ground state energy, lattice stress, electronic structure, phonon dispersion curves, and many more, given only the positions and atomic species for each atom in the cluster. Software implementing DFT makes use of the periodic symmetry of an ordered crystal lattice so that a finite-scope calculation based on a single unit cell of an ordered lattice can often produce results that approximate the bulk properties of a macroscopic sample of the material.

The algorithms used in such calculations originated in a mathematical proof in which Hohenberg and Kohn [5] presented a variational principle for obtaining the ground state energy of an electronic system, a principle that introduces a universal functional of the electron density $F[n(\vec{r})]$. Once this functional is computed by whatever means, the ground state energy in an arbitrary external potential can be obtained. The following year, Kohn and Sham [6] published a seminal paper in which they derived a highly nonlinear partial differential equation system that can be solved with a self-consistent, iterative algorithm to calculate the electron density versus position in an atomic system under study.

Several software packages implementing DFT are available. For this particular project, we chose Quantum Espresso, mainly because it has an excellent track record, it is available at no cost through the Web, and one of us (DeChiaro) had acquired several years' prior experience using Espresso in the academic domain. Further details, including the

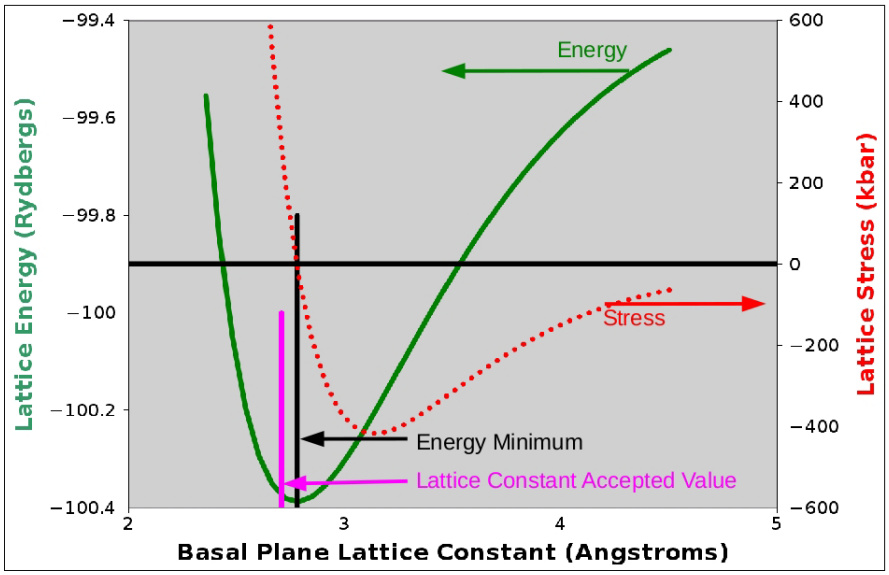

Figure 1. Lattice energy (left vertical axis) and stress (right vertical axis) curves vs. lattice constant for the paramagnetic solution of the transition metal ruthenium. Computed energy points are connected by solid green straight line segments, while the computed stress points are connected by dotted red straight line segments. The equilibrium lattice constant was found by fitting the three lowest energy points to a second order polynomial and then solving this to find the point of zero slope. The error between this value and the accepted value of lattice constant is about 2.7%.

algorithms used to solve the Kohn–Sham equation in a self-consistent iterative manner, are available in Giannozzi et al. [7], and the interested reader is directed to this publication.

Users of such software packages must be aware of a number of limitations and caveats. Each atomic species is represented by a pseudopotential file that approximates the effects of the atomic nucleus and the core electrons upon the valence electrons – but without the mathematically problematic "wiggles" and frequent zero crossings exhibited by the actual wave function. The generation of such pseudopotential files requires a parametrization procedure that vastly reduces the computational resources needed but also introduces certain errors. In general, we have obtained reasonably good results when using pseudopotential files parametrized with the Perdew, Becke, and Ernzerhof (PBE) generalized gradient approximation. However, in some cases, we employed Perdew-Zunger local density approximation pseudopotentials, generally because PBE pseudopotentials either might not be available for all elements or because the PZ potentials provide better agreement with experiment for some observable quantities. In any event, one should state which of the several different types of pseudopotential files were used, and these can be found in Appendix A for this work.

3. Basic Results: Extraction of the Lattice Constant

The ultimate success or failure of any computational model rests upon the degree to which it can accurately predict observable quantities such as the lattice constant. The DFT has had good success in accurately modeling many of the atoms in the Periodic Table, provided that one uses pseudopotential files that have been carefully tested and have good transferability characteristics. The two sections of the Table where the DFT success has been quite limited are the Lanthanide and the Actinide Series, primarily due to the difficulty in modeling the incomplete f-shells of those series.

Figure 1 shows the computed results for ruthenium, a typical example of a well-behaved species near the center of the Transition Metal Group. The reader will note that the extracted value of lattice constant corresponding to the energy minimum is in excellent agreement with the zero crossing of the lattice stress curve. This is a necessary but not sufficient condition to ensure that the calculated results are physically meaningful. One of the other important conditions that must be satisfied is a reasonable agreement (less than 5% error) between the extracted value of equilibrium lattice constant and the accepted value. Some of the elements crystallize in multiple lattice types and/or are characterized by multiple c/a ratios in the literature, however in all cases it was possible to find a structure that was stable and yielded good agreement between computed and accepted values of lattice constant. For most of the elements, we employed values from Wyckoff for the accepted lattice constants. Appendix A contains a table that compares the computed and accepted values of lattice constant for all the atomic species in this study. The mean absolute value of all these errors is about 1.565%, confirming the published results that DFT is reasonably successful in modeling the behavior of most of the atomic species of the Periodic Table in their elemental lattice form.

One further caveat that should be borne in mind when interpreting these results has to do with the crystal structures. We employed the lattice types, space groups, and atomic coordinates as specified in Wyckoff for one of the structures

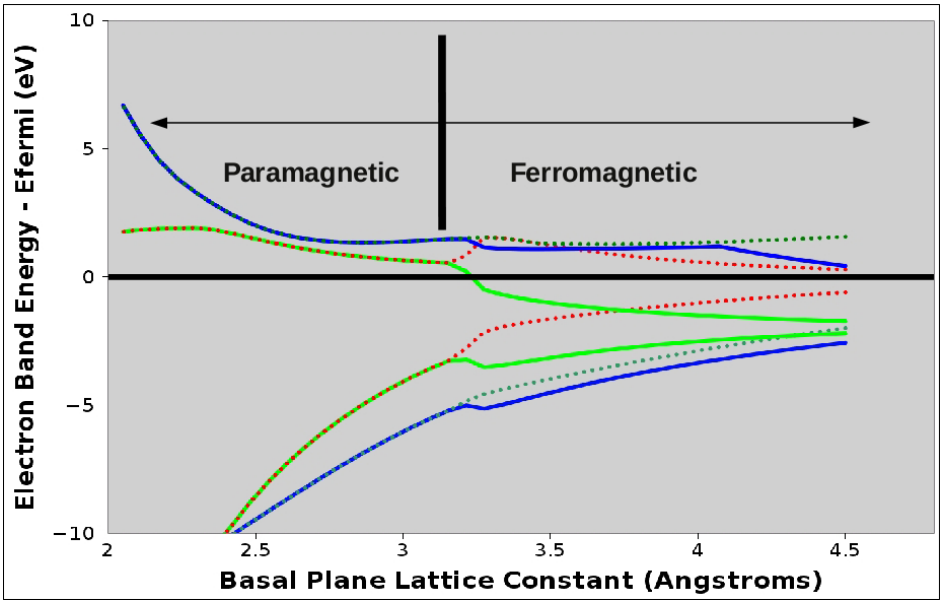

Figure 2. Electron energy relative to the Fermi level vs. lattice constant for the ferromagnetic solution of the transition metal ruthenium. Computed points on the spin-up bands are connected by solid straight line segments, while the points on the spin-down bands are connected by dotted straight line segments. The light green and red curves illustrate the two bands lying closest to the Fermi level, while the dark green and blue curves illustrate the two bands lying furthest from the Fermi level.

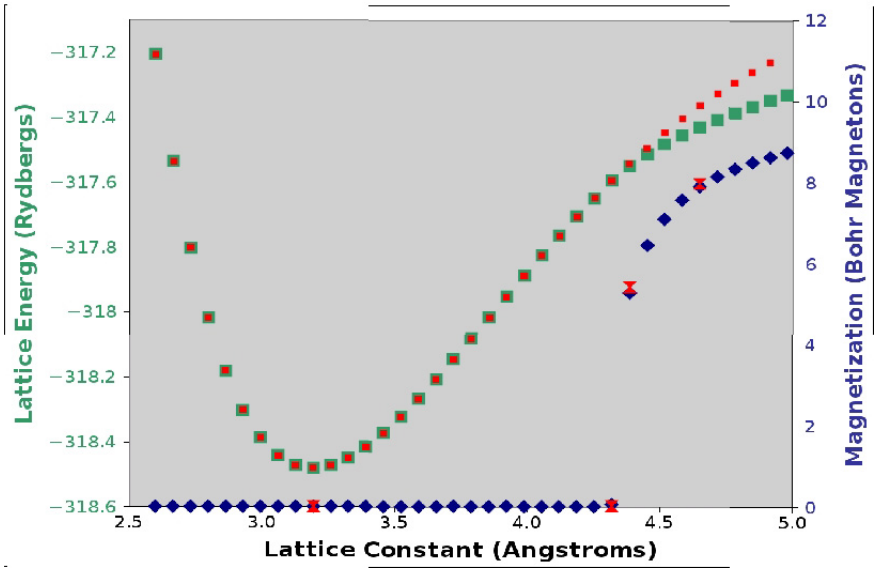

Figure 3. Ground state lattice energy (left vertical axis) in Rydbergs and absolute magnetization (right vertical axis) for tungsten versus BCC lattice constant in Angstroms. The green squares show the ground state energy for the ferromagnetic solution, while the small red squares show the energy for the paramagnetic solution. The blue diamonds show absolute magnetization in Bohr Magnetons per unit cell, and the red hour-glass symbols show magnetization values at key points calculated with a very dense mesh of k points to ensure maximum accuracy.

that is in equilibrium at room temperature. The abscissas of the plots presented in this work include values of lattice constant corresponding to high tensile stress. Such stress represents a departure from equilibrium conditions that will significantly elevate the lattice energy. All materials are limited in the associated strain they can support without physical destruction of the lattice. Atomic systems also possess a number of mechanisms to reduce their energy, even when the strain lies below the threshold for catastrophic destruction. These include the nucleation of lattice defects such as dislocations, the possibility of a phase transition to a different lattice type and space group, and even the growth of whiskers (for which high purity silver and tin are both notorious). Some of these phase transitions are accompanied by physical displacement of the atoms, for example, when a face-centered cubic (FCC) lattice undergoes a tetragonal distortion as the result of an applied stress field. Other phase transitions, however, do not displace the atoms but instead cause a change in electronic structure that gives rise to a collective phenomenon known as itinerant ferromagnetism. Materials that exhibit this latter type of phase transition are characterized by a critical threshold value of lattice constant at which the numerical solution to the Kohn–Sham equation suddenly bifurcates into two distinct solutions. One of these is paramagnetic and joins continuously and smoothly with the paramagnetic behavior found below the threshold. However, the other solution is ferromagnetic in nature and may exhibit discontinuities in the derivatives of certain parameters as it joins with the paramagnetic solution at the threshold value of lattice constant. One of those parameters is the electronic band structure, which bifurcates at the threshold into two distinct sets of energy bands, one for the spin-up electrons, the other for the spin-down electrons. This bifurcation usually does not affect the deep core states, but will significantly perturb the energy bands lying near the Fermi surface. To illustrate an example of this behavior, we return to the case of ruthenium.

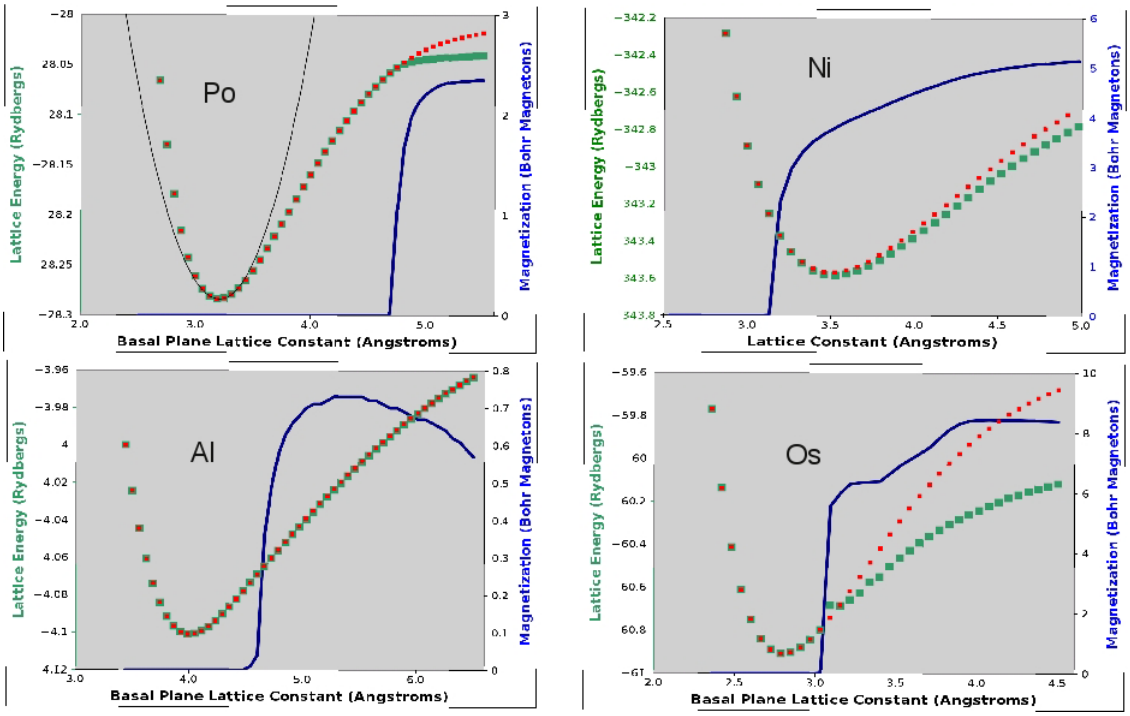

Figure 4. Ground state lattice energy (left vertical axes) in Rydbergs and absolute magnetization (right vertical axes) for polonium (upper left), nickel (upper right), aluminum (lower left), and osmium (lower right) versus lattice constant in Angstroms. Once again, the green squares show the ground state energies for the ferromagnetic solutions, while the small red squares show the energies for the paramagnetic solutions. The dark blue curves show absolute magnetizations in Bohr Magnetons per unit cell, and the thin black parabolic line on the polonium plot shows the regression polynomial that was fitted to the several points near the energy minimum and used to extract a value for the equilibrium lattice constant.

Figure 2 shows the electron energy eigenvalues (relative to the Fermi energy) plotted as a function of lattice constant for four spin-up and four spin-down energy bands at the center of the Brillouin zone ($k = 0$) where the electron momentum vanishes. Two of these energy bands lie below the Fermi surface, while the other two lie above it. The two bands lying closest to the Fermi surface are shown plotted in brighter colors, while the two lying furthest are plotted in darker colors. It is evident that the two brighter colored plots showing the bands lying closest to the Fermi surface exhibit considerably more splitting than the bands lying further from the surface.

4. Lattice Ground State Energy and Absolute Magnetization

The two most important lattice parameters to be considered in this work are the ground state energy and the magnetization of the lattice. The overall lattice ground state energy is the primary quantity used by Quantum Espresso in governing the self-consistent field (SCF) iterative solution of the Kohn–Sham equation. This ground state energy is normally given in units of Rydbergs (the energy level for the solitary 1s electron in hydrogen is -1.0 Rydberg or -13.6 eV), and the SCF iteration normally proceeds until the estimated iterative increment in this quantity falls below a user-specified threshold that is typically 10^{-8} Rydberg. Magnetization is calculated as the spin-up minus the spin-down charge density versus position in the three dimensional working volume of the structure specified by the user in the input file. These two spin-polarized charge densities are normally identically equal in materials that have no absolute magnetization

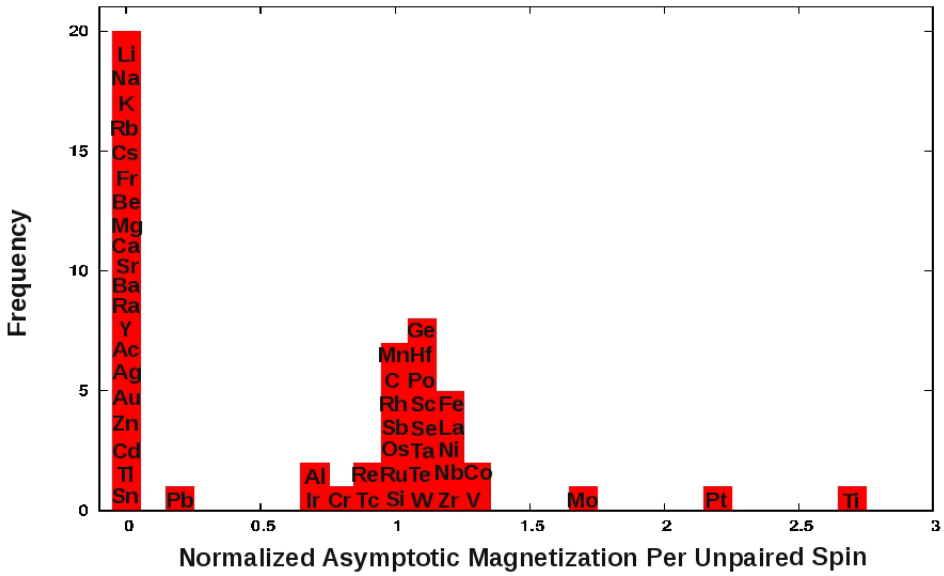

Figure 5. Histogram plot showing the distribution of the computed asymptotic magnetization for the elements after normalization to yield the absolute magnetization per unpaired electron spin. The width of each numerical bin is 0.1, and each vertical bar contains the chemical symbols of the various elements whose normalized asymptotic magnetizations fall in its respective bin. The tall bar at 0 on the left shows the 20 elements whose outermost electron shells contain only s electrons; they do not develop ferromagnetic activity when placed under high tensile stress.

and where the spin-up and spin-down electron energies are everywhere equal. However, as can be seen in Fig. 2, one of the spin-up energy bands crosses the Fermi surface at a lattice constant value near 3.2Å, while the corresponding spin-down band remains above the surface.

Since the electron occupation numbers (as specified by the Fermi–Dirac distribution) rapidly drop toward zero as one crosses the Fermi Surface from below, the spin-up band will be filled at $k = 0$ while the spin-down band will not be filled. Thus, we expect that the system will begin to show a nonvanishing magnetization, and the ground state lattice energies for the paramagnetic and the ferromagnetic solutions may begin to diverge from one another. This behavior is illustrated in Fig. 3, where we present ground state energies for the paramagnetic and ferromagnetic solutions and absolute magnetization (proportional to $\int \mid \rho_{\text{up}} - \rho_{\text{down}} \mid \mathrm{d}^3 V$) versus lattice constant for the transition metal tungsten.

Initial conditions specified in the input files were chosen to encourage the system to converge to either the paramagnetic or the ferromagnetic solution. For all points to the left of the threshold value of about 4.32Å, the ferromagnetic solution does not exist, and the code always converged to the paramagnetic solution, regardless of initial conditions. However, for points above threshold, the two solutions coexist, and the choice of initial conditions determines which solution will "attract" the convergence of the algorithm. The reader will note that at the threshold, we see the energy curves for the two solutions begin to diverge. The difference between the two grows monotonically with increasing lattice constant for tungsten in the range of lattice constants explored in this work. Not all atomic species exhibited this monotonic increase. However in nearly all cases, the ferromagnetic energy was lower than the paramagnetic energy at the same lattice constant, suggesting that the ferromagnetic state is the energetically preferred one. The very few exceptions involve one or two points close to the thresholds where the numerical fluctuations are very large for some elements. This can cause difficulty in convergence and the possibility of critical fluctuation noise in the results, a situation very common in the study of thermodynamic phase transitions. Figure 4 shows results for four other elements, drawn

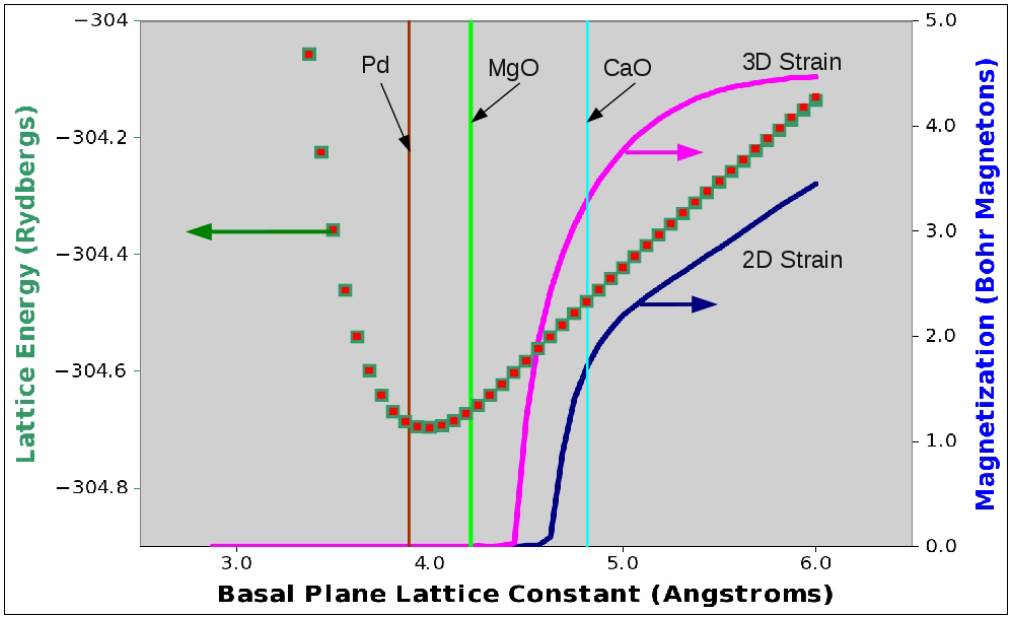

Figure 6. Simultaneous plots showing the ferromagnetic (green squares) and paramagnetic (small red squares) energy curve for Pd on the left vertical axis, the magnetization of Pd on the right vertical axis when strained in two and three dimensions, and the equilibrium lattice constants for Pd, MgO and CaO – all versus lattice constant.

from both the transition metals (Ni and Os) and the so-called sp elements (Al and Po) where the outermost valence electrons in the isolated atoms lie in p orbitals. We see that the general trend shows a rapid increase in magnetization at the threshold, a saturation at higher lattice constants, and in some cases, a decrease in magnetization at very high lattice constants as seen in the Al curves. The one element from the figure that is known to be ferromagnetic under normal conditions is nickel, and it is no coincidence that the threshold for bifurcation of the energy surface lies below the equilibrium lattice constant. Finally, we note that the 4 elements shown in the figure exhibit considerable differences in the rates at which the paramagnetic and ferromagnetic energy surfaces diverge above threshold. The ratio between this energy difference and kT is likely to have a strong influence upon the rate at which the higher-energy paramagnetic state is thermally populated at any given absolute temperature above 0K.

In the limit as the lattice constant approaches infinity, the behavior of the system approaches that of isolated atoms, for which the intrinsic electronic magnetic moment (neglecting the contribution caused by the orbital motion of the electrons) will be equal to the number of unpaired electron spins multiplied by the Bohr Magneton. In this limit, we would expect the total moment for a system of N decoupled identical atoms to be equal to the product of N, the number of unpaired spins in each atom, and the Bohr magneton. This implies that if we take the total moment of the system and normalize it by dividing by this quantity, we should obtain 1.0 Bohr magnetons per unpaired spin. The magnetization plots shown in Fig. 4 encompass about one order of magnitude dynamic range for the peak magnetizations computed in this work. Approximately the same can be said for the variation across the Periodic Table in the product of N and the number of unpaired spins. If we suspect these two quantities to be correlated in real elemental lattices, then we should be able to extract or extrapolate the maximum magnetic moment from each of the plots, perform the normalization, and obtain a result close to 1.0 in the absence of competing effects. This exercise was performed for each of the atomic species in this study. However, before presenting the results, we should add that it would be surprising if the

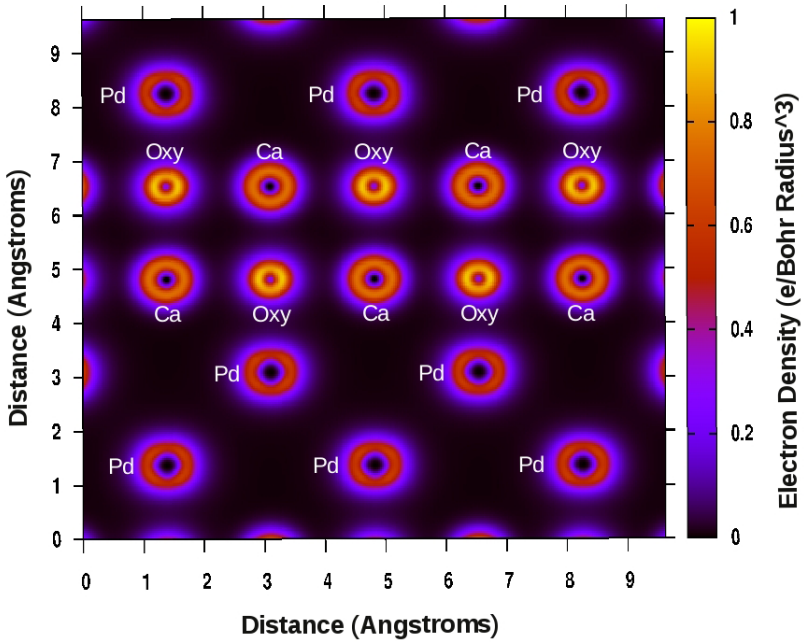

Figure 7. False color cross-sectional image of total charge density taken parallel to the *YZ* plane (thus along the [100] crystal plane) and intersecting the CaO:Pd supercell. Individual atoms are labeled for clarity. This image should be used to locate the various atoms and simplify the interpretation of the more complex spin-polarized image shown in Fig. 8.

magnetic moment contributions resulting from the electron orbital angular momenta were found to have no impact upon the results. In fact, our calculations indicate that in one respect the orbital angular momentum quantum number does impact the magnetizations of the elemental metals and semi-metals. Within the limits of computational precision caused by the numerical fluctuations, the magnetizations of all Column I and Column II atoms (whose outermost electron shells are comprised entirely of s-state electrons with vanishing orbital angular momenta) are exactly zero. The same can be said for the atoms lying along the extreme right hand edge of the Transition Metal Group (Zn, Cd, and Hg). We studied the first two of these and obtained zero magnetization and no ferromagnetic solutions to the Kohn-Sham Equation for any lattice constant lying in the range of values studied herein. Most of the remaining transition metals we studied (with the sole exceptions of Y, Ac, Ag, and Au) and some of the sp elements exhibited nonzero values of magnetization for sufficiently large values of lattice constant. Figure 5 contains a plot of the probability density function censored to the form of a histogram for the distribution of normalized peak magnetizations per unpaired spin.

With the exceptions of the elements whose outermost electron shell contains only s electrons, most of the elements produced normalized asymptotic magnetizations that cluster fairly close to the expected value of 1.0. The element Pd could not be plotted on Fig. 5 because the outermost shell is the 4d shell, and it is completely filled in the ground state. Thus there are no unpaired spins at all, unless the lattice can be sufficiently excited to cause some of the atoms to occupy the low-lying first excited state corresponding to an electronic configuration of 4d9 5s1. If this were the case, then Pd would appear in the distribution at 1.125 in the tallest of the histogram bars clustered near 1.0.

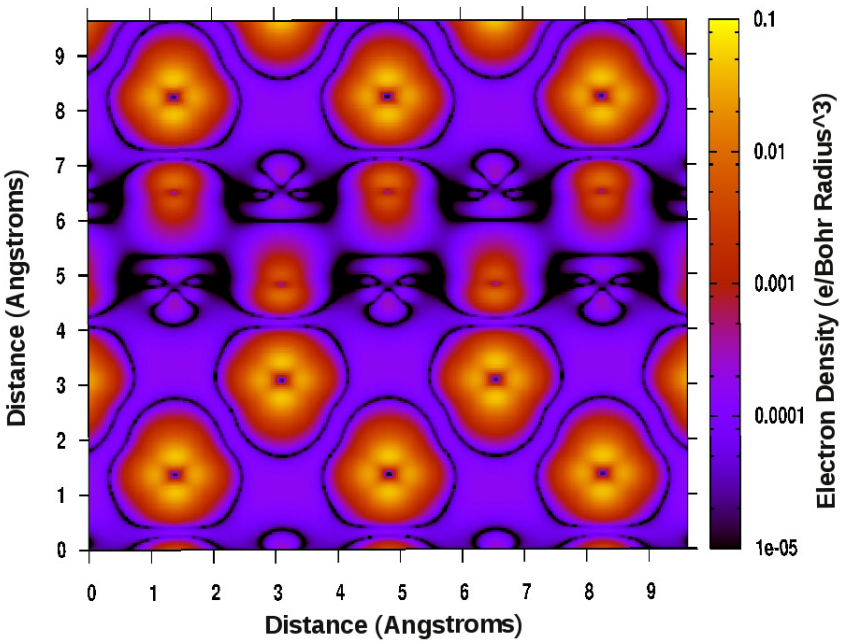

Figure 8. False color cross-sectional image of absolute value of spin-up minus spin-down charge density taken parallel to the *YZ* plane (along the [100] crystal plane) and intersecting the CaO:Pd supercell. A logarithmic scale was used to grade the colors in order to show all the atoms, including the most inactive ones. Atoms that are highly spin polarized will be bright in this image, while totally inactive atoms will appear black.

5. Application to the Iwamura Structure

From 1996 to 2005 results from a series of key LENR experiments were published by a team of workers at Mitsubishi Heavy Industries under the direction of Yasuhiro Iwamura. These results include the reported observation of excess heat and several types of nuclear transmutations that change the atomic number of their reactant species by +4 and the atomic mass number by +8 when deuterium is forced under a pressure difference of about 1.7 atm. through an ABABAB sandwich structure consisting of alternating layers of Pd and a light metal oxide having the same FCC crystal structure as Pd. Some of the Iwamura results were recently confirmed by an independent team at Toyota Central Research Laboratories [9] and published in the October, 2013 Issue of *Japanese J. Appl. Phys.* Iwamura et al. also presented some of their key findings at ICCF-11 in Marseilles, France, in 2004. Among these findings are the following observations:

(1) Transmutations are not observed when the light metal oxide layers are absent from the sandwich structure.
(2) Transmutations are not observed unless the sandwich structure is permeated with D_2 under pressure.
(3) Transmutations are not observed if the light isotope of hydrogen is used instead of deuterium.
(4) Transmutations are only observed for some chemical compositions of the light metal oxide layers and not others. In particular, when Pd is used as the transition metal layer, CaO was observed to function well, while MgO (another oxide with the same crystal structure) did not function at all.

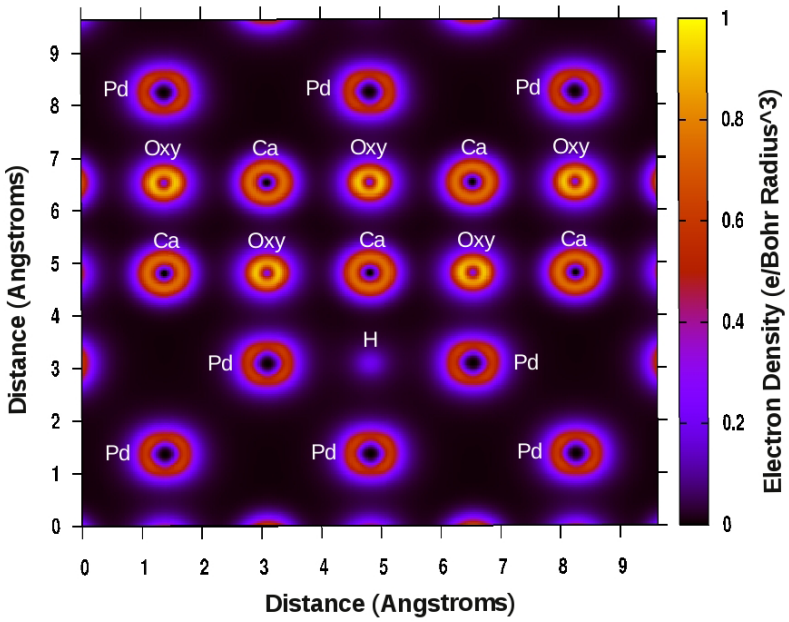

Figure 9. False color image of total charge density (in units of electronic charge per cubic Bohr radius) versus position after a single hydrogen atom has been added at the octahedral site just below the calcium atom near the geometric center of the image. The hydrogen atom can be seen as a small, purple sphere.

The Mitsubishi team suggested that two possible roles of the oxide layers are to increase the deuterium density within the structure and to modify the surface electronic band structure of the Pd in some way that would favor the LENR reactions. Based upon the results of our spin-polarized DFT studies, it is now possible to propose a third role for the oxide layers: to apply a tensile stress to the Pd films in two dimensions that is of sufficient magnitude to drive at least some fraction of the Pd atoms into their ferromagnetic state. If this third hypothesis is experimentally confirmed, we would then interpret the sandwich structure as a long period strained layer superlattice that is very similar (except for its longer period) to those now widely employed by the integrated circuit and optoelectronic component industries to create new materials with novel and highly optimized properties.

Figure 6 presents results that help explain how the strained layer superlattice hypothesis functions. The accepted value for the Pd lattice constant is shown as a brown vertical line in the figure. As we might hope, this value lies very close to the global minimum in the energy curves. The lattice constant for MgO as shown by the light green line in the figure is larger than that of Pd, but not sufficiently large to drive the Pd into its ferromagnetic state when the sandwich structure is epitaxially grown so that some fraction of the Pd is forced to take on the lattice constant of the underlying MgO. Thus, *if* the LENR reaction were to depend upon the presence of a large magnetic field, we would predict that the sandwich structures made from MgO will not perform any better than those without any metal oxide layers at all – in agreement with the experimental observations. On the other hand, the lattice constant of CaO (4.815 Å) is considerably larger than that of MgO, as one can see in the light blue vertical line in the figure. In fact, the lattice constant of CaO is sufficiently large that if we get some epitaxial growth of the Pd on top of the CaO so that the Pd is forced to assume the CaO lattice constant, we expect the Pd to be driven well into its ferromagnetic state, regardless of whether the tensile stress is applied in 3 or only 2 physical dimensions. This is also in excellent agreement with experiment.

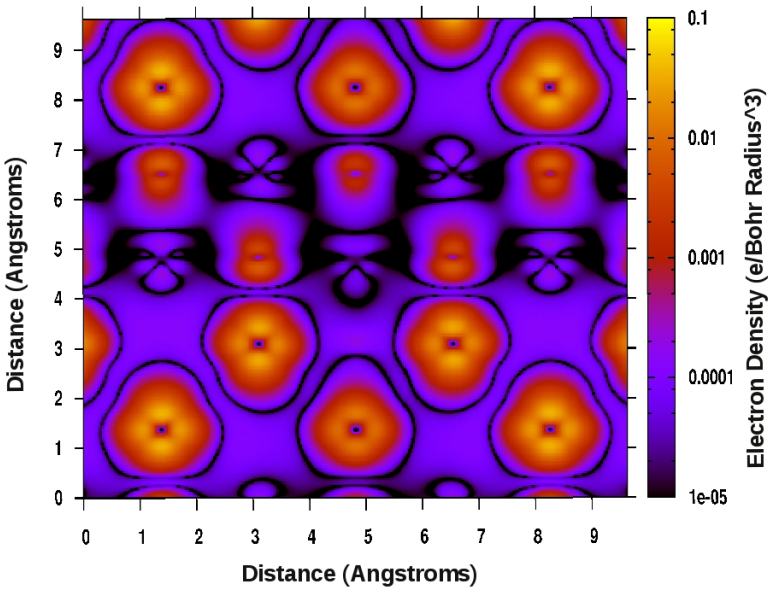

Figure 10. False color cross-sectional image of absolute value of spin-up minus spin-down charge density after adding the single hydrogen atom. The hydrogen is barely visible just below the central Ca atom and above the center-most Pd atom. Please note that the "eyes" of the central Ca atom are now missing, and the brightness of the Pd atom immediately below the hydrogen and the oxygen directly above the hydrogen is smaller than the other Pd and oxygen atoms, respectively.

As with any hypothesis, further experiments would be necessary either to confirm or refute it. However, if confirmation is obtained, the insight gained could illuminate the path toward technological exploitation. Among other things, it could provide guidance for those seeking other metal insulating compounds with even larger lattice constants (such as BaF_2, for example, with a lattice constant near 6.2 Å). There is, of course, a maximum percentage lattice constant mismatch between the two materials (typically only a few percent) that can be tolerated without negative effects such as delamination of the epitaxial film, nucleation of dislocations or other crystallographic defects, and thermal expansion problems, to name just a few. Thus the quest for the optimum set of materials for any given application will be far from trivial.

6. DFT Studies of the CaO:Pd and MgO:Pd Interfaces

The lattice structures for most of the elemental metals contain a basis with only one or at most two atoms. This makes it possible to study such structures even when limited to a single core processor. However, the study of an interface between two materials usually requires construction of a much larger system containing at least several tens of atoms. Fortunately, the authors have access to a desktop Linux machine with 16 cores and 16 GB of RAM, establishing an upper limit on the accessible systems at about 75 atoms. We therefore modeled the CaO:Pd interface by constructing a supercell of $2 \times 2 \times 2$ FCC unit cells, the bottom 4 of which are composed of Pd and the top 4 of CaO. The overall lattice constant for the supercell was set at twice the value for a single cell of CaO. This should be reasonably accurate in the limit as the CaO layer becomes much thicker than the Pd layer. Quantum Espresso saves both the many electron wave function and the spin-polarized charge density as arrays defined on a discretized three dimensional mesh. The post-processing tool makes it straightforward to sample the wave function and charge density on any user-specified line

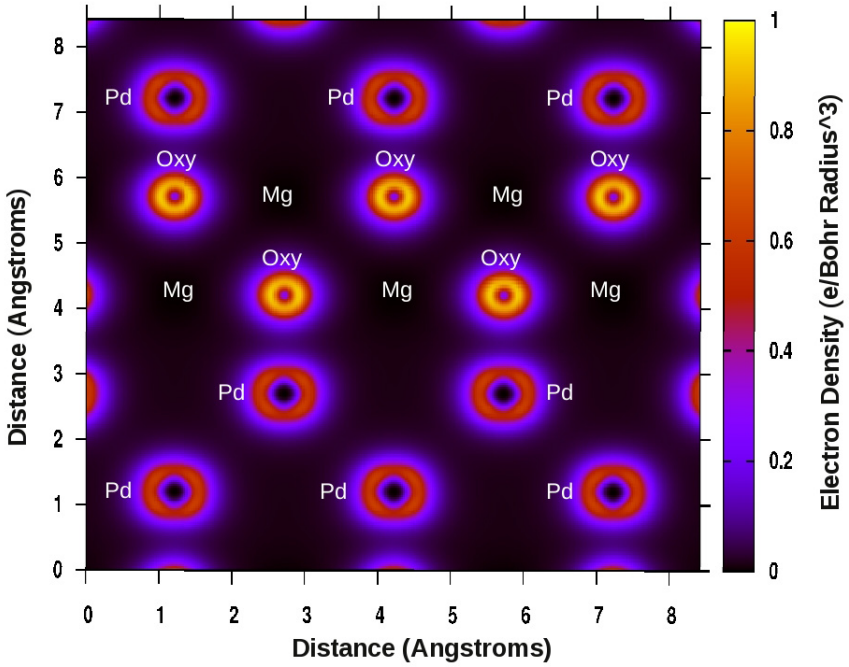

Figure 11. False color cross-sectional image of total charge taken parallel to the *YZ* plane (along the [100] crystal plane)and intersecting the MgO:Pd supercell. Individual atoms are labelled for clarity. The Mg atoms are not visible because they are represented in the pseudopotential file only by their two valence electrons, which have been completely absorbed into the electronic band structure of the material and are no longer localized around the ion core. The Mg labels show where the ion cores lie.

or plane intersecting the volume of the system under study. When combined with a full featured plotting program such as Gnuplot, the user can generate false color images showing total charge density versus position, spin up minus spin down charge density versus position, and many other useful parameters.

Figure 7 shows a false color cross-sectional image showing total charge density through the *YZ* ([100]) plane of the supercell. Individual atoms are labeled to facilitate their species identification. The atoms appear as doughnut-shaped objects because the pseudopotential files used to represent each atom contain only the outermost valence electrons, the ones most directly involved in the creation of chemical bonds and the determination of most physical properties of materials. Figure 8 shows a false color cross-sectional image through exactly the same set of atoms, however here we are plotting the absolute value of spin-up minus spin-down charge density as a function of position with a logarithmic color scale in order to assess which atoms are the most ferromagnetically active. The largest and brightest atoms in Fig. 8 are Pd, and the spin polarized image shows evidence of the four-fold symmetry of the FCC lattice. We thus appreciate that the Pd has indeed become spin polarized by virtue of the tensile stress applied by the CaO lattice with which the Pd is in contact.

The thin black regions surrounding each Pd atom represent places where the spin polarization goes through a zero and switches algebraic sign. Since the straight line path from one Pd to another passes through exactly two of these sign changes, we see that all the Pd are ordered ferromagnetically with respect to one another. The smaller of the bright atoms are the oxygens, and we note that these are also spin polarized and ferromagnetically ordered relative to the Pd

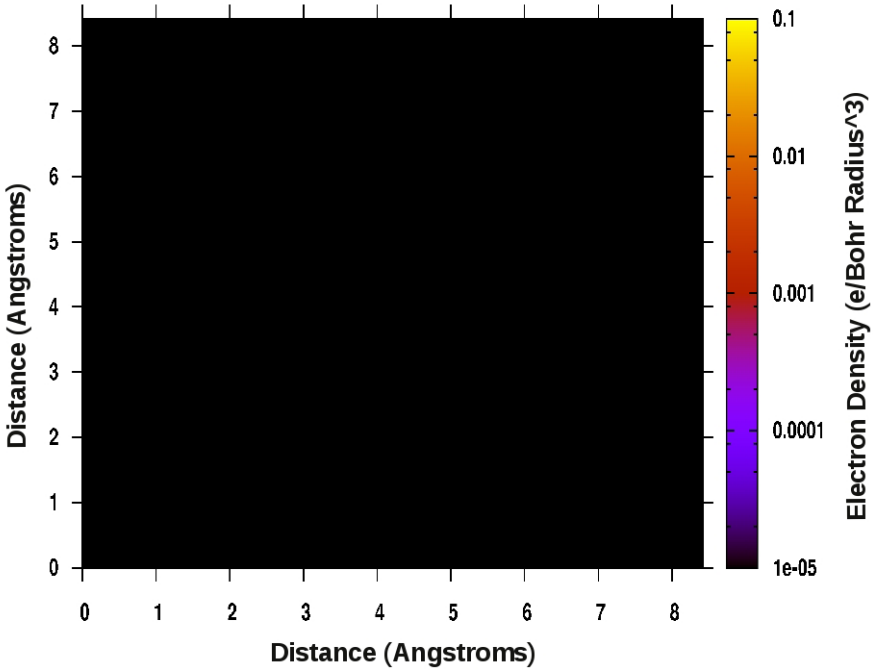

Figure 12. False color cross-sectional image of absolute value of spin-up minus spin-down charge density taken parallel to the *YZ* plane (along the [100] crystal plane) and intersecting the MgO:Pd supercell. The same logarithmic scale as presented in Figs. 8 and 10 was used to grade the colors. The entire image is black, confirming our prediction that the structure does not show any ferromagnetic ordering.

atoms. We also note that all the Pd atoms are equally magnetized. The shape of the spin polarized regions of the oxygen atoms is somewhat reminiscent of "Fig. 8" shape of the p orbitals that serve as the outermost occupied orbitals for the oxygen atoms. Finally, the least magnetically active of the three atomic species in Fig. 8 is the sublattice of calcium atoms. These atoms can easily be distinguished from the other species by their faint resemblance to the face of a masked and bearded burglar. The very low level of magnetic activity for the Ca atoms is consistent with our monatomic results for calcium showing zero spin polarization for all of Columns I and II elements.

In order for the CaO:Pd layered structure to be technologically useful for performing transmutations, one must permeate the structure with deuterium under a modest pressure differential. It is therefore of interest to seek some insight into how the structure will change when the octahedral sites on the Pd layers are occupied by hydrogen atoms. The minimum perturbation possible involves the addition of just one hydrogen atom, and the most aesthetically-appealing place to add this atom is immediately above the center-most Pd atom. Figure 9 shows the total electron density false color image of the CaO:Pd structure with the single added hydrogen, and Fig. 10 shows the corresponding spin-polarized image.

Figures 7–10 are in good agreement with the prediction that the CaO:Pd structure can be expected to show itinerant ferromagnetic ordering. Equally important, however, is the exploration of the MgO:Pd structure. If the results of Fig. 6 are in fact correct, then we expect that a DFT study of the MgO:Pd structure with the supercell lattice constant set to twice the equilibrium value for MgO (4.211 Å) should result in no observable ferromagnetic ordering. Figures 11 and 12 show the results of the MgO:Pd calculation. Figure 11 shows a false color image of the total electron density vs. position in the *YZ* ([100]) plane at $x = 0$, and Fig. 12 shows an image of the spin-up minus spin-down charge

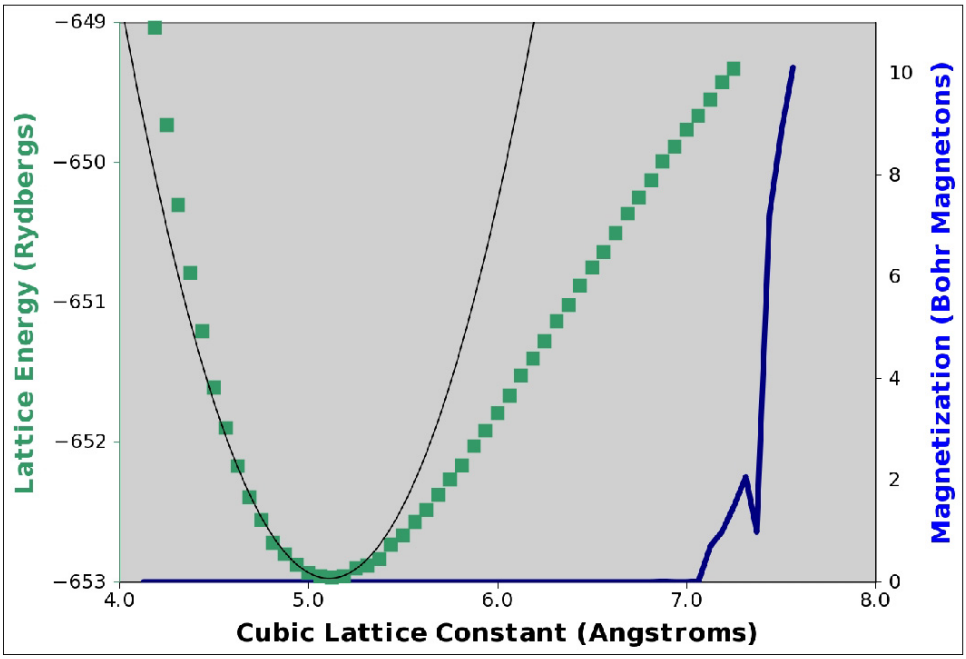

Figure 13. Ground state lattice energy (left vertical axis) in Rydbergs and absolute magnetization (right vertical axis) for cubic zirconia (ZrO_2) versus FCC lattice constant in Angstroms. The green squares show the ground state energy for the ferromagnetic solution, and the blue line shows absolute magnetization in Bohr Magnetons per unit cell. The narrow black line is the regression parabola that was derived by fitting the five points at the bottom of the energy curve to a second order polynomial. The extracted value of lattice constant is 5.1082 Å versus an accepted value of 5.07 Å.

density for the structure. The scales used in Figs. 11 and 12 are identical to those in Figs. 7 and 8, respectively. Aside from the "missing" valence electrons removed from the Mg atoms, the image shown in Fig. 11 closely resembles that of Fig. 7. In fact, the most obvious difference between the two figures is that the atoms appear slightly larger in Fig. 11. This is entirely due to the fact that the lattice constant in the MgO:Pd structure is considerably smaller (2×4.211 versus 2×4.815Å) than the lattice constant in the CaO:Pd structure, as is evident from the X and Y axis scales.

Finally, we note that the image in Fig. 12 is entirely black because there is no spin polarization down to the level of 10^{-5} electrons per cubic Bohr radius in the MgO:Pd structure, thus confirming our expectations that no spontaneous magnetization will appear because the Pd has not been strained up to its threshold for spontaneous ferromagnetic ordering. One dimensional cross sections were also performed for the same supercell runs (CaO:Pd with and without the single added H atom and MgO:Pd) whose two dimensional spin polarization false color images are shown in Figs. 8, 10, and 12. In order to avoid undue increases in the length of the paper, their plots are presented in a Supplemental Section contained on-line.

7. Application to the Arata Structure

Yoshiaki Arata of Osaka University has published a number of interesting papers in which he and his colleagues report several experimental observations that may be relevant to the computational results presented in this work. ZrO_2:Pd structures were fabricated by alloying Pd and Zr and subsequently oxidizing the alloy. Since Zr has a much higher chemical affinity for oxygen than Pd does, we end up with Pd nanoparticles embedded in an insulating matrix of ZrO_2

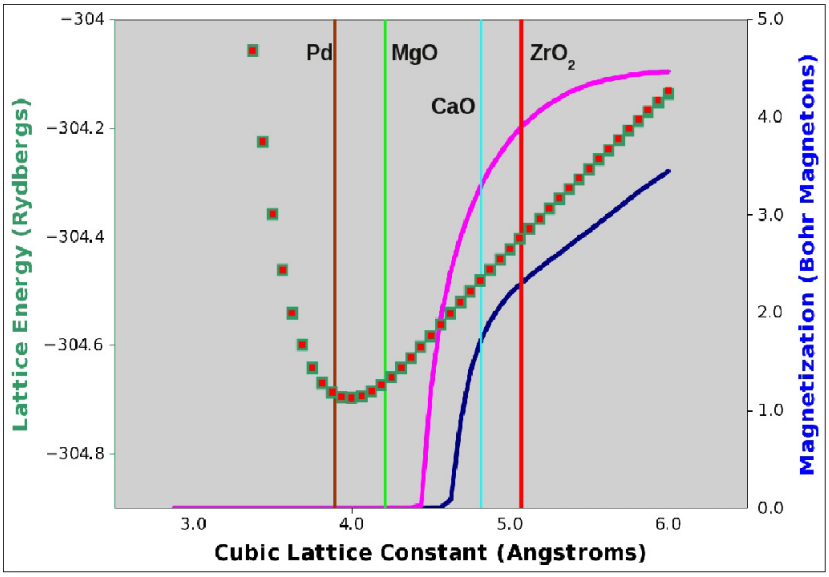

Figure 14. Simultaneous plots showing the ferromagnetic (green squares) and paramagnetic (small red squares) energy curve for Pd on the left vertical axis, the magnetization of Pd on the right vertical axis when strained in two and three dimensions, and the equilibrium lattice constants for Pd (brown), MgO (light green), CaO (light blue), and ZrO_2 (red) – all versus lattice constant.

(which can crystallize as the well-known cubic zirconia). The main experimental observations can be summarized as follows:

(1) Stimulation of the ZrO_2:Pd powder with ultrasonic power greatly increased the LENR rate.
(2) Stimulation of the ZrO_2:Pd powder with energy from a welding laser [10] greatly increased the LENR rate. In his ICCF-10 paper, Arata et al. do not state what kind of welding laser they employed. However, a literature search of Arata's other papers [11] strongly suggests that the laser was likely to have been a CO_2 laser. In fact, Arata invented the CO_2 laser welding process.
(3) LENR events, including the generation of significant quantities of ^{4}He, were observed when the ZrO_2:Pd powder was loaded with deuterium. No ^{4}He was observed when the pure light isotope of hydrogen was used.
(4) No ^{4}He was observed when the experiment was run with bulk Pd.
(5) The use of Pd black powder resulted in a low level of ^{4}He. The use of Pd nanoparticles resulted in higher ^{4}He levels, but not nearly as much as when the ZrO_2:Pd powder was used.

In light of the computational results presented in the previous sections of this work, we performed DFT studies of the cubic zirconia lattice with results presented in Fig. 13.

The error between the extracted value of lattice constant and the accepted value is about 0.75%, thus the most basic of the DFT results are in reasonable agreement with observation. The reader will note our DFT results predict that ZrO_2 can become ferromagnetic if it is placed in sufficiently high tensile stress. However, we do not expect this to happen in the Arata structure, because the ZrO_2 is placed in contact with Pd, which has a smaller lattice constant, thereby placing the zirconia in compressive stress. Having verified the lattice constant for FCC cubic zirconia, we next inquire how this value compares with the threshold for the onset of spontaneous ferromagnetic ordering in Pd. Results are shown in Fig. 14.

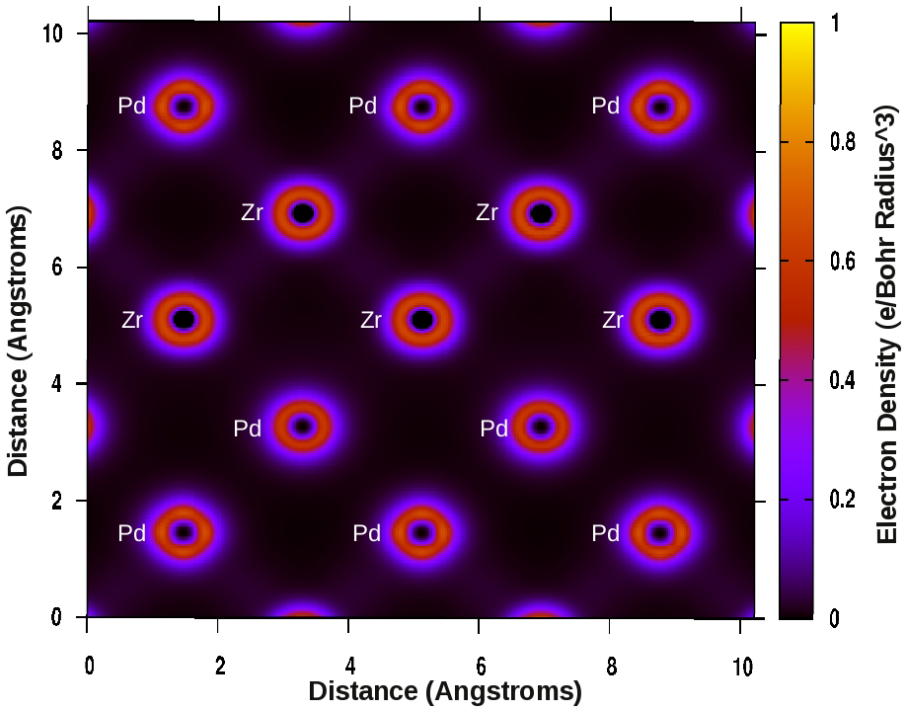

Figure 15. False color cross-sectional image of total charge taken parallel to the *YZ* plane (along the [100] crystal plane) and intersecting the ZrO_2:Pd supercell. Individual atoms are labeled for clarity. However, the oxygen atoms are not visible in this view because they occupy lattice sites located above and below the plane being represented in the figure. The Pd atoms can be distinguished from the Zr because the Pd core hole is smaller due to the higher nuclear charge. In addition, the Pd 4d valence charge cloud exhibits a slightly higher contrast around the circumference than the Zr atoms.

As we can see from the figure, cubic zirconia has a lattice constant larger than any of the substrates used by the MHI team. This suggests that growing Pd on a zirconia substrate will push the fraction of Pd cells that grow epitaxially further into the ferromagnetic regime than using MgO or even CaO. Indeed, the figure suggests that if the LENR rate is somehow driven by the local magnetic field intensity, we may expect to see rates for the Arata structures that are higher than those reported by the MHI team with their CaO substrates, provided only that the larger lattice constant of ZrO_2 does not cause the fraction of Pd cells growing epitaxially to plummet.

Before leaving the subject of the Arata results, we should comment on the use of the CO_2 laser and draw a connection with the work of Letts and Hagelstein. It is by now well-known that the output wavelength of a CO_2 laser is about 10.7 μm. When this free space wavelength is converted to frequency, we get a value of about 28.04 THz, which does not agree very well with the A1g stretching mode frequencies of 88.9, 108.8, and 125.7 THz for the D_2, HD, and H_2 free-space molecules, respectively. However, once the molecules are added to a monovacancy within the Pd lattice and the structure is relaxed to allow the hydrogen/deuterium atoms to find locally minimum energy positions, we calculate a number of phonon energy eigenvalues that lie in the 20–35 THz frequency range, depending upon which of several minimum energy sites are occupied by the hydrogen/deuterium molecules. Thus it is not difficult to believe that Arata and his colleagues may have been pumping the hydrided or deuterided Pd lattice close to one of its resonances, as indeed Letts and Hagelstein reported when they described three one-phonon resonances at 8, 15, and 20 THz in their

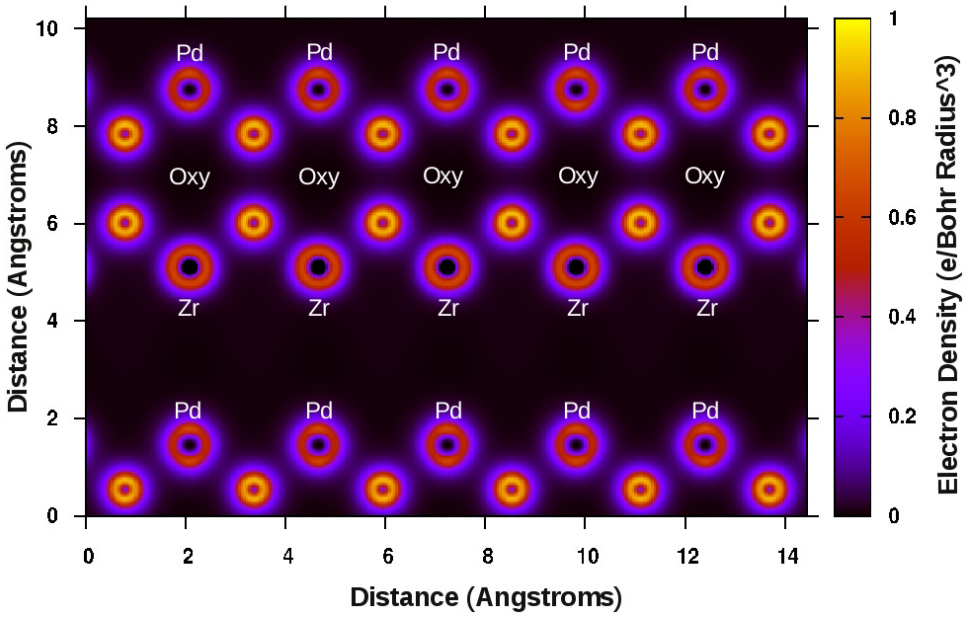

Figure 16. False color cross-sectional image of total charge density in a plane defined by the [110] and Z axes and intersecting the ZrO_2:Pd supercell. The aspect ratio of this figure is higher than 1:1 because the length of the [110] face diagonal is $\sqrt{2}$ times larger than the length of the unit cell in the X, Y, or Z dimensions.

two-laser paper [2]. What is also interesting is that Arata reports very little LENR activity when bulk Pd or powdered Pd was stimulated with the beam from the laser. Only when the Pd was in surface contact with a complex oxide did he observe high LENR activity and significant ^{4}He production.

8. DFT Study of the ZrO_2:Pd Interface

DFT studies of the ZrO_2:Pd interface were performed using a $2 \times 2 \times 2$ supercell in a manner similar to that described in Section 6 for the purpose of studying ferromagnetic activity and identifying which atomic species are most active. Figure 15 shows a false color image of the total charge density of the ZrO_2:Pd supercell sampled on a plane parallel to the YZ ([100]) plane and similar to those shown in Figs. 7, 9, and 11. The supercell lattice constant was set at 10.2164 Å, corresponding to a lattice constant of 5.1082 Å for each individual unit cell.

This view shows that the Pd and Zr atoms occupy the usual sites in the FCC supercell structure. However, the oxygen atoms are not visible in this view. In order to provide a view showing all 3 atomic species, we need to orient the horizontal axis in the crystallographic [110] direction instead of purely parallel to the Y-axis. Such a view is shown in Fig. 16.

As with the CaO:Pd and MgO:Pd structures, we generated spin-polarized images for the ZrO_2:Pd supercell. Figure 17 shows the spin-polarized image corresponding to the total charge image of Fig. 15, and Fig. 18 shows the spin-polarized image corresponding to the total charge image of Fig. 16. There are a number of striking features visible in Figs. 17 and 18. First, we note that the two rows of Pd atoms are no longer equally polarized; the Pd atoms located closest to the oxygen atoms are polarized about 20 times more strongly than the Pd atoms located closest to the Zr atoms. Likewise, the two rows of oxygen atoms shown in the figure are also no longer equivalent; the oxygen atoms

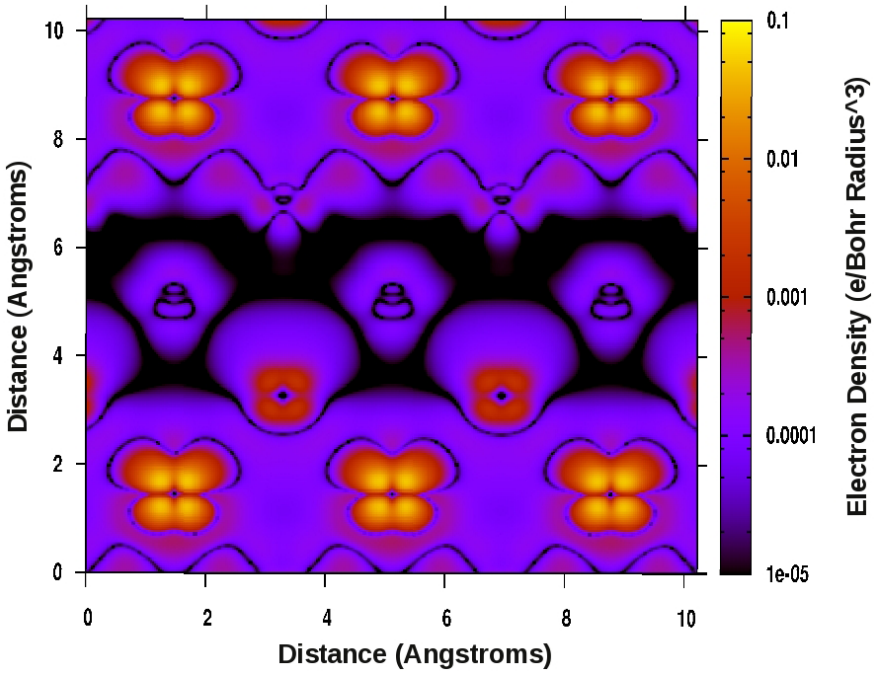

Figure 17. False color cross-sectional image of spin-up minus spin-down charge density taken parallel to the *YZ* plane (along the [100] crystal plane) and intersecting the ZrO_2:Pd supercell. The brightest features identify the lowest row of three Pd atoms, while the upper row of two Pd atoms (shown in red) is not as strongly magnetized. The magnetically inactive zirconium atoms are shown largely in violet and black with just a trace of red.

located closest to the Pd are much more strongly polarized than the ones near the Zr atoms. We also note that the Zr atoms themselves are very weakly polarized. This latter observation should not be especially surprising, because the lattice constant for the individual unit cells in this run was set to 5.1082 Å, corresponding to the minimum in the ZrO_2 energy curve. This is considerably less than the computed threshold of about 7 Å for the onset of spin polarization of the Zr atoms. Finally, both figures reveal exactly two zero crossings in traveling between any two Pd atoms and between any Pd and one of the neighboring strongly polarized oxygen atoms. Thus all of the Pd are ferromagnetically ordered, and furthermore, the oxygens are ferromagnetically polarized with respect to the Pd atoms, a situation very different from what is shown in Fig. 10, where the single hydrogen electron spin is polarized antiferromagnetically with respect to the Pd. One dimensional cross sections were also performed for the same ZrO_2:Pd supercell run whose two dimensional spin polarization false color images are shown in Figs. 17 and 18. In order to avoid undue increases in the length of the paper, their plots are presented in the on-line Supplemental Section.

The three structures discussed in this work may also be compared by providing their respective total supercell magnetic polarizations. For the MgO:Pd structure, the total magnetization is obviously zero, because there were no species whose interatomic separation was pushed beyond the threshold for spontaneous magnetization. For the CaO:Pd supercell, the total absolute magnetization was 5.57 Bohr magnetons, while for the ZrO_2:Pd supercell, the value was 8.61 Bohr magnetons. In both of the latter structures, the only atoms to become polarized are the Pd and the oxygens. The CaO:Pd supercell contains a total of 32 Pd and oxygen atoms, while the ZrO_2:Pd supercell contains a total of 48. Thus the ratio of polarized atoms between the two structures is $48/32 = 1.50$. As it turns out, the ratio of the

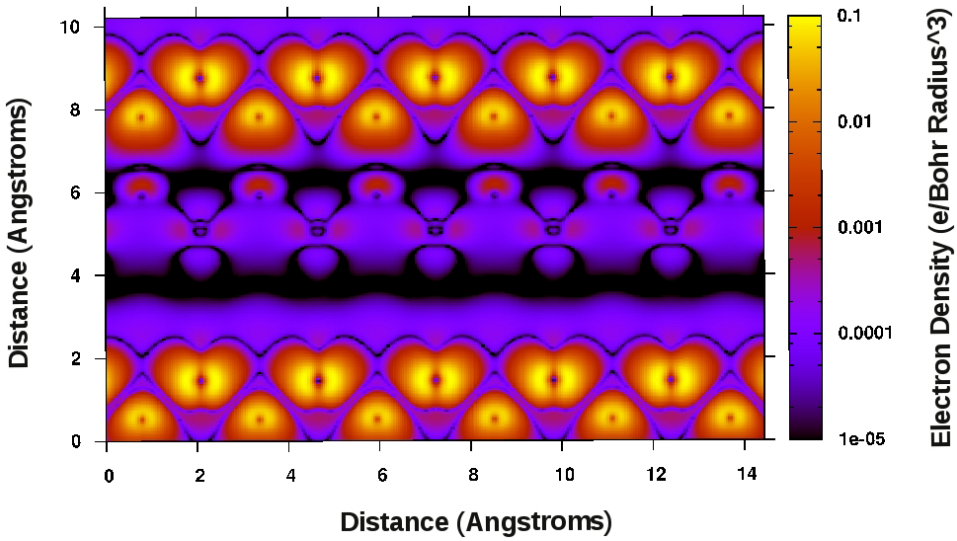

Figure 18. False color cross-sectional image of spin-up minus spin-down charge density in a plane defined by the [110] and Z axes and intersecting the ZrO_2:Pd supercell. The bright heart-shaped features identify the highly magnetized rows of Pd atoms, while the smaller bright features are the rows of oxygen atoms located near the highly magnetized Pd atoms. The less highly magnetized oxygen atoms are shown in red below their more highly magnetized counterparts. Once again, the magnetically inactive zirconium atoms are shown largely in violet and black. Finally, the less highly magnetized Pd atoms are not visible in this cross-sectional view.

two magnetizations was $8.61/5.57 = 1.54$. It is thus tempting to attribute the magnetization difference simply to the difference in the number of polarized atoms. However, the local variations in spin polarization shown in the figures suggest that this is an oversimplified picture, because all of the Pd and oxygen atoms in the CaO:Pd supercell are strongly polarized, while this is clearly not true for either the Pd or the oxygen atoms in the ZrO_2:Pd supercell. A more accurate picture can be obtained by making one dimensional plots of spin polarization through each of the two supercells and plotting the results on a linear scale instead of the logarithmic scale used in the false color images. Such a plot is shown in Fig. 19.

Care must be exercised in running one dimensional cross sections through the atoms, however, because the lattice symmetry induces nodes in the spin polarization along certain directions. In order to avoid sampling the spin polarizations along nodal lines, it was necessary to section the CaO:Pd supercell in the [001] direction (Z-direction) along a vector passing through the origin of coordinates. Thus the red line in the plot passes through Pd atoms at the 0.2 and 1.2 values of the Z-coordinate. The pair of minor peaks near 1.0 on the X-axis correspond to one of the oxygen atoms. For the ZrO_2:Pd supercell, it was necessary to perform our section in the [110] direction at an altitude of $Z = 0$ in order to pass through the antinodes in the spin polarization for the Pd atoms, and each pair of tall, green peaks represents one Pd atom. Even after exercising care to ensure our sections pass through the antinodes of the atomic polarization patterns, it is clear that the peak spin polarization is about two times larger for the ZrO_2:Pd structure than it is for the CaO:Pd. This is most probably attributable to the fact that the larger ZrO_2:Pd lattice constant pushes the Pd further up the magnetization curve than the CaO:Pd structure does.

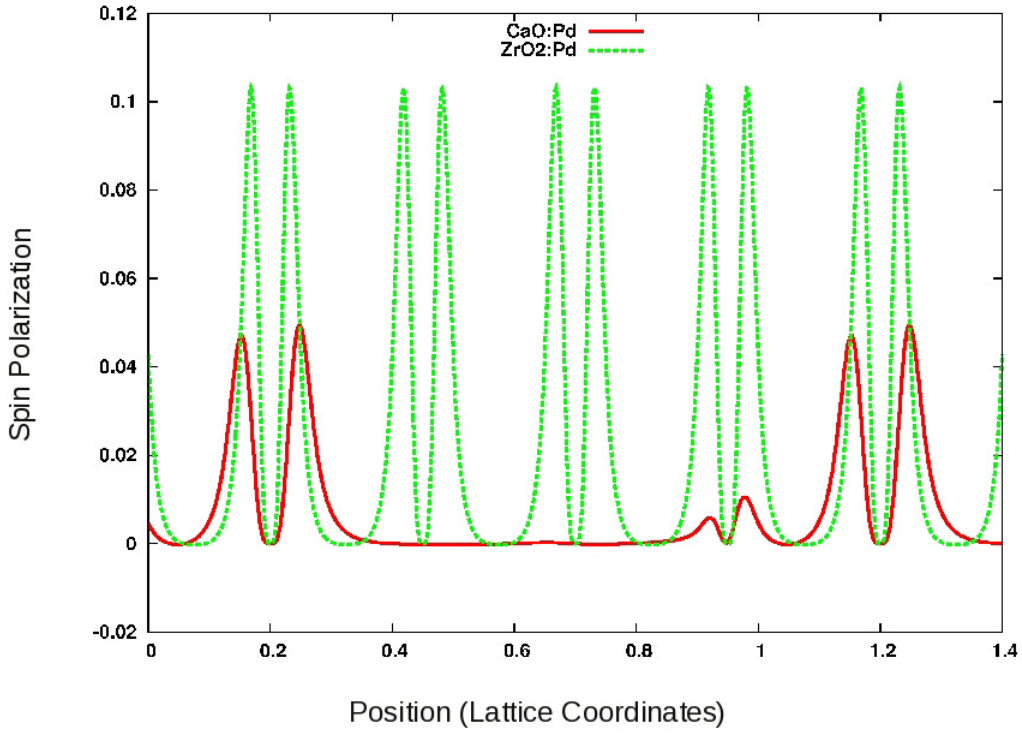

Figure 19. Plots of spin polarization (in units of electronic charges per cubic Bohr radius) versus position in the CaO:Pd supercell (red solid line) and in the ZrO_2:Pd supercell (green dotted line). The horizontal coordinates for the ZrO_2:Pd plot were divided by $\sqrt{2}$ to permit display on the same axis scale. The tall peaks in each of the plots represent the Pd atoms.

9. Summary

In summary, spin-polarized DFT computations have been useful in providing insight into the magnetic behavior of many of the transition metals on the Periodic Table in their elemental lattices. Most of the transition metals and a number of sp elements (including diamond, aluminum, silicon, germanium, selenium, tellurium, lead, and polonium) are predicted to exhibit ferromagnetic ordering when their lattices are placed in sufficiently high tensile stress. At the threshold lattice constant for the onset of this ferromagnetic ordering, we predict that the energy surface for the elemental lattice bifurcates into two stable solutions, one paramagnetic with a higher energy and one ferromagnetic with a lower energy. The paramagnetic sheet for the energy surface above threshold joins smoothly with the paramagnetic sheet below threshold, however the ferromagnetic sheet joins with the paramagnetic sheet in such a way that the energy is continuous, but its derivatives may exhibit jump discontinuities at the threshold. Most of the elements exhibit magnetization curves that rise very rapidly with lattice constant above threshold and then saturate at higher values, approaching well-defined asymptotes as the lattice constant grows. In most cases, the normalized values of these asymptotic magnetizations lie close to 1.0 Bohr Magneton per unpaired p or d electron spin, which is the expected limiting case for isolated atoms. Interestingly, we find that (with the possible exceptions of the Lanthanide and Actinide series) the atoms whose outermost electron shells contain only s electrons do not exhibit ferromagnetic ordering at any

practical value of lattice constant. This specifically includes all the Columns I and II elements and several elements on the right-hand edge of the Transition Metal Group such as zinc, cadmium, silver, and gold.

The results summarized above may now be applied to a variety of multilayer structures whose LENR results have been published during the past 15 years. The Mitsubishi Heavy Industries (MHI) team under Yasuhiro Iwamura reported successful observation of several different types of nuclear transmutations when using a structure consisting of alternating layers of CaO and Pd, both of which crystallize in the face-centered cubic (FCC) structure. The CaO unit cell lattice constant is about 4.815 Å, placing it above the threshold for the onset of spontaneous ferromagnetic ordering of Pd (4.50 Å when tensile stress is applied in all three dimensions, 4.69 Å when stress is applied in only two dimensions). By contrast, they reported negative experimental results when MgO was substituted for the CaO. The lattice constant for MgO is only 4.211 Å, placing it well below the thresholds for magnetization in Pd. Similarly, the Osaka University team under Yoshiaki Arata reported high LENR rates and ^{4}He production rates when their Pd nanoparticles were grown in intimate contact with ZrO_2, which also has an FCC lattice and a lattice constant of about 5.07 Å. They reported much lower LENR rates when bulk Pd or even finely divided Pd powder was used in the same experimental apparatus.

The search to identify the experimental parameters that most directly control LENR phenomena has posed and continues to pose difficult challenges for the community. The effect of magnetic fields upon measured LENR rates has been known for some time but is not yet well understood. Our results suggest the possible existence of an underlying order involving spontaneous magnetization that may tie together the work of several different teams and materials systems. It is hoped that these results will provide a number of mechanistic clues for the theoretical community as well as guidance for LENR materials specialists seeking to optimize reactor structures for various LENR applications of the future.

Acknowledgements

The DFT studies documented in this work are a direct outgrowth of US Navy research that was funded under the In-house Laboratory Independent Research (ILIR) Program, and we wish to gratefully acknowledge the strong support of Jeff Solka (the ILIR sponsor) and the Department Q management over the past 5 years. In addition, we wish to thank a number of dear colleagues for their inspiration, including Peter Hagelstein of the MIT Electronics Research Laboratory, the LENR teams at the NASA Langley and Glenn facilities, and especially Olga Dmitriyeva and Rick Cantwell of Coolescence, who were instrumental in suggesting the potential value of spin-polarized calculations in elemental metal systems.

References

[1] J.O.M. Bockris, R. Sundaresan, Z, Minevski and D. Letts, Triggering of heat and sub-surface changes in Pd–D systems, *ICCF Conference Proceedings*, Vol. 4, 1993.

[2] D. Letts and P.L. Hagelstein, Stimulation of optical phonons in deuterated palladium, *ICCF Conference Proceedings*, Vol. 14, 2008.

[3] Y. Iwamura, T. Itoh, M. Sakano, N. Yamazaki, S. Kuribayashi, Y. Terada, T. Ishikawa and J. Kasagi, Observation of nuclear transmutation reactions induced by D_2 gas permeation through Pd complexes, *ICCF Conference Proceedings*, Vol. 11, 2004.

[4] Y. Arata and Y.C. Zhang, Development of compact nuclear fusion reactor using solid pycnodeuterium as nuclear fuel, *ICCF Conference Proceedings,* Vol. 10, 2002.

[5] P. Hohenberg and W. Kohn, Inhomogeneous electron gas, *Phys. Rev.* **136** (1964) B864–B871.

[6] W. Kohn and L.J. Sham, Self-consistent equations including exchange and correlation effects, *Phys. Rev*. 140 (1965) A1133–A1138.

[7] P. Giannozzi, S. Baroni, N. Bonini, M. Calandra, R. Car, C. Cavazzoni, D. Ceresoli, G.L. Chiarotti, M. Cococcioni, I. Dabo,, A. Dal Corso, S. de Gironcoli, S. Fabris, G. Fratesi, R. Gebauer, U. Gerstmann, C. Gougoussis, A. Kokalj, M. Lazzeri, L. Martin-

Samos, N. Marzari, F. Mauri, R. Mazzarello, S. Paolini, A. Pasquarello, L. Paulatto, C. Sbraccia, S. Scandolo, G. Sclauzero, A.P. Seitsonen, A. Smogunov, P. Umari and R.M. Wentzcovitch, *J. Phys.: Condensed Matter* **21** (2009) 395502.

[8] R.W.G. Wyckoff, *Crystal Structures*, Wiley, New York, 1963.

[9] T. Hioki, N. Takahashi, S. Kosaka, T. Nishi, H. Azuma, S. Hibi, Y. Higuchi, A. Murase and T. Motohiro, Inductively coupled plasma mass spectrometry study on the increase in the amount of Pr atoms for Cs–Ion–implanted Pd/CaO multilayer complex with deuterium permeation, *Jap. J. Appl. Phys.* **52** (2013) 107301-1–107301-8.

[10] Y. Arata and Y.C. Zhang, Development of compact nuclear fusion reactor using solid pycnodeuterium as nuclear fuel, *ICCF Conference Proceedings*, Vol. 10, 2003.

[11] See, for example, Y. Arata, N. Abe and T. Oda, Fundamental phenomena in high power CO_2 laser welding (Report I): atmospheric laser welding (welding physics, process & instrument), *Trans. JWRI* **14**(1) (1985) 5–11.

Appendix A

Appendix B

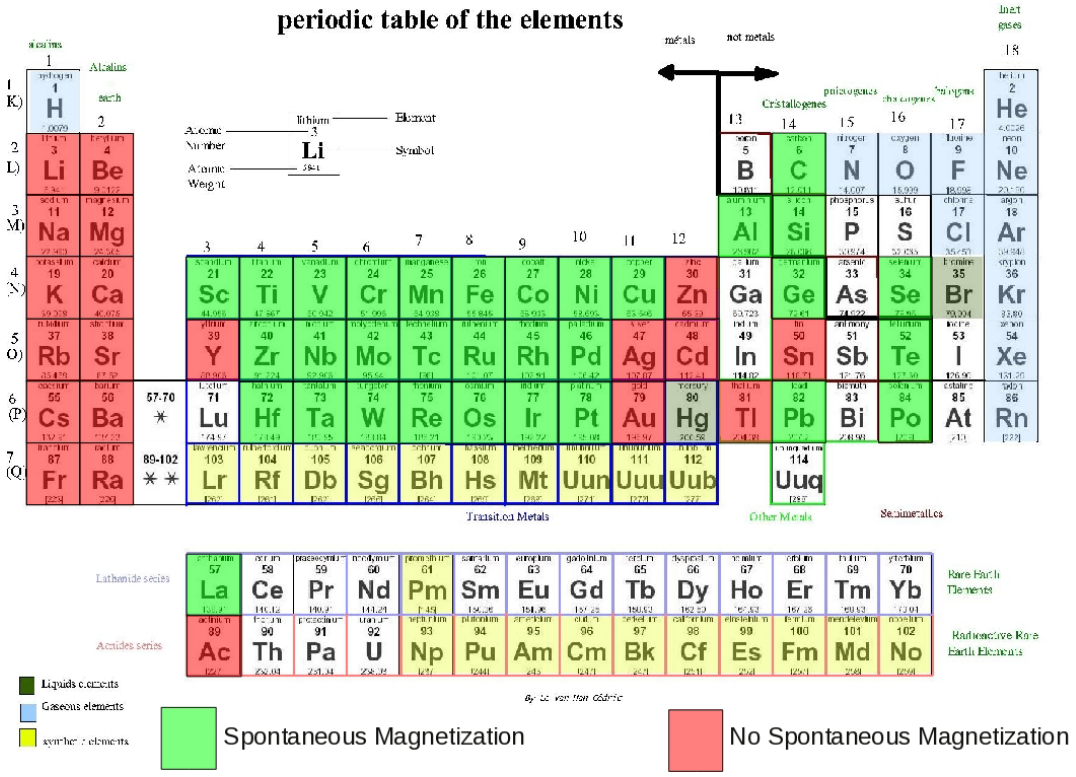

Figure 20. Appendix B: Periodic Table of the elements.

Supplementary Figures

Table 1. Appendix A: Table of computed and accepted values of lattice constant

Element	Lattice type	Pseudopotential file name	Computed a	Accepted a	% Error
Actinium	Face-Centered Cubic	Ac.pbe-mt-fhi.UPF	5.3199	5.31	0.186
Aluminum	Face-Centered Cubic	Al.pbe-rrkj.UPF	4.0219	4.0495	–0.682
Antimony	Hexagonal Close Packed	Sb.pbe-rrkj.UPF	3.4163	3.33	2.592
Barium	Body-Centered Cubic	Ba.pbe-nsp-van.UPF	4.982	5.02	–0.757
Beryllium	Hexagonal Close Packed	Be-pbe-rrkjus.UPF	2.3035	2.2858	0.774
Cadmium	Hexagonal Close Packed	Cd.pbe-n-van.UPF	3.117	2.9794	4.618
Calcium	Face-Centered Cubic	Ca-pbe-nsp-van.UPF	5.5458	5.5884	–0.762
Carbon (Diamond)	Face-Centered Cubic	C.pbe-rrkjus.UPF	3.5685	3.57	–0.042
Cesium	Body-Centered Cubic	Cs-pbe-mt-fhi.UPF	5.8912	6.141	–4.068
Chromium	Body-Centered Cubic	Cr.pbe-sp-van.UPF	2.8552	2.91	–1.883
Cobalt	Hexagonal Close Packed	Co-pbe-nd-rrkjus.UPF	2.5184	2.5071	0.451
Copper	Face-Centered Cubic	Cu.pbe-d-rrkjus.UPF	3.6315	3.61	0.596
Germanium	Face-Centered Cubic	Ge.pbe-mt_fhi.UPF	5.8722	5.6575	3.795
Gold	Face-Centered Cubic	Au.pz-nd-rrkjus.UPF	4.0204	4.08	–1.461
Hafnium	Hexagonal Close Packed	Hf-pbe-mt-fhi.UPF	3.2194	3.1964	0.720
Iridium	Face-Centered Cubic	Ir-pbe-n-rrkjus.UPF	3.839	3.9092	–1.796
Iron	Body-Centered Cubic	Fe-pbe-nd-rrkjus.UPF	2.8783	2.87	0.289
Lanthanum	Hexagonal Close Packed	La-pbe-nsp-van.UPF	3.662	3.75	–2.347
Lead	Face-Centered Cubic	Pb-pbe-d-van.UPF	5.007	4.9508	1.135
Lithium	Body-Centered Cubic	Li-pbe-n-van.UPF	3.5092	3.51	–0.023
Magnesium	Hexagonal Close Packed	Mg-pz-n-vbc.UPF	3.1598	3.21	–1.564
Manganese	Body-Centered Cubic	Mn.pbe-sp-van.UPF	2.8649	2.85	0.523
Molybdenum	Body-Centered Cubic	Mo-pbe-mt-fhi.UPF	3.2148	3.147	2.154
Nickel	Face-Centered Cubic	Ni.pbe-nd-rrkjus.UPF	3.52	3.524	–0.114
Niobium	Body-Centered Cubic	Nb-pbe-nsp-van.UPF	3.3051	3.3	0.155
Osmium	Hexagonal Close Packed	Os.pbe-mt-fhi.UPF	2.8072	2.7344	2.662
Palladium	Face-Centered Cubic	Pd-pbe-rrkjus-4d10.UPF	3.974	3.8907	2.141
Platinum	Face-Centered Cubic	Pt-pbe-nd-rrkjus.UPF	3.9854	3.92	1.668
Polonium	Simple Cubic	Po-pbe-mt-fhi.UPF	3.2074	3.359	–4.513
Potassium	Body-Centered Cubic	K-pz-n-vbc.UPF	5.2401	5.23	–0.194
Rhenium	Hexagonal Close Packed	Re.pbe-mt-fhi.UPF	2.8139	2.761	1.916
Rhodium	Face-Centered Cubic	Rh-pbe-rrkjus.UPF	3.959	3.8	4.184
Rubidium	Body-Centered Cubic	Rb-pbe-mt-fhi.UPF	5.468	5.585	–2.095
Ruthenium	Hexagonal Close Packed	Ru.pbe-n-van.UPF	2.779	2.7059	2.702
Scandium	Hexagonal Close Packed	Sc.pbe-nsp-van.UPF	3.303	3.309	–0.181
Selenium	Hexagonal	Se.pbe-van.UPF	4.4695	4.36	2.511
Silicon	Face-Centered Cubic	Si.pbe-rrkj.UPF	5.5085	5.4309	1.429
Silver	Face-Centered Cubic	Ag-pbe-d-rrkjus.UPF	4.1333	4.09	1.058
Sodium	Body-Centered Cubic	Na-pbe-sp-van-ak.UPF	4.1283	4.2906	–3.783
Strontium	Face-Centered Cubic	Sr-pbe-sp-van.UPF	6.0934	6.08	0.220
Tantalum	Body-Centered Cubic	Ta-pbe-nsp-van.UPF	3.3418	3.3013	1.227
Technetium	Hexagonal Close Packed	Tc.pbe-mt-fhi.UPF	2.776	2.735	1.499
Tellurium	Hexagonal	Te.pbe-rrkj.UPF	4.5050	4.45	1.236
Thallium	Hexagonal Close Packed	Tl-pbe-mt-fhi.UPF	3.3538	3.4566	–2.974
Tin	Tetragonal	Sn-pbe-d-rrkjus.UPF	5.9175	5.8318	1.470
Titanium	Hexagonal Close Packed	Ti-pbe-sp-van.UPF	2.923	2.9508	–0.942
Tungsten	Body-Centered Cubic	W-pbe-nsp-van.UPF	3.1951	3.1652	0.945
Vanadium	Body-Centered Cubic	V-pbe-n-van.UPF	3.0078	3.02	–0.404
Yttrium	Hexagonal Close Packed	Y-pbe-nsp-van.UPF	3.6318	3.65	–0.499
Zinc	Hexagonal Close Packed	Zn-pbe-van.UPF	2.7353	2.6649	2.642
Zirconium	Hexagonal Close Packed	Zr-pbe-nsp-van.UPF	3.2254	3.232	–0.204

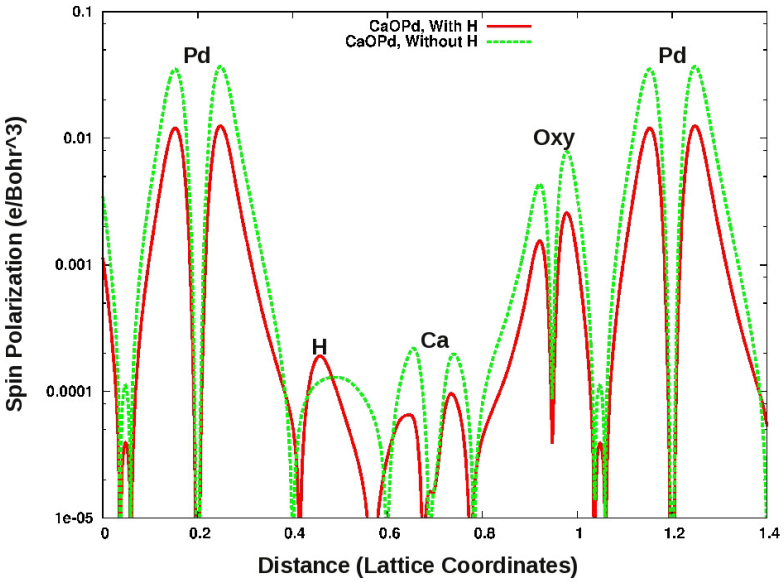

Figure 21. Supplementary Figure S1.

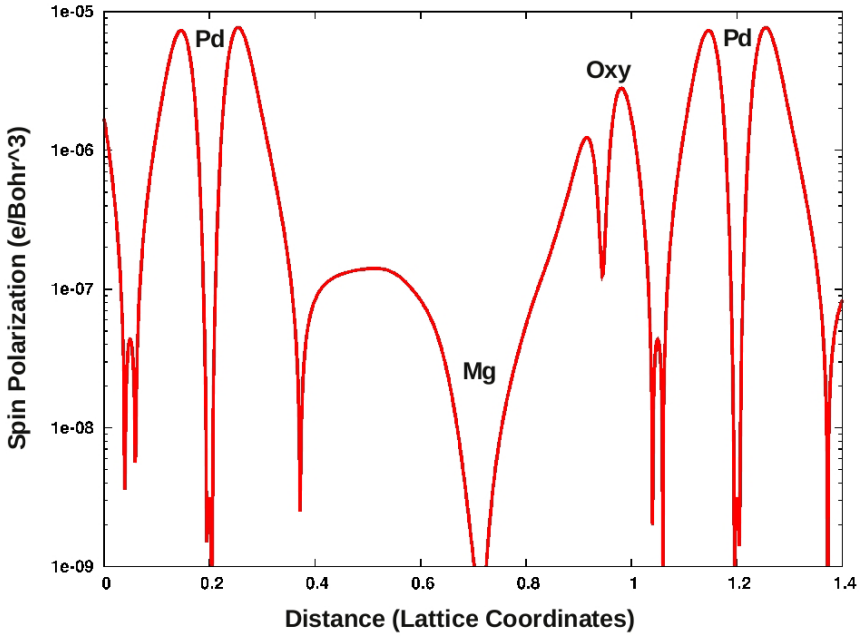

Figure 22. Supplementary Figure S2.

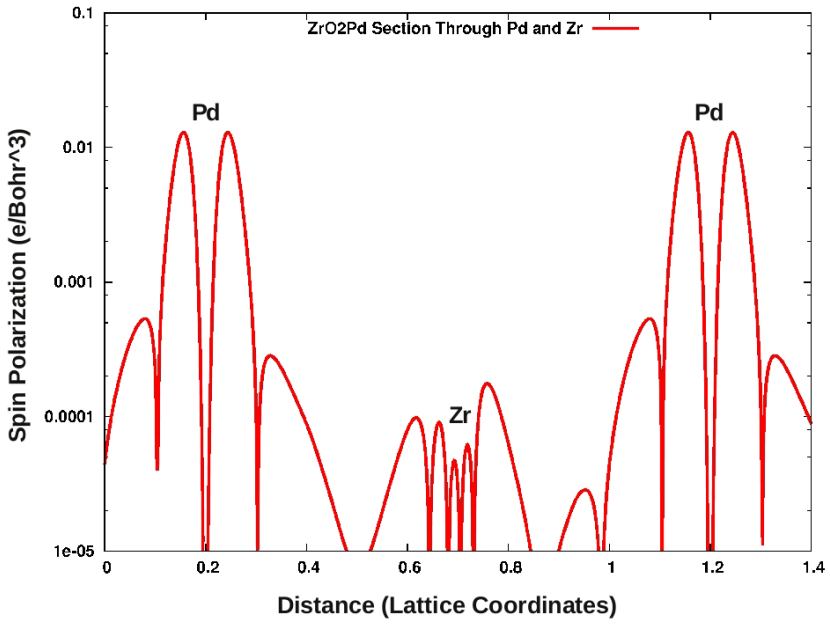

Figure 23. Supplementary Figure S3.

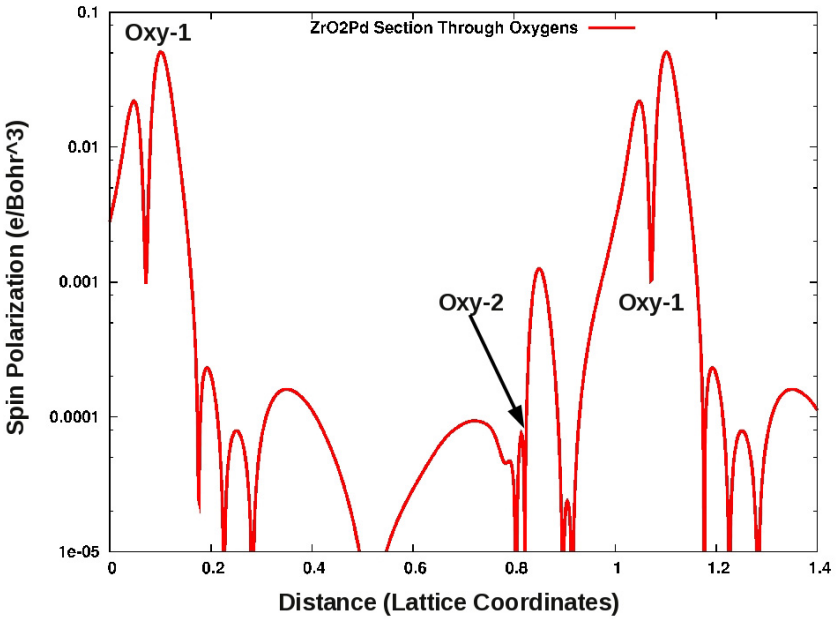

Figure 24. Supplementary Figure S4.

J. Condensed Matter Nucl. Sci. 17 (2015) 27–34

Research Article

Nuclear Exothermic Reactions in Lattices: A Theoretical Study of D–D Reaction

Fulvio Frisone*

Department of Physics, University of Catania, Italy

Abstract

In this work we try to explain the deuteron–deuteron reactions within palladium lattice by means of the coherence theory of nuclear and condensed matter. The coherence model of condensed matter affirms that within a deuteron-loaded palladium lattice there are three different plasmas: electrons, ions and deuterons plasma. Then, according to the loading percentage x = D/Pd, the ions deuterium can take place on the octahedrical sites or in the tetrahedral in the (1,0,0)-plane. In the coherence theory it is called β-plasma the deuterons plasma in the octahedral site and γ-plasma which in tetrahedral. We propose a general model of effective local time-dependent deuteron–deuteron potential, that takes into account the electrons and ions plasma oscillations. The main features of this potential are extracted by means of many-body theory considering the interaction deuteron–phonon–deuteron. In fact the phonon exchange produces a attractive component between two deuteron within the D_2 molecular. This attractive force is able to reduce the inter-nuclear distance from about 0.7 to 0.16 Å. It means that the lattice strongly modifies the nuclear environment with respect to free space. In this way according to deuterons energy, loading percentage and plasma frequency we are able to predict high o low tunneling probability.
 ISSN 2227-3123

Keywords: Coherence theory, Condensed matter, Dislocations within the ions of the metal, Low energy nuclear reactions

1. Introduction

In a model of lattice a reaction takes place within the Coherence Theory of Condensed Matter and represents a general theoretical framework accepted by most of physicists that work on the cold fusion phenomenon. In the coherence theory of condensed matter [1] it is assumed that the electromagnetic (e.m.) field due to elementary constituents of matter (i.e. ions and electrons) plays a very important role in the dynamic system. In fact, considering the coupling between e.m. equations, due to charged matter, and the Schrödinger equation of field operator, it is possible to demonstrate that in proximity of e.m. frequency ω_0, the matter system is represented by a coherence dynamic system. For this reason it is possible to speak about coherence domains whose length is about $\lambda_{CD} = 2\pi/\omega_0$.

*E-mail: frisone@ct.infn.it

 ISSN 2227-3123

Of course the simplest model of matter with coherence domain is the plasma system. In the usual plasma theory we must consider the plasma frequency ω_{p} and the Debey length that measures the coulomb force extension, i.e. the coherence domain length. For a system with N charges Q of m mass within a V volume the plasma frequency can be written as

$$\omega_{\mathrm{p}} = \frac{Q}{\sqrt{m}}\sqrt{\frac{N}{V}}. \tag{1}$$

This presentation is focused on the "nuclear environment" that is supposed to exist within the palladium lattice D_2-loaded and at room temperature as predicted by the Coherence Theory. In fact, when the palladium lattice is loaded with deuterium gas, according to some people, it is possible to observe traces of nuclear reactions [2–4]. For this reason many physicists speak about Low Energy Reaction Nuclear (LERN). Various experiments prove that in the D_2-loaded palladium lattice the most frequent nuclear reactions are [4,5]:

(1) D+D$\rightarrow$ ^{3}H + p + 4.03 MeV,

(2) D+D$\rightarrow$ ^{4}He + 23.85 MeV.

The aim of this presentation is to propose a "coherence" model through which it becomes possible to explain the occurrence of reactions (1) and (2) and their probability, according to the most reliable experiments. The starting point of this theoretical study is the analysis of the inner environment of the lattice, i.e. of plasma present within the lattice itself (d-electron, s-electron, Pd-ions and D-ions), using the coherence theory of matter; the following step is based on the effective potential reported in [6,7] by adding the role of lattice perturbations through which the computation of the (D–D) tunneling probability improves.

2. Plasma Present within the Non-loaded Palladium Lattice

According to the Coherence Theory of Condensed Matter, in a Pd lattice at room temperature the electron shells are in a coherent regime within a coherent domain. In fact they oscillate in tune with a coherent e.m. field trapped in the coherent domains. For this reason, in order to describe the lattice environment, we must consider the s-electron and d-electron plasma.

2.1. Plasma of d-electrons

They are formed by palladium d-shell electrons. We can start computing:

$$\omega_{\mathrm{d}} = \frac{e}{\sqrt{m}}\sqrt{\frac{n_{\mathrm{d}}N}{V}} \tag{2}$$

as d-electron plasma frequency. But according to the coherence theory of matter the plasma frequency is about 1.38 and this factor is obtained assuming a uniform d-electron charge distribution. But of course the d-electron plasma is localized in a shell of radius R (that is about 1 Å), so the geometrical contribution is

$$\sqrt{\frac{6}{\pi}} = 1.38. \tag{3}$$

From the *renormalized* d-electron plasma frequency, you obtain:

$$\omega_{\mathrm{de}} = 41.5\ \mathrm{eV}/\hbar \tag{4}$$

and the maximum oscillation amplitude ξ_{d} is about 0.5 Å.

2.2. Plasma of delocalized s-electrons

The s-electrons are the ones that within the lattice structure neutralize the adsorbed deuteron ions. They are delocalized and their plasma frequency depends on loading ratio (D/Pd percentage) shown in the following equation (5):

$$\omega_{\text{se}} = \frac{e}{\sqrt{m}}\sqrt{\frac{N}{V}} \cdot \sqrt{\frac{x}{\lambda_{\text{a}}}}, \tag{5}$$

where

$$\lambda_{\text{a}} = \left[1 - \frac{N}{V}V_{\text{pd}}\right] \tag{6}$$

and V_{pd} is the volume actually occupied by the Pd-atom. As reported in [1]:

$$\omega_{\text{se}} \approx x^{1/2} 15.2 \text{ eV}/\hbar. \tag{7}$$

For example for $x = 0.5$, the ω_{se} is about 10.7 eV/$\hbar$.

2.3. Plasma of Pd-ions

Further, it is important to consider the plasma due to Palladium ions that form the lattice structure. In this case it is possible to demonstrate that the frequency is

$$\omega_{\text{pd}} = 0.1 \text{ eV}. \tag{8}$$

3. Plasma Present within the D_2-Loaded Palladium Lattice

We know that deuterium is adsorbed as soon as it touches the palladium surface. This loading can be enhanced using electrolytic cells or vacuum chambers working at opportune pressure [8,9]. Throughout Preparata's theory of Condensed Matter it is assumed that, according to the ratio x = D/Pd, three phases, concerning the D_2–Pd system, reaction:

(1) phase α for $x < 0.1$,

(2) phase β for $0.1 < x < 0.7$,

(3) phase γ for $x > 0.7$.

In the α phase, the D_2 is in a disordered and not coherent state (D_2 is not charged!). Regarding the other phases, the following ionization reaction takes place on the lattice surface, due to lattice e.m. field:

$$\text{D}_{\text{lattice}} \rightarrow \text{D}^+ + \text{e}^-. \tag{9}$$

Then, according to the loading percentage x = D/Pd, the ions deuterium can release on the octahedrical or in the tetrahedral sites are in the (1,0,0)-plane. In the coherence theory it is called β-plasma the deuterons plasma in the octahedral site and γ-plasma in the tetrahedral site.

Regarding the β-plasma it is possible to affirm that plasma frequency is

$$\omega_\beta = \omega_{\beta 0}(x + 0.05)^{1/2}, \tag{10}$$

where

$$\omega_{\beta 0} = \frac{e}{\sqrt{m_{\mathrm{D}}}} \left(\frac{N}{V}\right)^{1/2} \frac{1}{\lambda_{\mathrm{a}}^{1/2}} = \frac{0.15}{\lambda_{\mathrm{a}}^{1/2}} \text{ eV}/\hbar. \tag{11}$$

For example if we use $\lambda_{\mathrm{a}} = 0.4$ and $x = 0.5$ you obtain $\omega_\beta = 0.168$ eV/$\hbar$.

In the tetrahedral sites the D^+ can occupy the thin disk that encompass two sites.

They present to the D^+ ions a barrier. Note that the d-shell electrons oscillate past the equilibrium distance y_0 (about 1.4 Å) thus embedding the ions in a static cloud of negative charge (which can screen the coulomb barrier). So, as reported in have [7]:

$$\omega_\gamma = \sqrt{\frac{4Z_{\mathrm{eff}}\alpha}{m_{\mathrm{D}} y_0^2}} \approx 0.65 \text{ eV}/\hbar. \tag{12}$$

Of course this frequency depends also on chemical condition of the palladium lattice (impurities, temperature, etc.)

Due to a large plasma oscillation of d-electrons, in the disk-like tetrahedral region (where the γ-phase D^+'s are located) a high density negative charge condenses giving rise to a screening potential $W(t)$.

We emphasize that the γ-phase depends on x value and that this new phase has been experimentally observed [10].

The new phase γ is very important in the LERN investigation. In fact many "cold fusion physicists" declare the main point of *cold fusion protocol* is that the loading D/Pd ratio must be higher than 0.7, i.e. the deuterium must be placed in the tetrahedral sites.

4. The D–D Potential

In [6], it was shown that the phenomenon of fusion between nuclei of deuterium in the crystalline lattice of a metal is conditioned by the structural characteristics, by the dynamic conditions of the system, and also by the concentration of impurities present in the metal under examination.

In fact, studying the interaction between deuterons (including the deuteron–plasmon contribution) in the case of three typical metals (Pd, Pt and Ti), a three-dimensional model showed that the height of the Coulomb barrier decreases upon the variance of the total energy and the concentration of impurities within the metal itself.

The starting potential that links Morse-like attraction and Coulomb-like repulsion can be written in this way [6,7]:

$$V(r) = k_0 \frac{q^2}{r} \cdot \left(V(r)_{\mathrm{M}} \frac{A}{r}\right) \tag{13}$$

In (13), $V(r)_{\mathrm{M}}$ is a Morse-like potential, and is given by:

$$V(r)_{\mathrm{M}} = B\left\{\exp\left(-2\varphi\left(r - r_0\right)\right) - 2\exp\left(-\varphi\left(r - r_0\right)\right)\right\} \tag{14}$$

Here the parameters A, B, φ and r_0 depend on the lattice.

In fact the D–D potential (13) is an effective potential whose reliability is shown by its own ability to fit the Coulomb potential for $r \to 0$ and the Morse potential in the attractive zone. Moreover, Siclen and Jones [11] defined ρ the point where the Coulomb potential is linked by the Morse trend, r_0' the equilibrium distance and D' the well. Certainly, within the free space for a D_2 molecule, ρ is about 0.3 Å , r_0' is about 0.7 Å and D' is –4.6 eV. But within the lattice the screening effect and the deuteron–deuteron interaction due to phonon exchange modify noticeably these parameter values.

Considering the role of coupling between deuterons and plasmons, in [12] the authors have numerically evaluated a D–D potential having the features of potential (13) with $D' = -50$ eV and $r'_0 = 0.5$ Å and $\rho = 0.2$ Å (in [12] the authors consider only two plasmon excitations at 7.5 and 26.5 eV).

4.1. The features of potential (14)

Since the screening effect can be modulated by donor atoms the role of impurities becomes considerable (as shown in [6,7]) and has been proven that

$$A = JKTR \tag{15}$$

and

$$B = J/\zeta. \tag{16}$$

Here J is the impurities concentration, *KT* is the lattice temperature, R the nuclear radius and ζ a parameter to evaluate by fitting.

Finally the actual d–d potential can be written as

$$V(r) = k_0 \frac{q^2}{r} \cdot \left(V(r)_{\mathrm{M}} - \frac{JKTR}{r} \right). \tag{17}$$

In this presentation, according to the coherence theory of condensed matter, it is emphasized the role of potential (17) in the three different phases : α, β and γ.

So in this theoretical framework aims to clarify:

(1) what is *KT?*
(2) what is the role of electrons and ions plasma?

About the first point, according to the different deuteron–lattice configurations, *KT* can be:

(i) the loaded lattice temperature considering the deuterons in the α-phase,
(ii) ω_β considering the deuterons in β-phase,
(iii) ω_γ considering the deuterons in the γ-phase.

Whereas regarding the second point, the question is trickier.

In fact the lattice environment is a mix of coherent plasmas (ion Pd, electron and deuterons plasma) at different temperature, due to different masses, thus describing an emerging potential becomes a very hard task. The method proposed in this presentation considers the total screening contribution of lattice environment in a D–D interaction (i.e. V_{tot}) as random potential $Q(t)$. So this model can be written as

$$V_{\mathrm{tot}}(t) = V(r) + Q(t). \tag{18}$$

And assuming that

$$\langle Q(t) \rangle_{\mathrm{t}} \neq 0 \tag{19}$$

that is, $Q(t)$ is now supposed to be (as a second order potential contribution) a periodic potential (the frequency will be labeled by ω_Q) that oscillates between the maximum value $Q_{\max}$ and 0.

Further specifically, the charge oscillations of d-shell electrons produce a screening potential having harmonic features:

$$eV(r) = -Z_d \frac{ke^2}{2a_0} r^2. \tag{20}$$

In [1] putting $Z_{\mathrm{d}} = 10/3$ and $a_0 = 0.7$ Å , it is evaluated a screening potential V_0 of about 85 eV. Computing this way you get $\rho \mathrm{g} V_0/26.9$ and, at least, $\rho = 0.165$ Å.

According to the loading ratio, within a palladium lattice the following cases occur.

(1) α-phase

In the phase α the deuterons are in a molecular state and the thermal motion is about
0.02 eV $< \hbar\omega_\alpha <$ 0.1 eV.
This phase takes places when x is less than 0.1, and since $W(t)$ is zero, the
D–D potential is

$$V(r) = k\frac{q^2}{r} \cdot \left(V_{\mathrm{M}}(r) - \frac{J\hbar\omega_\alpha R}{r} \right). \tag{21}$$

Equation (21) has been partially evaluated in a previous page [6] but only considering the dependence of tunneling probability on impurities present within lattice.

(2) β-phase

When x is bigger than 0.1 but less then 0.7, phase β occurs. The interaction takes place between deuteron ions that oscillate within the following energy values:
0.1 eV $< \hbar\omega_\beta <$ 0.2 eV.
In this case $W(t)$ is zero, so the potential is given by Eq. (22):

$$V(r) = k\frac{q^2}{r} \cdot \left(V_{\mathrm{M}}(r) - \frac{J\hbar\omega_\beta R}{r} \right). \tag{22}$$

Comparing Eqs. (21) and (22), it seems quite obvious that the weight of impurities is more important in the β-phase.

The role of temperature on tunneling effect has yielded to such conclusion according to the previous Refs. [6,7].

(3) γ-phase

Finally when the loading ratio is higher than 0.7, the deuteron–palladium system is in the phase γ.

This is the more interesting case. The deuterons undergo the screening due to d-shell electrons, therefore the D–D potential must be calculated assuming that the wall present in potential (13), due to Morse contribution, disappears. In fact if we use a classic plasma model where the D^+ ions are the positive charges and the d-electrons the negative, it is very reasonable to suppose that the following potential must be used:

$$V(r,t) = k\frac{q^2}{r} \cdot \left(V_{\mathrm{M}}(r) - \frac{J\hbar\omega_\gamma R}{r} \right) + Q(t). \tag{23}$$

We emphasize that $Q(t)$ is an unknown perturbative potential. It should be pointed out that

$$\langle Q(t) \rangle_{\mathrm{t}} \approx \frac{W_{\max}}{\sqrt{2}}. \tag{24}$$

As previously said, the screening potential, due to d-electrons is supposed to reduce the repulsive barrier, i.e. ρ and r_0'.

$$\langle Q(t) \rangle_{\mathrm{t}} \approx 85 \text{ eV}. \tag{25}$$

5. Results and Discussions

This presentation shows the D–D fusion probability renormalized to number of events per second regarding the D–D interaction in each different phase. More specifically, fusion probabilities in the phase α, β and γ are compared at varying states of energy between –50 and 50 eV. It is also important to consider the role of d-shell electron screening as perturbative lattice potential. This treatment, which considers only the case where $Q(t)$ is different by zero, involves a change of value of certain points in the x-axes where the coulomb barrier is represented and, in this case, the final result is the screening enhancement of fusion probability. In order to evaluate the fusion rate (Λ) this equation was required:

$$\Lambda = A\Gamma, \tag{26}$$

where Γ is the Gamow factor and A is the nuclear reaction constant obtained from the measured cross sections (value used was $10^{22}\mathrm{s}^{-1}$).

From an experimental point of view, in the cold fusion phenomenon it is possible to affirm that there are three types of experiment [13]:

(1) those that give negative results,
(2) those that give some results (little detection signs are measured in contrast with the background, therefore fusion probability is found to be about 10^{-23} using a very high loading ratio),
(3) those that give clear positive results as Fleischmann and Pons experiments.

Nevertheless, experiments of the third type are less accurate from an experimental point of view. For this reason it is possible to explain only the experiments of the first and second type throughout a physical and mathematical theoretical model of controversial phenomenon of cold fusion. In this case the role of loading ratio needs to be considered on the experimental results.

Starting from α-phase:

In this case the theoretical fusion probability is very small, less than 10^{-74}. It is possible to affirm that if the deuterium is loaded with a percentage $x < 0.2$ no fusion event occurs. The same absence of nuclear phenomenon is compatible for a loading ratio of about 0.7 since, in this case, the predicted fusion probability is less than 10^{-42}. These predictions, of course, agree to the experimental results. But for $x > 0.7$ a set of valid experiments on cold fusion report some background spikes (e.g. see [14]). The remarkable result of such model is that in the γ-phase, some background fluctuations are evident, since the theoretical predictions yielded to a fusion probability of about 10^{-22} due to a very high loading ratio. This represents a new result according to [6,7] since, in those cases, the fusion probability was independent by the loading ratio.

Moreover, the model proposed in this work (which unifies nuclear physics with condensed matter) can explain some anomaly nuclear traces found in the solids. In order to explain the occurrence of a very high fusion rate concerning the experiments of the third type, other contribution as micro-deformation would be required as long as the experiment itself could be possible. The role of micro-crack and impurities associated with the loading ratio will be explored in other speculative works. Hopefully *the nuclear physics within condensed matter* will be a new and highly productive scientific topic.

References

[1] O. Reifenschweiler, Reduced radioactivity of tritium in small titanium particles, *Phys. Lett. A* **184** (1994)149.
[2] O. Reifenschweiler, Some experiments on the decrease of tritium radioactivity, *Fusion Technol.* **30** (1996) 261.
[3] Melvin H. Miles et al., Introduction to the cold fusion experiments, *Fusion Technol.* **25** (1994) 478.

[4] G. Preparata, *QED Coherence in Matter*, Ch. 8, World Scientific, Singapore, 1995.
[5] Y. Iwamura, Detection of anomalous elements, X-ray and excess heat induced by continuous diffusion of deuterium through multi-layer cathode (Pd/CaO/Pd), ICCF-7, Vancouver, 1998.
[6] D. Morrison, The rise and decline of cold fusion, Physics World, 1990.)
[7] S. Aiello et al., Nuclear fusion experiment in palladium charged by deuterium gas, *Fusion Technol.* **18** (1990)323.
[8] F. Frisone, Deuteron interaction within a micro-crack in a lattice a room temperature, *Fusion Technol.* **39** (2001) 260.
[9] F. Frisone, Theoretical model of the probability of fusion between deuterons within deformed crystalline lattices with micro-cracks at room temperature, *Fusion Technol.* **40** (2001) 139.
[10] M. Fleishmann et al., Electro chemically induced nuclear fusion of deuterium, J. Electroanal. Chem. **261** (1989) 301–308.
[11] A. De Ninno et al., Evidence of emission of neutrons from a titanium–deuterium system, Europhys. Lett. A, 9 (1989) 221–224.
[12] G. Mengoli et al., The cycle life of 50/50 TiFe alloy electrodes for charge storage, *J. Electroanal. Chem.* **350** (1989) 57
[13] C. DeW Van Siclen and S.E. Jones, On muon catalyzed and cold fusion, *J. Phys. G. Nucl. Phys.* **12** (1986) 137.
[14] M. Baldo and R. Pucci, Relaxation toward equilibrium in plasmon-enhanced fusion, Fusion Technol. 18 (1990) 347.

J. Condensed Matter Nucl. Sci. 17 (2015) 35–66

Research Article

Empirical Models for Octahedral and Tetrahedral Occupation in PdH and in PdD at High Loading

Peter L. Hagelstein*

Massachusetts Institute of Technology, Cambridge, MA 02139, USA

Abstract

High D/Pd loading is known to be a requirement for producing excess heat in the Fleischmann–Pons experiment, and much work has in recent years been focused on electrochemical protocols and cathode processing in order to achieve D/Pd loadings approaching unity routinely. However, we know very little about PdD at a loading near unity, and almost nothing about what happens when the loading exceeds unity. It may be that when the octahedral sites are fully occupied, additional interstitial deuterium atoms occupy tetrahedral sites, a proposal which at this point has little experimental support. It is nevertheless possible to construct an empirical model for this scenario, and to make use of available experimental data to fit the associated model parameters. We worked with empirical models for both PdD and PdH that assume an O-site energy quadratic in loading, and an O-site to T-site excitation which is either constant in loading, or else taken as an empirical function fit to estimates inferred from the analysis of experimental data. There are two empirical models, each with four or more free parameters; and insufficient experimental data from which to choose each parameter or function independently. We add supplementary constraints that presume the models for PdH and PdD must be very similar, which reduces the number of degrees of freedom within the models. This allows data from PdH to be used to construct a model for PdD, and vice versa. The models which result are interesting; they suggest these complicated systems might be understood based on a simple underlying picture; they indicate that there is more T-site occupation than has been appreciated previously in the literature; they indicate that the resistance ratio calibrations for PdH and PdD are inconsistent; and finally, measurements of the chemical potential at high loading have the potential to provide information about the O-site to T-site excitation energy.
 ISSN 2227-3123

Keywords: Empirical models, Resistance ratio, Solubility of PdH and PdD at high loading, Statistical mechanics model, Tetrahedral occupation

1. Introduction

We have been interested for many years in understanding the origin of the excess heat effect in the Fleischmann–Pons experiment, where a large amount of thermal energy is observed, with no commensurate chemical or energetic nuclear products observed [1,2]. We have long recognized that there must be new physical mechanisms involved, and along with many others we have put in much effort seeking to understand associated microscopic mechanisms [3,4]. Additionally,

*E-mail: plh@mit.edu

 ISSN 2227-3123

we have been interested in developing a simulation model for excess heat production, which involves a combination of known physics along with new physics. In this work our focus is on conventional physics issues connected with the octahedral and tetrahedral occupation of PdD at high loading.

It was understood by Fleischmann and Pons in 1989 that the D/Pd loading needed to be high in order for excess heat to be observed. Subsequently, two different loading requirements were identified. It was observed in experiments at SRI and ENEA Frascati that cathodes which did not reach a D/Pd loading in the vicinity of 0.95 at some point during their loading history were unlikely to produce excess heat [5–7]. For a cathode with did reach this very high loading, excess heat could be seen subsequently at more modest loading; however, excess heat was observed to increase with loading above a threshold in the vicinity of 0.83 [8–10].

Because of these observations, much attention has been focused on achieving high loading [11]; electrochemical protocols suitable for achieving high loading [12–16]; the problem of developing cathodes that can load well [14,15,17]; and materials science studies [18,19]. Measurements of the D/Pd loading can be done conveniently based on the resistance ratio [20–25], which has in recent years been determined to a D/Pd loading greater than unity. X-ray diffraction measurements have been reported [26–29], including measurements of samples loaded near unity [29].

This work has motivated our interest in some of the associated theoretical issues. For example, one might ask why there should be any requirements on the D/Pd loading in the first place. The question of what it is that happens in the experiment when the D/Pd loading reaches either 0.83 or 0.95 also come to mind [3,30,31]. Our interest in this work is focused on the deuterium chemical potential and site occupation when the D/Pd loading is in the vicinity of unity, or reaches even higher loadings.

From earlier experimental work, we know that hydrogen and deuterium atoms occupy interstitial octahedral sites in the FCC PdH or PdD lattice [32–35]. Such a picture is consistent with theoretical models that have been studied over the years [36–41]. The basic picture of highly loaded PdD at room temperature as an FCC lattice with NaCl-type structure, with deuterium atoms in the octahedral site (see Fig. 1), has provided one of the cornerstones for studies of PdH and PdD, and also for our field as well. Such a picture is useful as long as the tetrahedral occupancy is low; in this connection we draw attention to a calculation of the tetrahedral occupation as a function of pressure by Christensen et al. [40], which shows negligible tetrahedral occupation for D/Pd$<$1 even at very high pressure.

We are interested in the question of what happens when the D/Pd loading ratio exceeds unity, for example as has

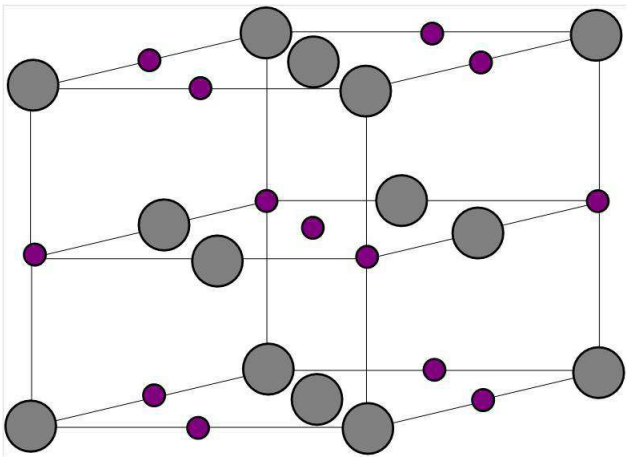

Figure 1. FCC lattice model for PdD; the large grey atoms in the figure are Pd, and the small purple atoms are D.

been claimed to have been achieved in high pressure experiments [42] up to 3.1 GPa. Note that there is not uniform agreement in the literature that the D/Pd loading can exceed unity under such conditions; for example, Hemmes et al. [43] models an H/Pd ratio less than unity for pressures up to 100 GPa. Sugimoto and Fukai model a variety of FCC metal hydrides up to 100 GPa, with no need for going above an H/Me ratio of unity [44].

However, if a D/Pd loading greater than unity can be achieved, then the question of where the extra deuterium atoms go in the lattice becomes important. Historically, this issue has largely been the focus of speculation. One possibility is that additional deuterium atoms occupy interstitial tetrahedral sites, once all of the octahedral sites are occupied [45–48]. Another suggestion is that double occupancy of octahedral sites occurs [49,50]. Such a suggestion seems unlikely since we would expect the occupation of anti-bonding orbitals which would tend to push the deuterium atoms apart [40] (although in the presence of a Pd vacancy this issue is removed [31]). In what follows, we examine simple models for tetrahedral occupation both for a D/Pd ratio less than unity as well as for D/Pd greater than 1.

Palladium vacancies become stabilized at high H/Pd loading, which was taken advantage of by Fukai and Okuma [51] to create a new phase with superabundant vacancies which we can write as $Pd_{0.75}H$. That this phase is thermodynamically favored at high loading suggests that we ought to at least be aware of the phase in connection with our discussion of D/Pd ratios in excess of unity. For example, in equilibrium we would expect the vacancy phase have a big impact on the phase diagram in this case; however, near room temperature vacancy diffusion is extremely slow so that one would not expect the vacancy phase to form through this mechanism over the course of an experiment. Nevertheless, one could imagine that if the D/Pd loading were sufficiently high then sufficient energy could be present to drive a phase change much more rapidly; as yet we are not aware of experimental evidence for this.

These arguments ultimately lead us back to a picture in which tetrahedral site occupation must be contemplated then when the D/Pd loading is sufficiently high. Within this picture a new set of issues arise. The first concerns how large the excitation energy is for O-site to T-site excitation. For example, if the excitation energy is large, then we would expect to see little T-site occupation for D/Pd < 1, and then a large increment in pressure would be required to push the D/Pd loading above unity. On the other hand, if the excitation energy is more modest, then we might expect to see some tetrahedral occupation in the accessible D/Pd < 1 regime, and the regime with a D/Pd loading greater than unity should be accessible in high pressure experiments and also in electrochemical experiments.

In what follows, our focus is on the development of an empirical model for PdD at high loading. Unfortunately, there is probably not sufficient relevant data available from experiment in order to specify such a model to the degree that we might be satisfied with. However, if we broaden our perspective to include the simultaneous development of a similar model for PdH, then the situation improves significantly, given certain assumptions as to how different the model for PdD should be from the model for PdH.

2. Simple Empirical Model for O-site and T-site Occupation

In order to connect with experiment in the case of highly loaded PdD we need to construct a statistical mechanics model for O-site and T-site occupation, with site energies which depend on the D/Pd loading. We also need to account for statistical factors associated with the electronic spin, nuclear spin, and excited state degeneracy of the interstitial atoms in the O-sites and T-sites. Our first order of business then is to assemble a set of basic relations between the deuterium chemical potential and the occupation of octahedral and tetrahedral sites.

The development of the basic thermodynamic relations is straightforward; but the specification of empirical models for how the site energies depend on the D/Pd loading is not. One might argue that it should be possible to take advantage of theory in order to understand how the site energies depend on the D/Pd loading. As we will see, the precision required to obtain a useful empirical model is beyond the current state of the art. Consequently, we will need to turn to experiment in order to develop model parameters. Fortunately we have available some measurements which are helpful; these will be considered in subsequent sections, along with the fitting of model parameters to the data.

2.1. Model partition function

The starting point for the thermodynamics model is a canonical partition function which roughly follows the approach of Lacher [36] given by

$$Q = \sum_{M_T} \sum_{M_O} \frac{(N_O + N_T)!}{M_O!(N_O - M_O)!M_T!(N_T - M_T)!} z_O^{M_O} z_T^{M_T} e^{-(M_O E_O + M_T E_T)/k_B T}, \tag{1}$$

where z_O and z_T are deuterium atom partition functions associated with O-site and T-site occupation. This approach is discussed by Orondo [55]; we have generalized it to include an appropriate multinomial coefficient for the partition of deuterium atoms into O-sites and T-sites. In this formula N_O and N_T are the number of O-sites and T-sites available, and M_O and M_T are the number of deuterium atoms in O-sites and T-sites.

The partition functions for the O-site and T-site are taken to be [52]

$$\begin{aligned} \text{PdH}: \quad & z_O = z_T = 2 \times 2 \left[\sum_n \exp\left\{ -\frac{E_n}{k_B T} \right\} \right]^3, \\ \text{PdD}: \quad & z_O = z_T = 2 \times 3 \left[\sum_n \exp\left\{ -\frac{E_n}{k_B T} \right\} \right]^3 \end{aligned} \tag{2}$$

with

$$E_n = \hbar \omega_{O,T} n^s \tag{3}$$

and

$$\begin{aligned} \text{PdH}: \quad & \hbar\omega_O = 69.0 \text{ meV}, \quad s_O = 1.2, \\ \text{PdH}: \quad & \hbar\omega_T = 53.8 \text{ meV}, \quad s_T = 1.2, \\ \text{PdD}: \quad & \hbar\omega_O = 46.5 \text{ meV}, \quad s_O = 1.2, \\ \text{PdH}: \quad & \hbar\omega_T = 39.0 \text{ meV}, \quad s_T = 1.2. \end{aligned} \tag{4}$$

The O-site partition function was developed from fits to results from inelastic neutron scattering [53]. The T-site partition function was selected to have the same s_T value, and was otherwise optimized fit in the analysis of solubility data for α-phase PdH_x and PdD_x [52].

In the D_2 chemical potential model that we make use of as in reference [54], we presumed a singlet electronic ground state with statistical weight 1 for the molecule; in a simple picture for atomic deuterium in the lattice the electronic spin degeneracy could reasonably be taken to be 2. For the molecule, we included the nuclear spin degeneracy which was reduced by the generalized Pauli principle; now we can keep track of the full nuclear spin degeneracy of the spin 1 deuterons. Analogous arguments apply in the case of PdH. The site energies E_O and E_T are assumed to vary with loading, with the temperature constant at 300 K in this study.

2.2. Deuterium chemical potential in the solid phase

For the chemical potential of O-site deuterium atoms we can write

$$-\frac{\mu_{\rm O}}{k_{\rm B}T} = \frac{\partial}{\partial M_{\rm O}} \ln\left\{ \frac{(N_{\rm O}+N_{\rm T})!}{M_{\rm O}!(N_{\rm O}-M_{\rm O})!M_{\rm T}!(N_{\rm T}-M_{\rm T})!} z_{\rm O}^{M_{\rm O}} z_{\rm T}^{M_{\rm T}} {\rm e}^{-(M_{\rm O}E_{\rm O}+M_{\rm T}E_{\rm T})/k_{\rm B}T} \right\}. \tag{5}$$

A similar expression occurs now for the T-site deuterium atoms

$$-\frac{\mu_{\rm T}}{k_{\rm B}T} = \frac{\partial}{\partial M_{\rm T}} \ln\left\{ \frac{(N_{\rm O}+N_{\rm T})!}{M_{\rm O}!(N_{\rm O}-M_{\rm O})!M_{\rm T}!(N_{\rm T}-M_{\rm T})!} z_{\rm O}^{M_{\rm O}} z_{\rm T}^{M_{\rm T}} {\rm e}^{-(M_{\rm O}E_{\rm O}+M_{\rm T}E_{\rm T})/k_{\rm B}T} \right\}. \tag{6}$$

The partial derivatives can be evaluated approximately in the limit that a macroscopic number of sites and deuterium atoms is involved to yield [55]

$$\begin{aligned}\mu_{\rm O} &= E_{\rm O} + M_{\rm O}\frac{\partial}{\partial M_{\rm O}}E_{\rm O} + M_{\rm T}\frac{\partial}{\partial M_{\rm O}}E_{\rm T} - k_{\rm B}T\ln\frac{N_{\rm O}-M_{\rm O}}{M_{\rm O}} - k_{\rm B}T\ln z_{\rm O} \\ &= E_{\rm O} + \theta_O\frac{\partial}{\partial \theta_O}E_{\rm O} + \theta_{\rm T}\frac{\partial}{\partial \theta_O}E_{\rm T} - k_{\rm B}T\ln\frac{1-\theta_O}{\theta_O} - k_{\rm B}T\ln z_{\rm O},\end{aligned} \tag{7}$$

$$\begin{aligned}\mu_{\rm T} &= E_{\rm T} + M_{\rm T}\frac{\partial}{\partial M_{\rm T}}E_{\rm T} + M_{\rm O}\frac{\partial}{\partial M_{\rm T}}E_{\rm O} - k_{\rm B}T\ln\frac{N_{\rm T}-M_{\rm T}}{M_{\rm T}} - k_{\rm B}T\ln z_{\rm T} \\ &= E_{\rm T} + \theta_{\rm T}\frac{\partial}{\partial \theta_{\rm T}}E_{\rm T} + \theta_O\frac{\partial}{\partial \theta_{\rm T}}E_{\rm O} - k_{\rm B}T\ln\frac{2-\theta_{\rm T}}{\theta_{\rm T}} - k_{\rm B}T\ln z_{\rm T}.\end{aligned} \tag{8}$$

In these formulas $E_{\rm O}$ and $E_{\rm T}$ depend on the O-site and T-site loading, as well as on the temperature. The O-site and T-site occupation fractions are referenced to the number of Pd atoms in the absence of vacancies, which is the same as the number of O-sites

$$\theta_{\rm O} = \frac{M_{\rm O}}{N_{\rm O}} = \frac{M_{\rm O}}{N_{\rm Pd}}, \tag{9}$$

$$\theta_{\rm T} = \frac{M_{\rm T}}{N_{\rm O}} = \frac{M_{\rm T}}{N_{\rm Pd}}. \tag{10}$$

According to these definitions the O-site fractional occupation $\theta_{\rm O}$ varies between 0 and 1, while the T-site fractional occupation $\theta_{\rm T}$ varies between 0 and 2. In equilibrium the different chemical potentials are equal

$$\mu_{\rm O} = \mu_{\rm T} = \mu_{\rm D}. \tag{11}$$

We note in connection with this discussion the approach of Ref. [56].

2.3. Reduction of the model

If the first-principles theoretical models were sufficiently good, then we could make use of the results of density functional calculations to determine how the O-site and T-site energies depend on the distribution of the atoms among the different sites, at least on average. From previous experience with such calculations, we know that the average configuration energies from Quantum Espresso calculations can be off by more than 100 meV [55,57]. While the agreement between DFT theory and experiment must be considered in this case to be excellent (given how difficult the calculation is), such a level of agreement is not useful for the modeling under consideration here.

To simplify things for the development of a useful empirical model, we will assume that the site energies depend on the total D/Pd loading (fractional interstitial occupation) θ

$$\theta = \theta_{\rm O} + \theta_{\rm T}. \tag{12}$$

The total loading θ under these definitions varies between 0 and 3. In this case, our thermodynamic relations reduce to

$$\mu_{\rm D} = E_{\rm O} + \theta_{\rm O}\frac{\partial E_{\rm O}}{\partial\theta} + \theta_{\rm T}\frac{\partial E_{\rm T}}{\partial\theta} - k_{\rm B}T\ln\frac{1-\theta_{\rm O}}{\theta_{\rm O}} - k_{\rm B}T\ln z_{\rm O}, \tag{13}$$

$$\mu_{\rm D} = E_{\rm T} + \theta_{\rm T}\frac{\partial E_{\rm T}}{\partial\theta} + \theta_{\rm O}\frac{\partial E_{\rm O}}{\partial\theta} - k_{\rm B}T\ln\frac{2-\theta_{\rm T}}{\theta_{\rm T}} - k_{\rm B}T\ln z_{\rm T}. \tag{14}$$

In writing this we presume that the site energies $E_{\rm O}$ and $E_{\rm T}$ depend on loading θ and on temperature.

2.4. Inclusion of PdV terms

The lattice expands by an incremental volume V_D when a deuterium atom enters the lattice. If the lattice is in deuterium gas, this expansion does work on the gas. We can take this effect into account by augmenting the model chemical potential with PdV terms according to

$$\mu_{\rm D} = E_{\rm O} + \theta_{\rm O}\frac{\partial E_{\rm O}}{\partial\theta} + \theta_{\rm T}\frac{\partial E_{\rm T}}{\partial\theta} - k_{\rm B}T\ln\frac{1-\theta_{\rm O}}{\theta_{\rm O}} - k_{\rm B}T\ln z_{\rm O} + PV_{\rm D}, \tag{15}$$

$$\mu_{\rm D} = E_{\rm T} + \theta_{\rm T}\frac{\partial E_{\rm T}}{\partial\theta} + \theta_{\rm O}\frac{\partial E_{\rm O}}{\partial\theta} - k_{\rm B}T\ln\frac{2-\theta_{\rm T}}{\theta_{\rm T}} - k_{\rm B}T\ln z_{\rm T} + PV_{\rm D}. \tag{16}$$

where $V_{\rm D}$ is about 2.9 Å^3 (we will adopt the save incremental volume for hydrogen). At low pressure these terms contribute very little, which is why they are usually neglected; however at high pressure in the vicinity of 1 GPa the PdV terms have a noticeable impact on the solubility.

2.5. Site energy models and temperature independence

The models above are reasonably general, and one might make use of them in connection with a sophisticated model with temperature-dependent site energies that are nonlinear in loading. We are interested in reducing the model even further (in order to reduce the number of degrees of freedom) in order to apply to restricted conditions. To this end, we consider a version for use under constant temperature conditions where the site energies are locally quadratic in the loading θ. It will be convenient to use a parameterization for the O-site energy given by

$$E_{\rm O}(\theta) = E_{\rm O}(\theta_0) + (\theta - \theta_0)E'_{\rm O}(\theta_0) + \frac{1}{2}(\theta - \theta_0)^2 E''_0(\theta_0). \tag{17}$$

We will take (somewhat arbitrarily)

$$\theta_0 = 0.60, \tag{18}$$

which is near the β-phase boundary of the miscibility gap.

We parameterize the T-site energy according to

$$E_{\rm T}(\theta) = E_{\rm O}(\theta) + \Delta E(\theta). \tag{19}$$

We see in this that the T-site energy is referenced to the O-site energy, with an O-site to T-site excitation energy specified as $\Delta E(\theta)$. In what follows we will consider a version of the model with constant excitation energy, and later on a more sophisticated version of the model with $\Delta E(\theta)$ chosen to match values inferred from experimental measurements.

2.6. Supplemental constraints

We see that there are three parameters and one function to be specified for an empirical model for loading in PdD, and three additional parameters and another function to be specified for an analogous empirical model for loading in PdH. From our perspective, the experimental data set that is available is insufficient to determine the 6 parameters and two functions required for the two models under consideration.

It is possible to reduce the number of free parameters by adding supplementary constraints on the parameters for PdD and PdH. It has been noted in the literature that the pressure as a function of loading curves for PdH and PdD in the β-phase region are offset from one another, but otherwise are very similar. We will take the liberty of presuming that this similarity extends for the O-site energy over the entire range of interest, which leads to the supplementary constraints

$$E'_{\rm O}(\theta)\Big|_{\rm PdH} = E'_{\rm O}(\theta)\Big|_{\rm PdD} \tag{20}$$

$$E''_{\rm O}(\theta)\Big|_{\rm PdH} = E''_{\rm O}(\theta)\Big|_{\rm PdD}. \tag{21}$$

For the O-site to T-site excitation energy, it would be reasonable to assume that the energy difference differs by the zero point energy

$$\Big[\Delta E(\theta)\Big]_{\rm PdH} = \Big[\Delta E(\theta)\Big]_{\rm PdD} + \Delta E_{\rm zp}. \tag{22}$$

The difference found for the α-phase does not match this requirement [52], but is not far off. In what follows we will make use of the experimental energy difference as best we know it, and use this relation as a check.

The biggest difficulty in the development of empirical models is in determining relevant constraints that can reduce the number of degrees of freedom that need to be specified. By supplementing our model with these constraints, we have reduced the number of degrees of freedom.

2.7. Chemical potential of deuterium in the gas phase

To proceed, we will need to evaluate the chemical potential; for this we write [55,58]

$$\mu_{\rm D} = \frac{1}{2}\mu_{\rm D_2} = \frac{1}{2}\mu_{\rm nonideal} - \frac{1}{2}k_{\rm B}T\ln z_{\rm rotvib} - \frac{E_{\rm d}}{2}, \tag{23}$$

where the nonideal contribution to the chemical potential is

$$\mu_{\rm nonideal} = k_{\rm B}T\ln\left[\frac{f}{k_{\rm B}T}\left(\frac{2\pi\hbar^2}{Mk_{\rm B}T}\right)^{3/2}\right]. \tag{24}$$

For the rotational and vibrational partition function we have

$$\mathrm{H_2}\text{:}\quad z_{\rm rotvib} = 1\sum_{\text{even } l}\sum_{n}(2l+1)\,{\rm e}^{-E_{nl}/k_{\rm B}T} + 3\sum_{\text{odd } l}\sum_{n}(2l+1)\,{\rm e}^{-E_{nl}/k_{\rm B}T}, \tag{25}$$

$$\mathrm{D_2}\text{:}\quad z_{\rm rotvib} = 6\sum_{\text{even } l}\sum_{n}(2l+1)\,{\rm e}^{-E_{nl}/k_{\rm B}T} + 3\sum_{\text{odd } l}\sum_{n}(2l+1)\,{\rm e}^{-E_{nl}/k_{\rm B}T}. \tag{26}$$

We made use of the fits of Urey and Rittenberg [59] for the rotational and vibrational energy levels. We note that the nuclear spin degrees of freedom are included explicitly in these relations [54]. To model the fugacity, we have available the model of Joubert for H_2 [60], and the model of Joubert and Thiebaut [61] for D_2. We have chosen in this case to use the H_2 model of Joubert [60] in both cases, in light of the discussion in Ref. [62]. The deuterium chemical potential that results in the case of PdD is shown in Fig. 2.

2.8. Matching with experiment at modest pressure

The pressure as a function of loading has been studied for both PdD and PdH in gas loading experiments at modest D_2 and H_2 pressure, and the resulting $P-C-T$ curves are reasonably well known [64]. These pressure versus loading curves are reasonably well fit by the empirical solubility relations given by Baranowski et al. [42]

$$\ln f_{\rm H_2} = -\frac{(100.4-90.1\theta)\ (\text{kJ mol}^{-1})}{RT} + \frac{106.4\ (\text{J mol}^{-1}\text{K}^{-1})}{R} + 2\ln\frac{\theta}{1-\theta}, \tag{27}$$

$$\ln f_{\rm D_2} = -\frac{(95.6-90.1\theta)\ (\text{kJ mol}^{-1})}{RT} + \frac{106.4\ (\text{J mol}^{-1}\text{K}^{-1})}{R} + 2\ln\frac{\theta}{1-\theta}. \tag{28}$$

The resulting pressure versus loading curves are shown in Fig. 3. One can see that the two curves are parallel with an offset.

If we presume no T-site occupation, and that the O-site energy is linear in the total loading θ, then we can obtain estimates for four of the empirical model parameters

$$\text{PdH}:\quad E_{\rm O}(\theta_0) - k_{\rm B}T\ln z_{\rm O} + \frac{E_{\rm D}}{2} = -391.8\ \text{meV},\quad E'_{\rm O}(\theta_0) = 233.5\ \text{meV}, \tag{29}$$

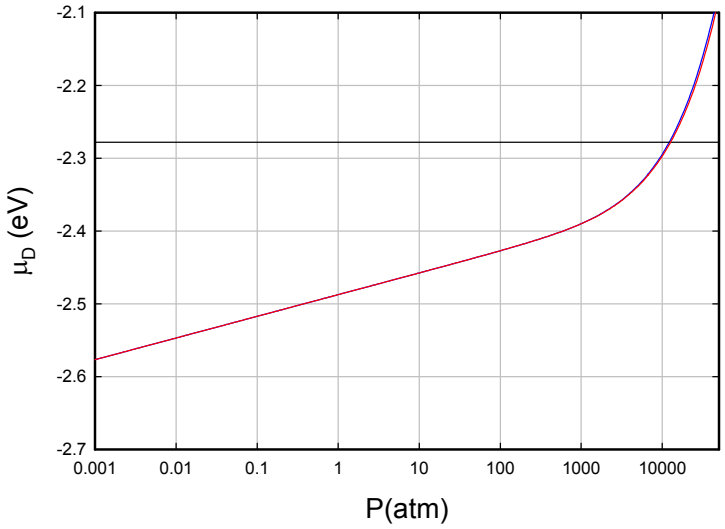

Figure 2. Deuterium chemical potential at 300 K as a function of pressure; with the D_2 fugacity from [59] (red line); with the H_2 fugacity from [60] (blue line); and half the dissociation energy $-E_d/2$ (black line).

$$\text{PdD}: \quad E_O(\theta_0) - k_B T \ln z_O + \frac{E_D}{2} = -399.1 \text{ meV}, \quad E'_O(\theta_0) = 233.5 \text{ meV}. \tag{30}$$

The slope parameters are the same here due to the construction of the empirical fits of Baranowski et al. [42] above. We used for the dissociation energy of H_2 2×2.23899 eV, and for the dissociation energy of D_2 2×2.27806 eV.

We can estimate the contribution of the $k_B T \ln z_O$ factors using a 3D SHO model to be

$$\text{PdH}: \quad k_B T \ln z_O = 41.4 \text{ meV}, \tag{31}$$

$$\text{PdD}: \quad k_B T \ln z_O = 60.4 \text{ meV}. \tag{32}$$

The corresponding estimates for $E_O(\theta_0)$ are

$$\text{PdH}: \quad E_O(\theta_0) + \frac{E_D}{2} = -350.4 \text{ meV} \quad \text{(SHO)}, \tag{33}$$

$$\text{PdD}: \quad E_O(\theta_0) + \frac{E_D}{2} = -338.8 \text{ meV} \quad \text{(SHO)}. \tag{34}$$

If we make use of the non-SHO partition functions given above (from Ref. [52]) we obtain

$$\text{PdH}: \quad E_O(\theta_0) + \frac{E_D}{2} = -350.6 \text{ meV} \quad \text{(non} - \text{SHO)}, \tag{35}$$

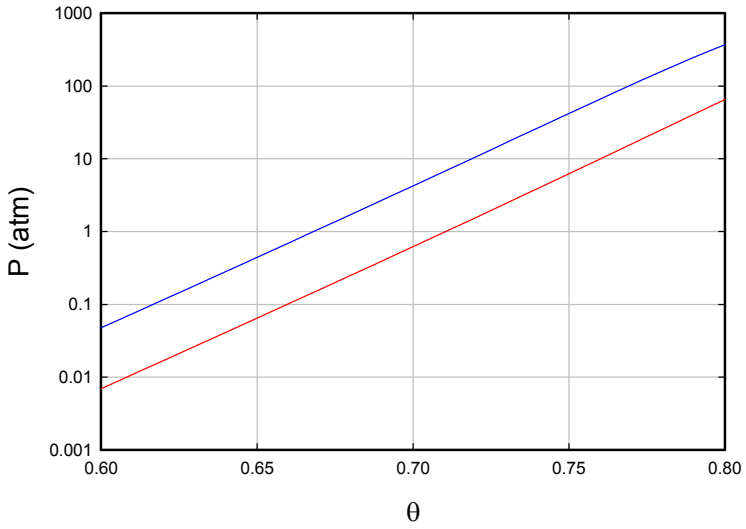

Figure 3. Equilibrium pressure at 300 K as a function of loading based on the parameterization of Baranowski et al. [42] for PdH (red line) and PdD (blue line).

$$\text{PdD}: \quad E_{\rm O}(\theta_0) + \frac{E_{\rm D}}{2} = -339.8 \text{ meV} \quad (\text{non} - \text{SHO}). \tag{36}$$

We might have expected to see a difference between PdH and PdD due to the zero-point energy contribution (which is estimated to be 31 meV by Ke and Kramer [63]); however the results here are much closer.

2.9. Fitting PdH at higher pressure

We would like to extend this general approach to higher loading if possible; unfortunately we lack systematic pressure versus loading data at higher pressure. There are some high pressure measurements of PdH that were reported by Tkacz and Baranowski [65] that look to be useful in the context of the present analysis. In this work data points are reported at H/Pd loadings between 0.90 and 0.995. Since our focus at the moment is on the O-site energy, we propose here to make use of the two data points with the lowest values of θ, as these have the best chance of being relatively free of tetrahedral occupation. It is possible to arrange for a weighted least squares fit based on

$$\mu_{\rm H} = E_{\rm O} + \theta_{\rm O}\frac{\partial E_{\rm O}}{\partial \theta} - k_{\rm B}T \ln \frac{1-\theta_{\rm O}}{\theta_{\rm O}} - k_{\rm B}T \ln z_{\rm O} + PV_{\rm H} \tag{37}$$

with results shown in Fig. 4. We see that the pressure versus loading curve that results looks very plausible. In this case the fitting parameters are

$$\text{PdH}: \quad E_{\rm O}(\theta_0) + \frac{E_{\rm D}}{2} = -385.8 \text{ meV}, \quad E'_{\rm O}(\theta_0) = 291.8 \text{ meV}, \quad E''_{\rm O}(\theta_0) = -150.3 \text{ meV}. \tag{38}$$

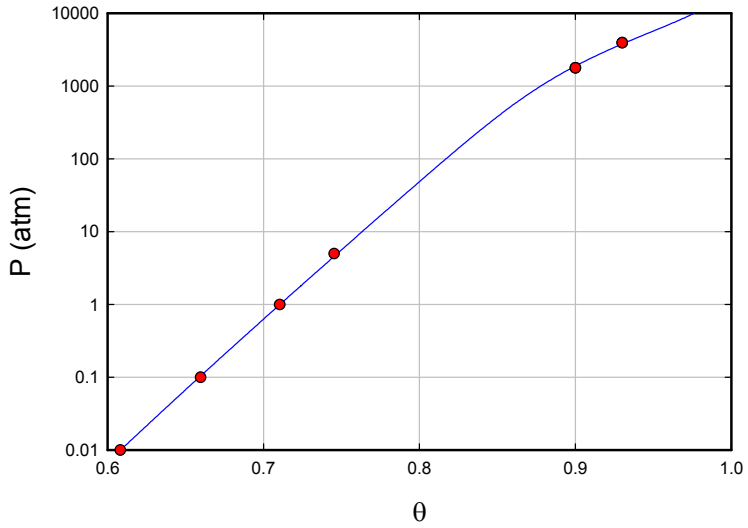

Figure 4. Least squares fit to selected pressure as a function of loading points for PdH at 300 K as a function of loading; points used for the fit (red circles); weighted least squares fit (blue line).

According to the supplemental constraints, we propose to develop an equivalent O-site energy model for PdD by shifting the O-site energy for PdH by a constant to match the pressure at the β-phase boundary; this leads to

$$\text{PdD}: \quad E_{\rm O}(\theta_0) + \frac{E_{\rm D}}{2} = -374.8 \text{ meV}, \quad E'_{\rm O}(\theta_0) = 291.8 \text{ meV}, \quad E''_{\rm O}(\theta_0) = -150.3 \text{ meV}. \tag{39}$$

2.10. Discussion

We are interested in the development of empirical models for the O-site and T-site energies in to be used in conjunction with an equilibrium statistical thermodynamics model for the O-site and T-site fractional occupation. In general one would like many degrees of freedom in an empirical model in order to develop the best match to the available experimental data sets. For our model it will not be straightforward to arrange for a unique determination of all of the parameters directly from experimental data, simply because we lack the relevant experimental measurements of PdD at high pressure, and we also lack experimental measurements of site-dependent occupancy at high loading.

The model under discussion assumes a quadratic dependence of the O-site energy on the total loading θ, and an O-site to T-site excitation energy that is to be discussed. There are six parameters and two functions to be specified for PdH and PdD. To reduce the number of free parameters we introduce supplementary constraints, which insures that the resulting models will differ only by offset energies. This allows us to make use of the high pressure measurements in PdH to estimate what happens in PdD at high pressure, below the point where T-site occupation becomes important. At this point we have initial estimates for the six parameters needed for our empirical models.

3. Input on T-site Occupation

At present there is no unambiguous direct experimental observation of bulk tetrahedral site occupation in equilibrium at high loading in PdH or PdD. Consequently, it has not been established conclusively what phase might be present in PdH or PdD above a loading of unity; only a few authors even claim to have observed PdH or PdD above a loading of unity. Nevertheless, we will proceed in what follows under the presumption that at high loading interstitial hydrogen or deuterium in equilibrium occupies tetrahedral sites.

The big issue in modeling T-site occupation is in determining the O-site to T-site excitation energy. This excitation energy has as yet not been determined experimentally. There are a number of theoretical calculations in the literature; however, there is a reasonably wide range of excitation energies predicted, and no reason to believe that the calculations are sufficiently accurate to be able to predict T-site occupation usefully. There is some neutron diffraction data which looks interesting at lower loading, which we consider in this section. The O-site to T-site excitation energy near a loading of unity will remain undetermined until the next section.

3.1. O-site to T-site excitation energy calculations

About 25–30 years ago, one could find literature values for the excitation energy near 300 meV [39,41]. Subsequently the problem has been addressed with embedded atom models, density functional calculations, and quantum chemistry calculations. A sizeable spread in the calculated O-site to T-site excitation energy is found, as shown in Table 1.

Based on this we might expect the O-site to T-site excitation energy near zero loading to be between about 50 and 295 meV, and that it probably increases with increasing loading.

3.2. Quasi-elastic neutron diffraction experiments

Tetrahedral occupation can be observed in quasi-elastic neutron diffraction experiments, which have been reported in the case of PdD. For example, if only O-sites are occupied, then the lattice structure is FCC which would be expected to give an associated FCC diffraction pattern. However, if significant tetrahedral occupation occurs, then the part of the diffraction pattern associated with the deuterons would would instead be consistent with the Fm3m space group. X-ray scattering is not useful in this application since deuterium atoms have no scattering power in the X-ray regime. The deuterium occupation can be determined then from the strength of the new neutron diffraction peaks that are not present in the FCC part of the spectrum.

Table 1. Energy difference (meV) between O-site and T-site occupation for different studies.

Reference	PdD/PdH	$\Delta E(\theta = 0)$	$\Delta E(\theta = 1)$
[39]	PdH	290	
[41]	PdD	295	350
[66]	PdH		213
[66]	PdD		150
[63]	PdD	50 ($\theta = 0.25$)	
[67]	PdH	80	
[68]	PdH	160	
[69]	PdH	160	
[70]	PdH	70	95
[55]	PdH		385
[71]	PdH	142	

An early attempt to determine tetrahedral occupation in this way was reported by Rotella et al. [72] in an electrochemical experiment near room temperature. Positive observations of diffraction lines from the Fm3m space group were reported by Pitt and Gray [73] in experiments done at 309°C, with comparable results subsequently obtained by McLennan et al. [74] in experiments done at similar temperatures. Negative results for tetrahedral occupation were found by Widenmeyer et al. [75] in experiments carried out at 177°C .

3.3. Role of monovacancies

We are confronted with a seeming contradiction where experiments which seem similar given different results. To make progress, it will be useful to have a picture in mind, and allow us to understand the model that results better.

We might begin with the measurements of Widenmeyer et al. [75] and assert somewhat arbitrarily that they argue they they tell us that there is no observable T-site occupation up to a D/Pd loading of 0.72 at a temperature of 177°C. We might take this one step further and assert that the data point that appears in Fig. 6 of Ref. [74] for a D/Pd loading of about 0.96 with a tetrahedral occupation somewhere between 0 and 2% at 25°C provides for the strictest experimental upper limit relevant for our model near stoichiometric loading.

If so, then what is the situation with the much higher levels of T-site occupation reported near 309°C in [73,74]? There are two possibilities. One is that the positive observations might be due (at least in part) to deuterium trapped in T-sites in monovacancies [76–78]. The idea is that if the sample was loaded reasonably well at elevated temperatures, then Pd vacancies become stabilized, and one might expect them to be able to form via atomic self-diffusion (vacancy diffusion) if the sample is held at elevated temperature sufficiently long [79]. We would expect deuterium to be trapped in vacancies, because the binding energy is be greater than for bulk O-site occupation. The O-site to T-site excitation energy in a monovacancy is known to be very small in the case of Ni [80], which is consistent with the relative occupation observed in Pd monovacancies [78].

Another possibility is that the observations reported by Pitt and Gray [73], and also by McLennan et al. [74], are basically correct. In this case one might argue that the O-site to T-site excitation energy is high in the β-phase, and also in the (dominant) β-phase component in the miscibility gap. If the sensitivity of the experiment of Widenmeyer et al. [75] were low, then the relatively weak signals from T-site occupation might not have been apparent.

Further experimentation will be required to resolve this issue. If we take the positive T-site observations as valid, then we end up with a model which looks to be generally consistent with what we found from an analysis of α-phase solubility data, and also what we will find shortly from high pressure experiments. If these neutron diffraction experiments are impacted by the presence of monovacancies, then our estimate for the excitation energy will be a lower bound (if diffraction from excited states contributes in equal measure to diffraction from the ground state).

3.4. Constraint on the O-site to T-site excitation energy

Given the discussion above, we propose to make use of the neutron diffraction measurements at lower temperature to provide a constraint on the O-site to T-site excitation energy at a D/Pd loading near unity. If we work with the low tetrahedral occupation observed at a D/Pd ratio of 0.96 at 25°C, we can use this to estimate an upper limit on the excitation energy at that loading and temperature.

For the analysis of a single D/Pd loading point, we can develop a local relation between the O-site to T-site excitation energy and the loading from the more general version of the model

$$\mu_D = E_O + \theta_O \frac{\partial}{d\theta} E_O + \theta_T \frac{\partial}{d\theta} E_T - k_B T \ln \frac{1-\theta_O}{\theta_O} - k_B T \ln z_O + P V_D,$$

$$\mu_{\rm D} = E_{\rm T} + \theta_{\rm T}\frac{\partial}{\partial d}E_{\rm T} + \theta_{\rm O}\frac{\partial}{d\theta}E_{\rm O} - k_{\rm B}T\ln\frac{2-\theta_{\rm T}}{\theta_{\rm T}} - k_{\rm B}T\ln z_{\rm T} + PV_{\rm D}$$

and subtract to obtain

$$E_{\rm T} - E_{\rm O} = k_{\rm B}T\left\{\ln\left(\frac{2-\theta_{\rm T}}{\theta_{\rm T}}\frac{\theta_{\rm O}}{1-\theta_{\rm O}}\right) + \ln\frac{z_{\rm T}}{z_{\rm O}}\right\}. \tag{40}$$

Results are shown in Table 2 (computed with the non-SHO partition functions). We do not know the lower limit of sensitivity in this experiment, so we have computed excitation energies for three possible low values of T-site occupation. We see that the O-site to T-site excitation energy must be greater than about 200 meV to be consistent with the low T-site occupation point in [74].

3.5. Estimate of excitation energies

In experiments of Pitt and Gray [73], and in experiments reported by McLennan et al. [74] positive observations of T-site occupation are reported. We would like to analyze the data point by point using an approach similar to the one used above. In this case we might assume either that we have deuterium occupation of T-sites, in which case we expect $E_{\rm T} - E_{\rm O}$ to be positive and large; or else we might assume that we have deuterium occupation of monovacancy traps. For this latter case, we can write

$$E_{\rm T}[V] - E_{\rm O} = k_{\rm B}T\left\{\ln\left(\frac{\Theta_{\rm V}-\theta_{\rm T}}{\theta_{\rm T}}\frac{\theta_{\rm O}}{1-\theta_{\rm O}}\right) + \ln\frac{z_{\rm T}[V]}{z_{\rm O}}\right\}, \tag{41}$$

where $\Theta_{\rm V}$ is the (unknown) fraction of monovacancy sites available.

Results are given in Table 3. One sees low but plausible O-site to T-site excitation energies under the assumption that the T-site occupation is conventional, with an O-site to T-site excitation energy that increases with loading.

The negative O-site to T-site excitation energies estimated in a simple model assuming the number of tetrahedral vacancy sites is $\Theta_{\rm V} = 0.04$ corresponds to a binding energy near 100 meV, which is a bit less than the vacancy binding energies computed by Vekilova et al. [81]. We do not know the number of vacancies present in these experiments; however, it is clear that in each case we would be able to obtain plausible (but high) solutions for vacancy concentrations consistent with the observed tetrahedral occupancy.

3.6. O-site and T-site occupation for different excitation energies

It seems to be useful to examine model predictions for the O-site and T-site occupation as a function of the total loading for different assumed O-site to T-site excitation energies. We expect the O-site to T-site excitation energy to depend

Table 2. Lower bound on excitation energy from neutron diffraction experiment at $\theta = 0.96$ at 25°C, assuming different values for T-site occupation.

θ	$\theta_{\rm O}$	$\theta_{\rm T}$	$E_{\rm T} - E_{\rm O}$ (meV)
0.96	0.955	0.005	224.6
0.96	0.950	0.01	203.9
0.96	0.960	0.02	181.0

Table 3. O-site to T-site excitation energies estimated from the neutron diffraction data of Pitt and Gray [73]. The $E_T - E_O$ number are for conventional T-site occupation [Equation (40)]; and the $E_T[V] - E_O$ numbers are for T-sites in monovacancies Eq. (41). The number of vacancy sites for this model is assumed to be $\Theta_V = 0.04$.

θ_O	θ_T	$E_T - E_O$ (meV)	$E_T[V] - E_O$ (meV)
0.068	0.016	133	-115
0.118	0.018	158	-96
0.161	0.021	168	-93
0.231	0.022	188	-76
0.355	0.030	203	-96
0.384	0.033	204	-118

on the D/Pd loading ratio, but since at present no reliable information is available with which to model, it will be convenient instead to present curves at constant excitation energies. We make use of the local isotherm for O-site and T-site occupation at constant loading [55]

$$\left(\frac{1-\theta_O}{\theta_O}\right)\left(\frac{\theta_T}{2-\theta_T}\right) = \frac{z_T}{z_O}\exp\left\{-\frac{(E_T - E_O)}{k_B T}\right\}. \tag{42}$$

Results are shown in Fig. 5. From this one can get some intuition as to how abrupt the transition from O-site occupation to T-site occupation is. For example, if the excitation energy were 500 meV, there would be an abrupt change in the

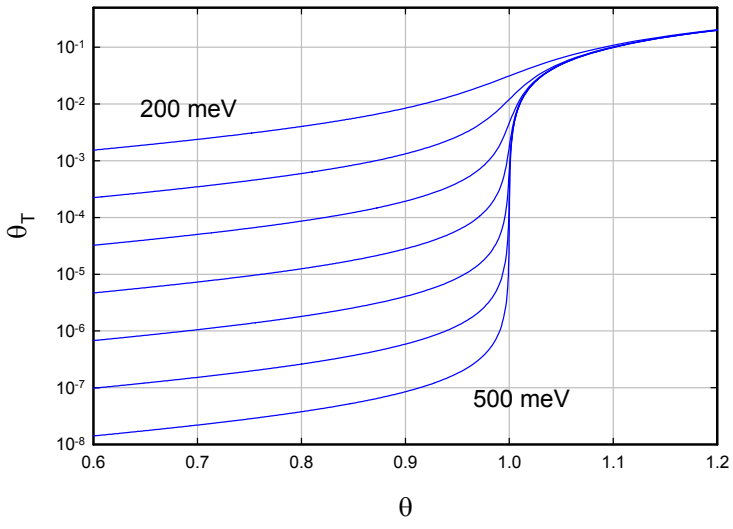

Figure 5. Tetrahedral fraction θ_T as a function total D/Pd loading θ for O-site to T-site energies of 200, 250, 300, . . ., 500 meV.

T-site occupation and a corresponding substantial change in the chemical potential which could in principle be detected in electrochemical measurements.

3.7. Discussion

It seems clear that we could learn much from neutron diffraction experiments carried out on PdD samples that are highly loaded. It is possible that the neutron diffraction experiments of Pitt and Gray [73] can be interpreted as demonstrating T-site occupation in the bulk, from which low O-site to T-site excitation energies can be inferred. It is also possible that the measurements were compromised due to the presence of a large number of monovacancies, since in a monovacancy both O-sites and T-sites can be occupied with a very small difference between the site energies. Later on we will make use of the results of these measurements interpreted as referring to bulk T-site occupation to develop an empirical fit for the excitation energy as a function of loading.

4. O-site to T-site Excitation Energy at High Loading

To complete our empirical model we require estimates for the O-site to T-site excitation energy. From the discussion of the last section, we know that the O-site to T-site excitation energy in PdD near unity loading must be greater than about 200 meV. Our goal in this section is to attempt to develop estimates for the excitation energy near unity for both PdD and PdH by comparing model predictions with experimental data at high pressure.

4.1. PdH at high loading

Let us return now to the high pressure PdH experiments of Tkacz and Baranowski [65], and compare results from the model with measured data points. By trying different values for the constant excitation energy, we find that the minimum error occurs for an excitation energy of 225.6 meV. The model parameters in this case are

$$\text{PdH}: \quad E_{\rm O}(\theta_0) + \frac{E_{\rm D}}{2} = -408.6 \text{ meV}, \quad E'_{\rm O}(\theta_0) = 322.5 \text{ meV}, \quad E''_{\rm O}(\theta_0) = -205.1 \text{ meV}. \tag{43}$$

The resulting fit is shown in Fig. 6.

4.2. Resistance ratio standard for PdH

A table that gives estimates for the H/Pd loading in PdH corresponding to different values of the resistance ratio R/R_0 appears in Crouch-Baker et al. [21]. In this table an H/Pd loading of 1.0 corresponds to a resistance ratio of 1.067. Baranowski et al. [42] show a resistance ratio corresponding to this value at a pressure of about 1.17 GPa. The pressure at an H/Pd loading of 1.0 in the model just above is 1.23 GPa, which is close.

If we carry out a least squares fitting of the pressure versus loading data set with fixed O-site to T-site excitation energy, including the two lowest points from Tkacz and Baranwoski along with the a loading of unity at 1.17GPa, then we end up with a low O-site to T-site excitation energy of about 202 meV.

4.3. Resistance ratio standard for PdD

One resistance ratio calibration curve currently in use for PdD (see [5]) gives a D/Pd loading of unity at a resistance ratio R/R_0 of 1.25, which corresponds to a D_2 equilibrium pressure of 1.94 GPa. A consistent model with constant O-site to T-site excitation energy is optimized with an excitation energy of 237 meV.

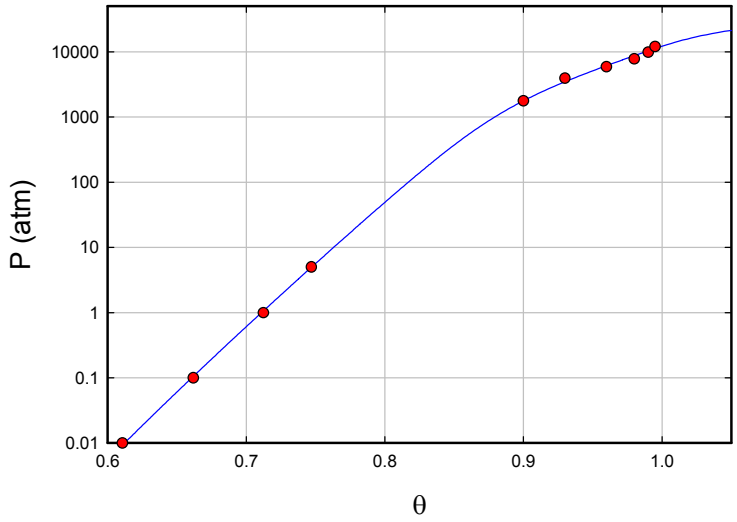

Figure 6. Least squares fit assuming an O-site to T-site excitation energy of 225.6 meV (independent of loading) to selected pressure as a function of loading points for PdH at 300 K as a function of loading; points used for the fit (red circles); least squares fit (blue line).

4.4. Resistance ratio versus fugacity for PdD at high loading

High pressure experiments with PdD were reported by Baranowski et al. [42] in which the applied D_2 reached as high as 3.1 GPa. Unfortunately the loading was not measured in these experiments, so we do not have a data set that we can compare directly with the model. However, it was noted in this paper that a noticeable break in the resistance ratio occurred at $\log_{10} f$ was about 9.3 (with fugacity assumed to be in atmospheres), which corresponds to a pressure of about 2 GPa.

We have used the model to compute θ as a function of the fugacity in order to see what O-site to T-site excitation energy might be relevant. Model results in the case of constant O-site to T-site excitation energy are shown in Fig. 7. We see that we can arrange for an intercept near $\log_{10} f = 9.3$ for an excitation energy of about 225 meV.

It may be that the determination of the resistance ratio curve involved an interpretation of the change of slope of the resistance ratio curve versus $\log_{10} f$ as defining where a D/Pd loading of unity occurs. In principle the argument here is basically the same, except that the model under discussion results in a shift in pressure. If we assume that the change in slope of the deuterium occupation fraction as a function of $\log_{10} f$ is correlated to the change in the slope of the resistance ratio as a function of $\log_{10} f$, then we conclude that $\theta = 1$ occurs closer to a pressure of 1.87 GPa at a resistance ratio R/R_0 near 1.28.

4.5. Zero-point energy considerations

We often think of PdH and PdD as being very similar other than due to differences attributable to the zero-point energy. Consequently, we might expect the O-site to T-site excitation energy in PdH to be larger than the excitation energy in PdD by the zero-point energy difference. For this discussion, we make use of the calculations of Ke and Kramer [63] for which the difference in zero-point energies for the O-site is

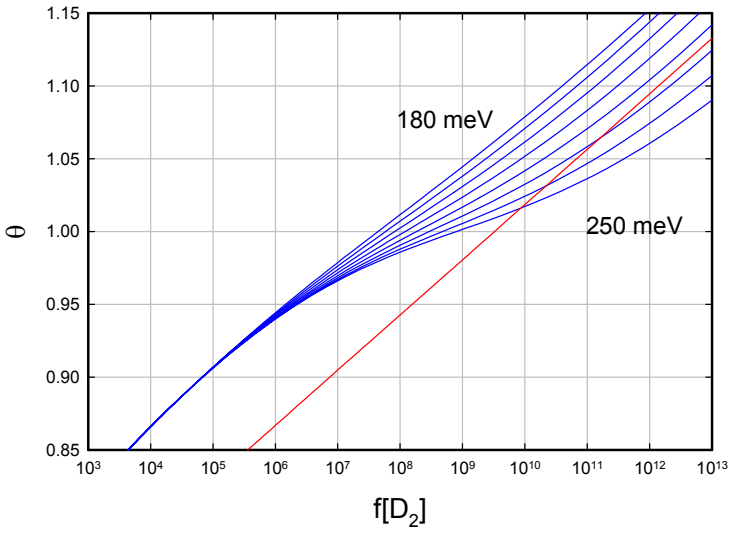

Figure 7. D/Pd ratio θ as a function of fugacity for simple models with constant O-site to T-site energies of 180, 190, . . ., 250 meV (blue lines); line with matched slope and intercept at $\log_{10} f = 9.3$(red).

$$\Delta E_{\rm O}(\text{H-D}) = 98.4 - 67.4 = 31.0 \text{ meV}. \tag{44}$$

The corresponding difference in the zero-point energies for the T-site is

$$\Delta E_{\rm T}(\text{H-D}) = 180.6 - 128.4 = 52.2 \text{ meV}. \tag{45}$$

From this we would conclude that the O-site to T-site excitation energy in PdH should be larger than in PdD by 21.2 meV near $\theta = 0$. We note that in the analysis of α-phase solubility data in [52] we obtained a smaller difference (about 1 meV). From the analysis in this section we would conclude that the O-site to T-site excitation energies are practically the same for PdH and PdD.

At high loading near $\theta = 1$ we might expect that the lattice expansion would result in a lower local zero-point energy. However, in this case the notion of a local zero-point energy is problematic as we would expect fully developed phonon dispersion relations; in this case the zero-point energy would need to be computed by summing over all of the vibrational modes. The lattice expansion is greater for PdH than for PdD, so there is the possibility that the zero-point contribution is reduced for PdH relative to PdD.

4.6. X-ray and R/R_0 data of Knies et al.

Electrochemical experiments with PdD and PdH were reported by Knies et al. [29] in which high loadings were achieved, where the (bulk) resistance ratio was measured, and where the (surface) lattice constant was measured. In principle this kind of measurement would be extremely useful in sorting out solubility issues at very high loading, and

providing data with which to compare against modeling. Probably it is useful here to consider the experiment in light of the discussion above in this Section.

For the PdD B2 experiment, the resistance ratio of 1.61 was obtained, interpreted as a bulk loading of 0.95; and a surface lattice constant of 4.09 Å was measured, and interpreted as a surface loading of 0.977. If we take a resistance ratio as corresponding to an equilibrium pressure of about 0.81 GPa, then the model with constant excitation energy would give a bulk loading of 0.939, compatible with the interpretation of Knies et al.

To determine a D/Pd loading consistent with a lattice constant of 4.09 Å it would be useful to have appropriate calibration data available. For example, Schirber and Morosin [82] have reported a systematic set of measurements at 77 K, showing that the lattice constant is very nearly linear in the loading. No equivalent study has been reported near room temperature. If we developed similar linear calibrations based on Yamamoto et al. [26], or perhaps on Felici et al. [27], we would probably conclude that the surface loading was lower than 0.977. On the other hand, a systematic study in the case of PdH_x was reported by Balbaa et al. [83], and based on these measurements we would probably conclude that a lattice constant of 4.09 Å corresponds to a D/Pd loading near unity. One conclusion that we might draw from this is that it would be very useful if a systematic calibration of D/Pd loading versus lattice constant could be established at room temperature.

For PdH, a resistance ratio as low as 1.28 appears at the largest lattice constants. The associated equilibrium pressure from [42] looks to be about about 0.67 GPa. This corresponds to a loading in a model with constant excitation energy of about 0.959, which is compantible with the 0.97 interpreted reported by Knies et al. [29].

4.7. Discussion

In this section we have taken the O-site to T-site excitation energy to be constant with loading θ, which allows us to develop estimates independently for PdH and for PdD. From the high pressure loading data of Tkacz and Baranowski we infer an excitation energy of 225.6 meV; from the resistance ratio as a function of fugacity data of Ref. [42] we estimate an excitation energy of 225 meV. We might have expected the PdH excitation energy might be larger than the PdD excitation energy based on estimates for the zero-point energy. However, the analysis of this section leads to the conclusion that the two excitation energies are essentially the same, analogous to what was found in our analysis of the α-phase solubility; this is a result which in retrospect seems very plausible.

Altogether this leads to a matched set of models for PdH and PdD which we can summarize through the model parameters

$$\text{PdH}: \quad E_{\rm O}(\theta_0) + \frac{E_{\rm D}}{2} = -384.5 \text{ meV}, \quad E'_{\rm O}(\theta_0) = 289.3 \text{ meV},$$

$$E''_{\rm O}(\theta_0) = -139.6 \text{ meV}, \quad \Delta E = 225.6 \text{ meV}, \tag{46}$$

$$\text{PdD}: \quad E_{\rm O}(\theta_0) + \frac{E_{\rm D}}{2} = -373.3 \text{ meV}, \quad E'_{\rm O}(\theta_0) = 289.3 \text{ meV},$$

$$E''_{\rm O}(\theta_0) = -139.6 \text{ meV}, \quad \Delta E = 225 \text{ meV}. \tag{47}$$

Results for pressure as a function of loading θ are shown in Fig. 8. We note that the O-site energies from this model are significantly lower than the incremental enthalpy ΔH one can find in the literature, which is about 240 meV [84]. This can be understood from the differential relation between the chemical potential and the O-site and T-site energies; here

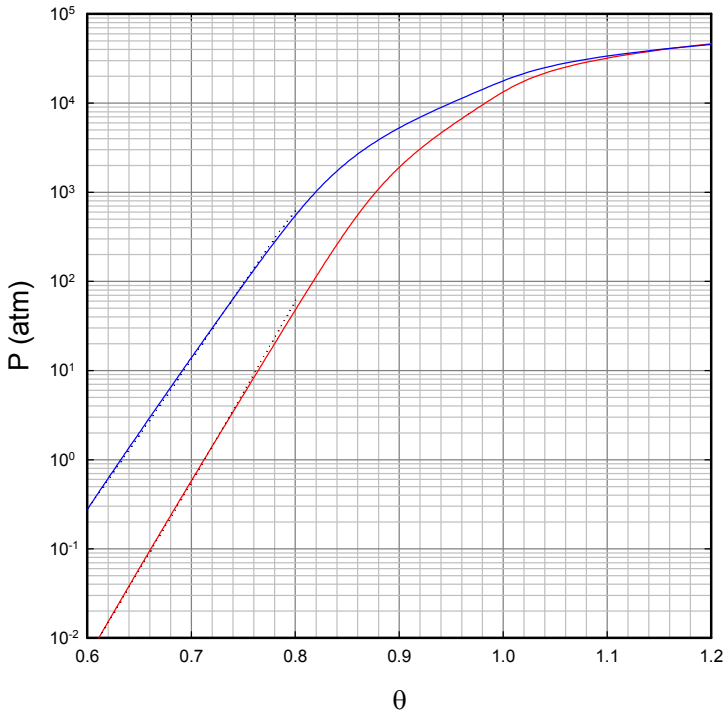

Figure 8. Model pressure as a function of loading θ at 300 K; PdH (red line); low pressure empirical model of Baranowski et al. [42] for PdH (dark red dotted line); PdD (blue line); low pressure empirical model of Baranowski et al. [42] for PdD (dark blue dotted line).

we have used a boundary condition at $\theta = 0.6$ instead of a boundary condition at $\theta = 0$. Hence the solutions for the O-site and T-site energies can be different (due to the different boundary conditions) for the same chemical potential.

In principle the established resistance ratio calibrations from the literature can be used to provide estimates for the O-site to T-site excitation energies assuming a constant excitation energy. The energies estimated in this way are 202 meV for PdH and 237 meV for PdD. Since we are expecting the excitation energies for the two cases to be close, this suggests that the different calibrations are not consistent. The resulting excitation energy estimates are nevertheless helpful in this case, as they are in the same range as estimates from other measurements.

5. O-site to T-site Excitation Energy as a Function of θ

We are interested in the specification of a model for the O-site to T-site excitation energy as a function of loading at 300 K. We have data from neutron diffraction experiments which are relevant, and which we will make use of. However, there also appears discussion in the literature on the possible impact of the T-site on diffusion which is also of interest.

5.1. Diffusion coefficient anomaly and the Sicking conjecture

We consider the diffusion coefficient anomaly, where the diffusion coefficient of D in PdD at low loading is greater than the diffusion coefficient of H in PdH at low loading. For example, consider the α-phase diffusion coefficient parameterizations given in Fukai's book [35]; if we evaluate them for PdH and PdD at $T = 300$ K, we obtain

$$D_{\rm H}(300\ {\rm K}) = 3.97 \times 10^{-7}\ {\rm cm}^2/{\rm s}, \tag{48}$$

$$D_{\rm D}(300\ {\rm K}) = 5.89 \times 10^{-7}\ {\rm cm}^2/{\rm s}. \tag{49}$$

The issue here is that the diffusion coefficient for deuterium is higher than the diffusion coefficient for hydrogen, where we might expect that the diffusion coefficient for hydrogen should be larger since hydrogen is lighter.

A resolution to this anomaly has been proposed by Sicking [85,86]. The basic idea is that the zero-point energy of the tetrahedral site is larger for PdH than for PdD, so that H might not be bound at the T-site, or perhaps the T-site is bound but leaks via tunneling. In either case, the contribution of O–T–O transitions to the diffusion coefficient might be reduced in PdH relative to PdD; this is a candidate explanation for the anomaly in the diffusion coefficient. Ke and Kramer [63] have modeled diffusion taking this into account, and find a larger diffusion coefficient for deuterium than for hydrogen (the model for deuterium in this case matches experiment, although the agreement with experiment is only qualitative in the case of hydrogen).

5.2. Implication for the O-site to T-site excitation energy

Our interest in this issue comes from the implication it has for the O-site to T-site excitation energy. For example, imagine the simplest scenario in which hydrogen in the T-site in α-phase PdH is not bound, and D in α-phase PdD is bound. The experimental activation energies are given by Sicking [86] to be 230 meV for α-phase PdH and 206 meV for α-phase PdD. Leisure et al. [87] give the barrier energies to be 232 meV for $PdH_{0.67}$ and 219 meV for $PdD_{0.67}$. The barrier energies in the two cases in the model of Ke and Kramer [63] are 204 meV for $PdH_{0.25}$ and 185 meV for $PdD_{0.25}$ (which result in theoretical activation energies close to experiment). In this scenario then we might conclude that the O-site to T-site excitation energy at low loading in PdH is above 204 meV, and the O-site to T-site excitation energy in PdD is below 185 meV.

Of course, such an argument is too simplistic, since we would want the deuterium atom to be bound and not leak in the T-site well for PdD, so we would prefer that its energy be well below 185 meV. This would suggest that we should be satisfied if the hydrogen in PdH leaks rapidly out of the T-site well in PdH. However, in either case we see that if we accept Sicking's conjecture, it implies various constraints on the O-site to T-site excitation energies.

5.3. Quasi-elastic neutron scattering and NMR experiments

We can make some progress on this by considering experimental results on quasi-elastic neutron scattering experiments, which can give information about the diffusion mechanism. For example, based on Sicking's conjecture, we might expect not to see evidence for O–T–O transitions in PdH if the T-site either is unbound or leaks; and we might expect to see evidence for O–T–O transitions in PdD if the T-site is bound and does not leak in PdD. In an early quasi-elastic neutron scattering experiment with β-phase PdH by Beg and Ross [88] the data was interpreted as being consistent with O–T–O diffusion processes, which would argue against the Sicking conjecture. However, a subsequent quasi-elastic neutron scattering experiment reported by Nelin and Sköld [89] gave a different result; in this case more accurate

measurements could be fit to models for O–O transitions, and not by O–T–O transitions. A similar conclusion was drawn based on NMR measurements [90–92].

The experimental results for PdH then are consistent with the Sicking conjecture. What we need next are analogous measurements for the O–T–O and O–O jump mechanisms in PdD. One would imagine that it should be possible to confirm the conjecture from a quasi-elastic neutron scattering or from NMR measurements, which are sensitive to the O–T–O diffusion mechanism. Unfortunately, we have as yet not been able to find reports of such measurements; consequently we do not know from experiment whether the T-site in PdD_x participates in deuterium diffusion.

5.4. Theoretical diffusion models based on the O–T–O mechanism

Quite a few theoretical treatments of the problem of diffusion have appeared in the literature. Computations of diffusion coefficients based on an O–T–O mechanism appear widely [39,67,68,70,94]. The situation in this case is perplexing. Quasi-elastic neutron scattering and NMR experiments appear to rule out the O–T–O mechanism in PdH, yet most modern treatments of the theoretical problem are based on the O–T–O mechanism.

One exception to this is an important recent paper by Yoshinari [95]. In this work a three-dimensional potential was developed from density functional calculations based on the VASP code, and numerical solutions for the eigenfunctions were obtained. Differences between diffusion in PdH and PdD in this calculation are attributed to the details of the excited state structure. The T-site ground state energy for H in Pd in this model is 240.9 meV, leading to an excitation energy of 156.2 meV.

5.5. O-site to T-site excitation energy for different θ

There does not seem to be an unambiguous conclusion from theoretical and experimental results on diffusion so far. The accuracy of the theoretical calculations is impressive, but not yet at the level we are interested in. The experimental results so far do not shed light on the excitation energy, except perhaps in providing an upper limit.

In the discussion above we were able to obtain estimates for the O-site to T-site excitation energy at different D/Pd loadings from the neutron diffraction experiments of Pitt and Gray [73]. Now that we have an estimate for the excitation energy at $\theta = 1$ from the high pressure experiments of Baranowski et al. [42], it seems reasonable to ask whether the different excitation energies might be consistent. The different results are shown together in Fig. 9, along with an empirical fit given by

$$\Delta E(\theta) = \frac{\alpha_0 + \alpha_1\theta}{1 + \beta_1\theta} \tag{50}$$

with

$$\alpha_0 = 100.676 \text{ meV}, \quad \alpha_1 = 824.259 \text{ meV},$$

$$\beta_1 = 3.1108. \tag{51}$$

Our conclusion from this discussion is that there appears to be consistency between the O-site to T-site excitation energies from the different sources. Although arising from completely different experiments, the excitation energies from the neutron diffraction data and from the high pressure data seem compatible. This would also be the case if the values from the neutron diffraction experiment were under-estimated by 10–20 meV due to interference from monovacancy occupation. The excitation energy from the analysis of the α-phase region was fine tuned to agree with

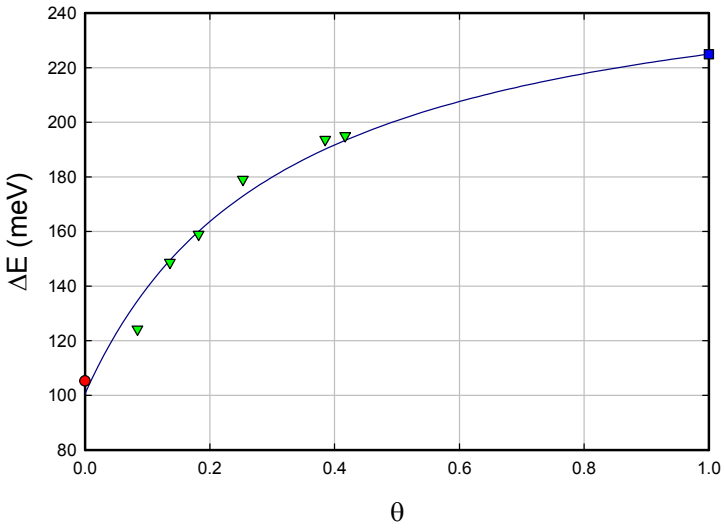

Figure 9. O-site to T-site excitation energy as a function of loading; inferred from data of Pitt and Gray [73] (green triangles); estimated from high pressure loading data of Baranowski et al. [42] (blue square); excitation energy from α-phase PdD_x analysis of Hagelstein (2015) (red circle); empirical fit (dark blue line).

the neutron diffraction data; however, had this not been done we would have ended up with an excitation energy not very different which would be compatible as an independent measurement.

In the case of PdH the excitation energy at $\theta = 0$ was estimated to be 106.5 meV at $\theta = 0$ [[52]], and 226 meV at $\theta = 1$. In both cases the excitation energy is larger by about 1 meV; so we have taken $\Delta E(\theta)$ to be larger by 1 meV in this case.

5.6. Site energy models with θ-dependent excitation energy

It is possible to optimize the O-site energy model for PdH as before, but now with the θ-dependent excitation energy model discussed above. A good fit is obtained with the parameters

$$\text{PdH}: \quad E_{\rm O}(\theta_0) + \frac{E_{\rm D}}{2} = -409.2 \text{ meV}, \quad E'_{\rm O}(\theta_0) = 328.6 \text{ meV},$$

$$E''_{\rm O}(\theta_0) = -215.5 \text{ meV}. \tag{52}$$

The corresponding fit for PdD is then

$$\text{PdD}: \quad E_{\rm O}(\theta_0) + \frac{E_{\rm D}}{2} = -399.1 \text{ meV}, \quad E'_{\rm O}(\theta_0) = 328.6 \text{ meV},$$

$$E''_{\rm O}(\theta_0) = -215.5 \text{ meV}. \tag{53}$$

These empirical fitting parameters are a bit different from those found above in the case where the excitation energy is taken to be constant with loading. The associated pressure versus loading curves are shown in Fig. 10. The O-site and T-site fractions θ_O and θ_T are shown in Fig. 11.

5.7. Discussion

Although the O-site to T-site excitation energy has been much studied over many years, there is little agreement in the literature how big the excitation energy should be. There is an anomaly in the diffusion coefficient in which the value for deuterium in palladium is larger than the value for hydrogen in palladium, which has provided the motivation for the conjecture of Sicking which would have important implications for the O-site to T-site excitation energy if true. Experimental results for quasi-elastic neutron scattering and NMR appear to rule out the O–T–O mechanism in PdH, consistent with the Sicking conjecture, but also consistent with an O-site to T-site excitation energy greater than the activation energy. Since at present we lack quasi-elastic neutron scattering results and NMR results clarifying the diffusion mechanism in PdD, there is no resolution of the problem from experiment. The recent theoretical models that focus on a mechanism presumably ruled out is perplexing.

Nevertheless, there appears to be consistency in the excitation energy developed from the analysis of neutron

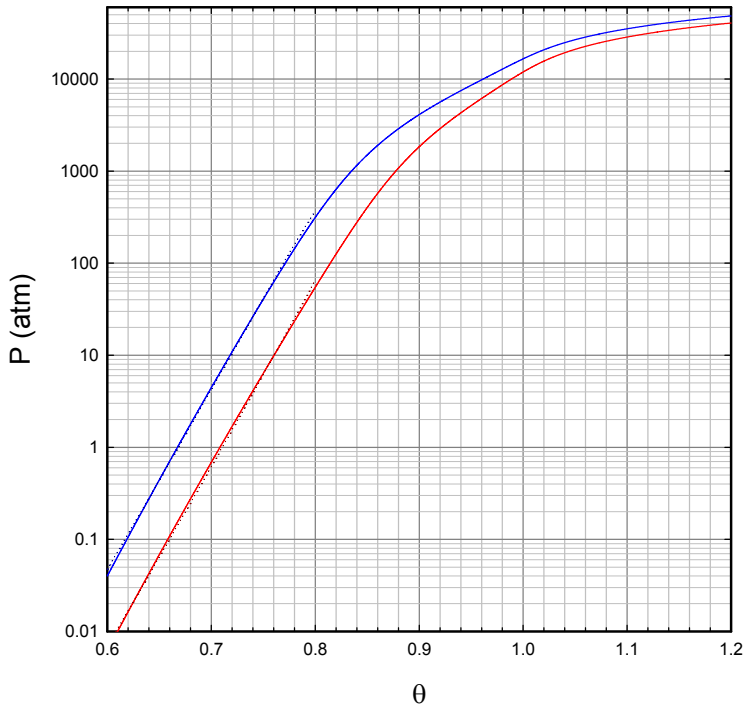

Figure 10. Model pressure as a function of loading θ at 300 K; PdH (red line); low pressure empirical model of Baranowski et al. [42] for PdH (dark red dotted line); PdD (blue line); low pressure empirical model of Baranowski et al. [42] for PdD (dark blue dotted line).

diffraction data, high pressure loading data, and from α-phase solubility data. We note that the neutron diffraction experiments are done at elevated temperature, and the high pressure measurements are done at room temperature. We took as an ansatz that the excitation energy did not vary with temperature in the analysis of the α-phase solubility data, and we were able to obtain good results. Implicit in the argument in this section is the assumption that the excitation energy is not a strong function of temperature for different loadings.

6. Possibility of new electrochemical measurements

In recent years researchers have learned how to achieve very high D/Pd loading near unity reproducibly, which constitutes an advance in electrochemistry, and potentially allows new experiments to be done which were not possible previously. We have wondered what experiments might be possible with this new capability, specifically in connection with the issues under discussion in the sections above. Here we speculate about the possibility of extending electrochemical measurements of the derivative of the chemical potential with loading, and of the Frumkin adsorption isotherm parameter, to higher loading than normally done in the hope of obtaining new information about the O-site to T-site excitation energy and solubility.

In Fig. 12 we show model results for the chemical potential as a function loading for both PdH and PdD. For many decades it has been taken as given that the hydrogen and deuterium chemical potential is linear in the loading above the miscibility gap. The chemical potential that results from the models under consideration in this paper are weakly nonlinear above the miscibility gap, and show a weak step near $\theta = 1$.

The corresponding slopes are plotted in Fig. 13. We see a weak nonlinearity in the slope above the miscibility gap from the models, and a peak near $\theta = 1$. This result is interesting, since the slope of the chemical potential is experimentally accessible. For example, we recall the measurement of the derivative of the enthalpy for PdD given in

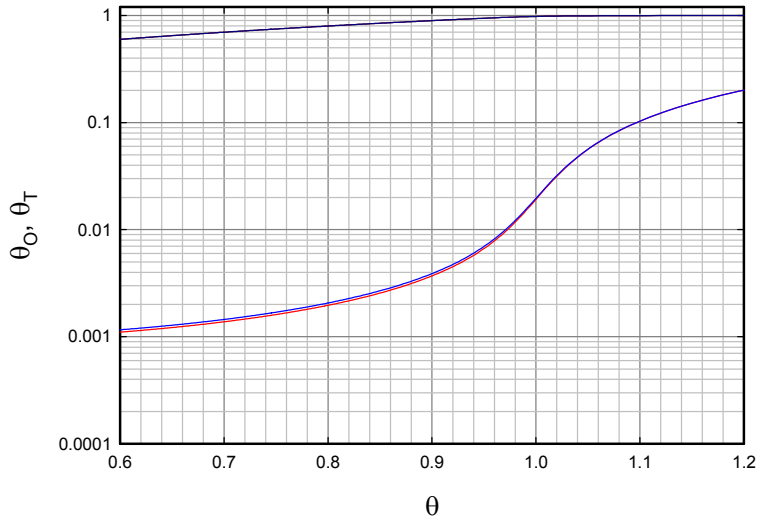

Figure 11. O-site fraction for PdH (upper dark red line, under upper dark blue line) as a function of θ; T-site fraction for PdH (lower red line); O-site fraction for PdD (upper dark blue line); T-site fraction for PdD (lower blue line).

Chun and Ra [97] which led to an estimate for the derivative of the chemical potential

$$\frac{d\mu_H}{d\theta} = 514 \text{ meV}. \tag{54}$$

The lowest value for $d\mu_D/d\theta$ in the β phase in the PdD model is 576 meV. The Frumkin adsorption isotherm parameter u is related to this derivative according to

$$u = \frac{1}{k_B T}\frac{d\mu_H}{d\theta} = 22.3. \tag{55}$$

The slope measured in [97] corresponds to $u = 19.9$.

Of interest in this discussion is that we have the possibility of learning something about the O-site to T-site excitation energy from electrochemical measurements of the slope of the chemical potential. The presence of a maximum in the slope close to $\theta = 1$ potentially gives us a way to determine where $\theta = 1$ is experimentally, and the value of the slope at the maximum places a strong constraint on the O-site to T-site excitation energy.

7. Summary and Conclusions

We have studied new empirical models for PdH and PdD for the O-site energy, and for the O-site to T-site excitation energy, in order to compare against a variety of experimental data. It must be emphasized that at this point we have no unambiguous experimental clarification that tetrahedral sites are occupied at high loading. Strictly speaking our model applies to loading to arbitrary excited state sites as long as there are two per Pd atom (and we would obtain very similar results if there were a different number of such excited state sites per Pd atom).

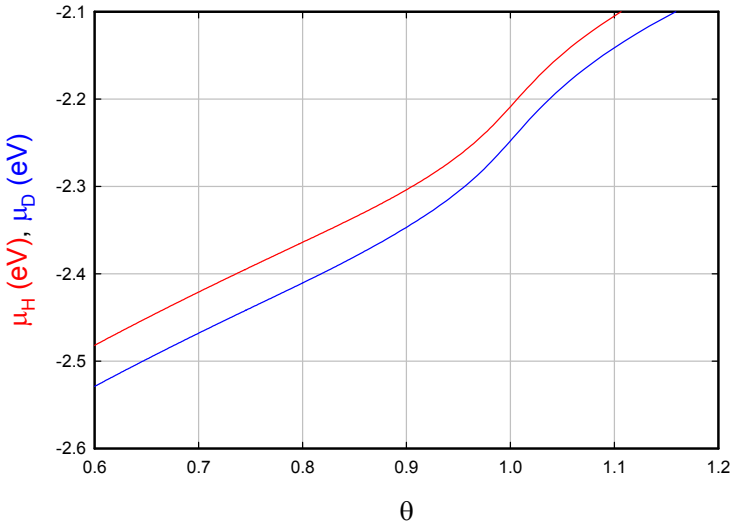

Figure 12. Model chemical potentials for PdH and PdD as a function of loading θ at 300 K with θ-dependent excitation energy.

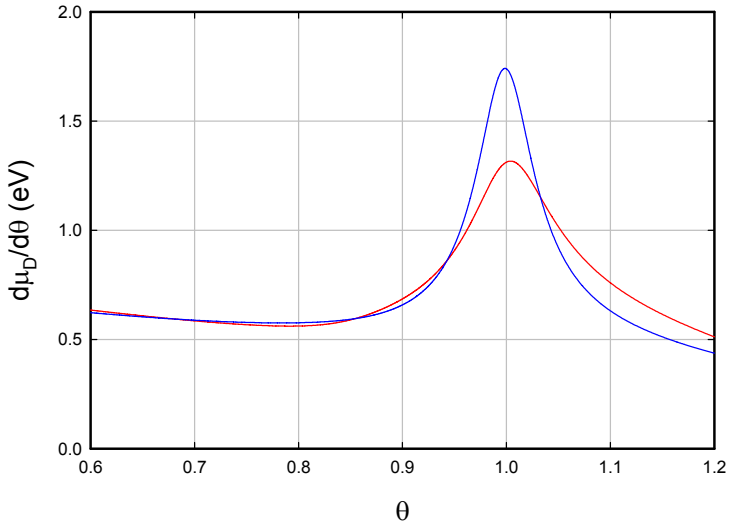

Figure 13. Slope of the model chemical potentials of Fig. 12 as a function of loading θ at 300 K.

A key issue in the construction of any empirical model is to have sufficient degrees of freedom to capture the essential features of the data of interest, and then to find sufficient experimental data so that constraints can be found for all of the different degrees of freedom. Here we were able to work with an O-site energy model taken to be quadratic in the total loading θ, and an O-site to T-site excitation energy taken to be constant or fit to available data. We introduced supplementary constraints which presume that PdH and PdD differ primarily through constant offset energies, which reduced the number of free parameters. The issue is that we have good solubility data at relatively high loading for PdH, but not for PdD. By taking the approach that we have, we are able to make use of the data for the hydride and use it to inform our model for the deuteride.

There are a number of implications of the results we obtained. For an H/Pd loading of 1 the model equilibrium pressure is 1.21 GPa, and based on the high pressure experiments of Baranowski et al. [42] this corresponds to a resistance ratio of 1.055. The corresponding value given in Crouch-Baker et al. [21] is 1.067, which is a bit higher. For a D/Pd loading of 1 the model equilibrium pressure is 1.68 GPa, which corresponds to a resistance ratio of about 1.30, which is higher than the 1.24 value corresponding to the calibration of McKubre et al. [5]. In this case the current PdH calibration slightly overestimates the loading, and the PdD calibration underestimates the loading, leading to the conclusion that the two systems are more alike than would be concluded from the standard resistance calibrations.

It is clear from this study that more experimental measurements are needed to clarify what happens at high loading, and to be sure of the assumptions and interpretations of the model. As mentioned above, it has not been unambiguously settled by experiment where hydrogen or deuterium goes once the octahedral sites are filled. If the slope of the chemical potential could be determined as a function of loading in new electrochemical experiments at very high loading, this would provide data which could be used to check for consistency with the new model, and which would provide us with an independent check on the O-site to T-site excitation energy. Additional quasi-elastic neutron diffraction experiments with PdD_x have the potential to provide direct measurements of T-site occupation, which could settle the issue. Quasi-elastic neutron scattering or NMR experiments on PdD have the potential to determine whether diffusion

in PdD occurs via an O–T–O mechanism, in contrast to PdH where the O–T–O mechanism appears to have been ruled out. Although not discussed in the text, solid state NMR experiments on PdH and PdD samples loaded above unity may help determine the site occupation of interstitials not in O-sites.

This kind of model is very powerful and can be very helpful in understanding experimental observations. We were able to develop reasonably precise estimates for the model parameters based on our interpretation of different experimental data. The value for the O-site to T-site excitation energy in PdD depends on our interpretation of resistance ratio data as a function of $\log_{10}$ fugacity in the experiments of Baranowski et al. [42]. It would be important to confirm (or else disprove) this interpretation in order to understand the resulting model better. It would also be useful to develop an equivalent plot for PdH for a similar assessment. We have relied heavily on the PdH loading measurements of Tkacz and Baranowski [65]; it would be useful to develop an equivalent data set for PdD.

Our focus has been on a model specific to 300 K. We have recently generalized our analysis to a set of isotherms at different temperatures that make up the phase diagram, with results that are compatible with the results presented in this work.

References

[1] M. Fleischmann, S. Pons and M. Hawkins, Electrochemically induced nuclear fusion of deuterium, *J. Electroanal Chem.* **201** (1989) 301; errata, **263** (1990) 187.

[2] M. Fleischmann, S. Pons, M.W. Anderson, L.J. Li and M. Hawkins, Calorimetry of the palladium–deuterium–heavy water system, *J. Electroanal. Chem.* **287** (1990) 293.

[3] P.L. Hagelstein, Bird's eye view of phonon models for excess heat in the Fleischmann–Pons experiment, *J. Cond. Mat. Nucl. Sci.* **6** 169 (2012).

[4] P.L. Hagelstein and I.U. Chaudhary, Phonon models for anomalies in condensed matter nuclear science, *Current Sci.* **108** 507 (2015).

[5] M.C.H. McKubre and F.L. Tanzella, Using resistivity to measure H/Pd and D/Pd loading: Method and significance, *Proc. ICCF12*, Yokohama, A Takahashi, K.-I. Ota and Y Iwamura (Eds.), World Scientific, Singapore, 2005, p. 392.

[6] M.C.H. McKubre, F.L. Tanzella and V. Violante, What is needed in LENR/FPE studies?, *J. Cond. Mat. Nucl. Sci.* **8** (2012) 187.

[7] M.C.H. McKubre, J. Bao, S. Crouch-Baker, P. Jayaweera, A. Sanjurjo and F. Tanzella, The palladium hydrogen system; Corrosion monitoring and energy production, it ECS Trans. **50** (2013) 357–365.

[8] M.C.H. McKubre, S. Crouch-Baker, A.M. Riley and S.I. Smedley, Excess power observations in electrochemical studies of the D/Pd system; the influence of loading, *Proc. ICCF3*, Nagoya, 1992, Nagoya, H. Ikegami (Ed.), Universal Academy Press, Tokyo, 1993, p. 5.

[9] M.C.H. McKubre, S. Crouch-Baker, R.C. Rocha-Filho, S.I. Smedley, F.L. Tanzella, T.O. Passell and J. Santucci, Isothermal flow calorimetric investigations of the D/Pd and H/Pd systems, *J. Electroanal. Chem.* **368** (1994) 55.

[10] M.C.H. McKubre, S. Crouch-Baker, A.K. Hauser, S.I. Smedley, F.L. Tanzella, M.S. Williams and S.S. Wing, Concerning reproducibility of excess power production, *Proc. 5th Int. Conf. on Cold Fusion*, 1995, pp. 17–33.

[11] T.A. Green and T.I. Quickenden, Electrolytic preparation of highly loaded deuterides of palladium, *J. Electroanaly. Chem.* **368** 121–131 (1994).

[12] M.C.H. McKubre, S. Crouch-Baker, F.L. Tanzella, S.I. Smedley, M. Williams, S. Wing, M. Maly-Schreiber, R.C. Rocha-Filho, P.C. Searson, J.G. Pronko and D.A. Kohler, Development of advanced concepts for nuclear processes in deuterated metals, Electric Power Research Institute Report TR-104195, 1994.

[13] F.L. Tanzella, S. Crouch-Baker, A. McKeown, M.C.H. McKubre, M. Williams and S. Wing, Parameters affecting the loading of hydrogen isotopes into palladium cathodes, *Proc. Sixth Int. Conf. on Cold Fusion, Progress in New Hydrogen Energy*, 1996, p. 171.

[14] T. Senjuh, H. Kamimura, T. Uehara, M. Sumi, S. Miyasita, T. Sigemitsu and N. Asami, Experimental study of electrochemical deuterium loading of Pd cathodes in the LiOD/D_2O system, *J. Alloys and Compounds* **253** (1997) 617–620.

[15] N. Asami, T. Senjuh, T. Uehara, M. Sumi, H. Kamimura and S. Miyashita, Material behavior of highly deuterated palladium, *Proc. 7th Int. Conf. on Cold Fusion*, 1998, pp. 15–21.

[16] I. Dardik, T. Zilov, H. Branover, A. El-Boher, E. Greenspan, B. Khachaturov, V. Krakov, S. Lesin, A. Shapiro and M. Tsirlin, Ultrasonically-excited electrolysis experiments at Energetics Technologies, *Proc. 14th Int. Conf. on Cold Fusion*, 2008, pp. 106–122.

[17] M. Apicella, E. Castagna, L. Capobianco, L. D'Aulerio, G. Mazzitelli, F. Sarto, A. Rosada, E. Santoro and V. Violante, Some recent results and ENEA, *Proc. 12th Int. Conf. on Cold Fusion*, 2012, pp. 117–132.

[18] V. Violante, E. Castagna, S. Lecci, F. Sarto, M. Sansovini, A. Torre, A. La Gatta, R. Duncan, G. Hubler, A. El-Boher, O. Azizi, D. Pease, D. Knies and M. McKubre, Review of materials science for studying the Fleischmann and Pons effect, *Current Sci.* **108** (2015) 540.

[19] O. Azizi, A. El-Boher, J.H. He, G.K. Hubler, D. Pease, W. Isaacson,V. Violante and S. Gangopadhyay, Progress towards understanding anomalous heat effect in metal deuterides, *Current Sci.* **108** (2015) 565.

[20] Y. Sakamoto, K. Takai, I. Takashima and M. Imada, Electrical resistance measurements as a function of composition of palladium–hydrogen (deuterium) systems by a gas phase method, *J. Phys.: Condensed Matter* **8** (1996) 3399.

[21] S. Crouch-Baker, M.C.H. McKubre and F.L. Tanzella, Variation of resistance with composition in the β-phase of the H–Pd system at 298 K, *Zeitschrift für Physikalische Chemie* **204** (1998) 247–254.

[22] P. Tripodi, M.C.H. McKubre, F.L. Tanzella, P.A. Honnor, D. Di Gioacchino, F. Celani and V. Violante, Temperature coefficient of resistivity at compositions approaching PdH, *Phys. Lett. A* **276** (2000) 122–126.

[23] P. Tripodi, D. Di Gioacchino and J.D. Vinko, AC electrical resistance measurements of PdH_x samples versus composition x, *J. Alloys and Compounds* **486** (2009) 55–59.

[24] P. Tripodi, A. Avveduto and J.D. Vinko, Strain and resistivity of PdH_x at hydrogen composition $x > 0.8$, *J. Alloys and Compounds* **500** (2010) 1–4.

[25] J. Gao, W.S. Zhang and J.J. Zhang, An explanation of hysteresis of electrical resistance—composition relationship in the Pd—H (D) and Pd alloy—H (D) systems measured by a gas phase method, *Int. J. Hydrogen Energy* **39** (2014) 21328–21334.

[26] T. Yamamoto, R. Taniguchi, T. Oka and K. Kawabata, In situ observation of deuteride formation inpalladium foil cathode by an X-ray diffraction method, *J. Less Common Metals* **172** (1991) 1381–1387.

[27] R. Felici, L. Bertalot, A. DeNinno, A. LaBarbera and V. Violante, In situ measurement of the deuterium (hydrogen) charging of a palladium electrode during electrolysis by energy dispersive X-ray diffraction, *Rev. Sci. Instr.* **66** (1995) 3344–3348.

[28] E.F. Skelton, P.L. Hagans, S.B. Qadri, D.D. Dominguez, A.C. Ehrlich and J.Z. Hu, In situ monitoring of crystallographic changes in Pd induced by diffusion of D, *Phys. Rev. B* **58** (1998) 14775.

[29] D.L. Knies, V. Violante, K.S. Grabowski, J.Z. Hu, D.D. Dominguez, J.H. He, S.B. Qadri and G.K. Hubler, In-situ synchrotron energy-dispersive X-ray diffraction study of thin Pd foils with Pd: D and Pd: H concentrations up to 1:1, *J. Appl. Phys.* **112** (2012) 083510.

[30] D. Letts and P.L. Hagelstein, Modified Szpak protocol for excess heat, *J. Cond. Matter Nucl. Sci.* **8** (2011) 1–11.

[31] P.L. Hagelstein and I.U. Chaudhary, Arguments for dideuterium near monovacancies in PdD, *15th Int. Conf. on Condensed Matter Nuclear Science*, 2009, pp. 282–287.

[32] J.E. Worsham, M.K. Wilkinson and C.G. Shull, Neutron-diffraction observations on the palladium–hydrogen and palladium–deuterium systems, *J. Phys. and Chem. Solids* **3** (1957) 303–310.

[33] G. Nelin, A neutron diffraction study of palladium hydride, *Physica status solidi (b)* **45** (1971) 527–536.

[34] H.D. Carstanjen, J.Dünstl, G.Löbl and R. Sizmann, Lattice location and determination of thermal amplitudes of deuterium in a-$PdD_{0.007}$ by channeling, *Physica Status Solidi (a)* **45** (1978) 529–536.

[35] Y. Fukai, *The Metal–Hydrogen System*, Springer, New York, 1991.

[36] J.R. Lacher, A theoretical formula for the solubility of hydrogen in palladium, *Proc. Roy. Soc. London, Series A, Math. Phys. Sci.* **161** (1937) 525–545.

[37] J.J. Rush and J.M. Rowe, Comment on High temperature thermodynamics of palladium-–hydrogen. II. Temperature dependence of partial molar properties of dilute solutions of hydrogen in the range 500—700 K [J. Chem. Phys. **65** (1976) 3915], *J. Chemical Phys.* **68** (1978) 3954–3954.

[38] M.A. Khan, J.C. Parlebas and C. Demangeat, Electronic structure and ordering of hydrogen in fcc transition metals, *J. Less Common Metals* **77** (1981) P1–P8.

[39] M.J. Gillan, A simulation model for hydrogen in palladium. I. Single-particle dynamics, *J. Phys. C: Solid State Phys.* **19** (1986) 6169.

[40] O.B. Christensen, P.D. Ditlevsen, K.W. Jacobsen, P. Stoltze, O.H. Nielsen and J.K. No, H-H interactions in Pd, *Phys. Rev. B* **40** (1989) 1993.
[41] S.M. Myers, P.M. Richards, D.M. Follstaedt and J.E. Schirber, Superstoichiometry, accelerated diffusion, and nuclear reactions in deuterium-implanted palladium, *Phys. Rev. B* **43** (1991) 9503.
[42] B. Baranowski, S.M. Filipek, M. Szustakowski, J. Farny and W. Woryna, Search for "cold-fusion" in some Me–D systems at high pressures of gaseous deuterium, *J. Less Common Metals* **158** (1990) 347–357.
[43] H. Hemmes, E. Salomons, R. Griessen, P. Sänger and A. Driessen, Lattice–gas model for the formation of palladium–silver hydrides at pressures up to 100 GPa, *Phys. Rev. B* **39** (1989) 10606.
[44] H. Sugimoto and Y. Fukai, Solubility of hydrogen in metals under high hydrogen pressures: thermodynamical calculations, *Acta Metallurgica et Materialia* **40** (1992) 2327–2336.
[45] Y. Fukai, Site preference of interstitial hydrogen in metals, *J. Less Common Metals* **101** (1984) 1–16.
[46] P.M. Richards, Molecular-dynamics investigation of deuteron separation in $PdD_{1.1}$, *Phys. Rev. B* **40** (1989) 7966.
[47] J.W. Halley and J.L. Valles, Estimate of nuclear fusion rates arising from a molecular-dynamics model of PdD_x, *Phys. Rev. B* **41** (1990) 6072.
[48] R. A. Oriani, The physical and metallurgical aspects of hydrogen in metals, *Fusion Technology* **26** 235–266 (1994).
[49] G. Benedek and P.F. Bortignon, Cold nuclear fusion: Viewpoints of solid-state physics, *Il Nuovo Cimento D* **11** (1989) 1227–1235.
[50] I.F. Silvera and F. Moshary, Deuterated palladium at temperatures from 4.3 to 400 K and pressures to 105 kbar: search for cold fusion, *Phys. Rev. B* **42** (1990) 9143.
[51] Y. Fukai and N. Okuma, Formation of superabundant vacancies in Pd hydride under high hydrogen pressures, *Phys. Rev. Lett.* **73** (1994) 1640.
[52] P.L. Hagelstein, O-site and T-site occupation of α-phase PdH_x and PdD_x, *J. Condensed Matter Nucl. Sci.* (in press).
[53] D.K. Ross, V.E. Antonov, E.L. Bokhenkov, A.I. Kolesnikov, E.G. Ponyatovsky and J. Tomkinson, Strong anisotropy in the inelastic neutron scattering from PdH at high energy transfer, *Phys. Rev. B* **58** (1998) 2591.
[54] P.L. Hagelstein Deuterium evolution reaction model and the Fleischmann–Pons experiment, *J. Condensed Matter Nucl. Sci.* **16** (2015) 46–63.
[55] P.O. Orondo, A theoretical model of interstitial hydrogen: pressure–composition–temperature, chemical potential, enthalpy and entropy, MIT Ph.D. Thesis, 2012.
[56] E. Salomons, On the lattice gas description of hydrogen in palladium: a molecular dynamics study, *J. Phys.: Condensed Matter* **2**(1990) 845.
[57] P. Orondo and P.L. Hagelstein, Basic physics model for PdH thermodynamics, *J. Condensed Matter Nucl. Sci.* **13** (2014) 149-–164.
[58] M. Ruda, E.A. Crespo and S.R. de Debiaggi, Atomistic modeling of H absorption in Pd nanoparticles, *J. Alloys and Compounds* **495** (2010) 471–475.
[59] H.C. Urey and D. Rittenberg, Some thermodynamic properties of the H1H2, H2H2 molecules and compounds containing the H2 atom, *J. Chemical Phys.* **1** (1933) 137–143.

[60] J.-M. Joubert, A calphad-type equation of state for hydrogen gas and its application to the assessment of Rh—H system, *Int. J. Hydrogen Energy* **35** (2010) 2104.
[61] J.-M. Joubert and S. Thiebaut, A thermodynamic description of the system Pd–Rh–H–D–T, *Acta Materialia* **59** (2011) 1680.
[62] P.L. Hagelstein, Equation of state and fugacity models for H_2 and for D_2, *J. Condensed Matter Nucl. Sci.* **16** (2015) 23–45.
[63] X. Ke and G.J. Kramer, Absorption and diffusion of hydrogen in palladium–silver alloys by density functional theory, *Phys. Rev. B* **66** (2002) 184304.
[64] T.B. Flanagan and W.A. Oates, The palladium–hydrogen system, *Ann. Rev. Mat. Sci.* **21** (1991) 269–304.
[65] M. Tkacz and B. Baranowski, Solubility of hydrogen in palladium hydride at high-pressure of gaseous hydrogen, *Roczniki Chemii* **50** (1976) 2159–2166.
[66] C. Elsässer, K.M. Ho, C.T. Chan and M. Fähnle, Vibrational states for hydrogen in palladium, *Phys. Rev. B* **44** (1991) 10377.
[67] P. Kamakoti and D.S. Sholl, A comparison of hydrogen diffusivities in Pd and CuPd alloys using density functional theory, *J. Membrane Sci.* **225** (2003) 145–154.
[68] S.Z. Baykara, Theoretical evaluation of diffusivity of hydrogen in palladium and rhodium, *Int. J. Hydrogen Energy* **29** (2004) 1631–1636.
[69] N. Ozawa, T.A. Roman, H. Nakanishi, H., Kasai, N.B. Arboleda Jr. and W.A. Dino, Potential energy of hydrogen atom motion on Pd (111) surface and in subsurface: A first principles calculation, *J. Appl. Phys.* **101** (2007) 123530.
[70] H. Grönbeck and V.P. Zhdanov, Effect of lattice strain on hydrogen diffusion in Pd: A density functional theory study, *Phys. Rev. B* **84** (2011) 052301.
[71] T.P. Senftle, M.J. Janik and A.C. van Duin, A reaxff investigation of hydride formation in palladium nanoclusters via monte carlo and molecular dynamics simulations, *J. Physical Chem. C* **118** (2014) 4967–4981.
[72] F.J. Rotella, J.W. Richardson Jr, L. Redey, G.P. Felcher, R.L. Hitterman and R. Kleb, Palladium deuteride formation in the cathode of an electrochemical cell, National Laboratory for High Energy Physics, KEK Report JP9206334, 1992, pp. 1–13.
[73] M.P. Pitt and E.M. Gray, Tetrahedral occupancy in the Pd–D system observed by in situ neutron powder diffraction, *EuroPhys. Lett.* **64** (2003) 344.
[74] K.G. McLennan, E.M. Gray and J.F. Dobson, Deuterium occupation of tetrahedral sites in palladium, *Phys. Rev. B* **78** (2008) 014104.
[75] M. Widenmeyer, R. Niewa, T.C. Hansen and H. Kohlmann, In situ neutron diffraction as a probe on formation and decomposition of nitrides and hydrides: A case study, *Zeitschrift für anorganische und allgemeine Chemie* **639** (2013) 285–295.
[76] J.P. Bugeat and E. Ligeon, Lattice location and trapping of hydrogen implanted in FCC metals, *Phys. Lett. A* **71** (1979) 93–96.
[77] J. Mory and E. Ligeon, Studies on dechannelling by defects and on lattice site location of hydrogen in face-centred cubic metals, *J. Materials Sci.* **17** (1982) 925–935.
[78] F. Besenbacher, B.B. Nielsen, J.K. Norskov, S.M. Myers and P. Nordlander, Interaction of hydrogen isotopes with metals: Deuterium trapped at lattice defects in palladium, *J. Fusion Energy* **9** (1990) 257–261.
[79] R.B. McLellan, The kinetic and thermodynamic effects of vacancy-interstitial interactions in Pd–H solutions, *Acta Materialia* **45** (1997) 1995–2000.
[80] F. Besenbacher, J.K. Nørskov, M.J. Puska and S. Holloway, Excitation of hydrogen motion inside a nickel vacancy, *Phys. Rev. Lett.* **55** (1985) 852.
[81] O.Y. Vekilova, D.I. Bazhanov, S.I. Simak and I.A. Abrikosov, First-principles study of vacancy-hydrogen interaction in Pd, *Phys. Rev. B* **80** (2009) 024101.
[82] J.E. Schirber and B. Morosin, Lattice constants of β–PdH_x and β-PdD_x with x near 1.0, *Phys. Rev. B* **12** (1975)117.
[83] I.S. Balbaa, P.A. Hardy, A. San-Martin, P.G. Coulter and F.D. Manchester, The effect of lattice distortions on the X-ray measurement of lattice parameters for PdH_x. I. Empirical relationships, *J. Phys. F: Metal Phys.* **17** (1987) 2041.
[84] E. Wicke and G.H. Nernst, Zustandsdiagramm und thermodynamisches Verhalten der Systeme Pd/H_2 und Pd/D_2 bei normalen Temperaturen; H/D-Trenneffekte, *Berichte der Bunsengesellschaft für physikalische Chemie* **68** (1964) 224–235.
[85] G. Sicking, Equilibrium and kinetic isotope effects, *Berichte der Bunsengesellschaft für physikalische Chemie* **76** (1972) 790–797.
[86] G. Sicking, Isotope effects in metal–hydrogen systems, *J. Less Common Metals* **101** (1984) 169–190.
[87] R.G. Leisure, L.A. Nygren and D.K. Hsu, Ultrasonic relaxation rates in palladium hydride and palladium deuteride, *Phys. Rev. B* **33** (1986) 8325.

[88] M.M. Beg and D.K. Ross, The quasielastic scattering of cold neutrons from the beta phase of palladium hydride (and hydrogen diffusion), *J. Phys. C: Solid State Phys.* **3** (1970) 2487.
[89] G. Nelin and K. Sköld, Diffusion of hydrogen in the ß-phase of Pd–H studied by small energy transfer neutron scattering, *J. Phys. and Chem. of Solids* **36** (1975) 1175–1182.
[90] D.A. Cornell and E.F.W. Seymour, Nuclear magnetic resonance study of hydrogen diffusion in palladium and palladium–cerium alloys, *J. Less Common Metals* **39** (1975) 43–54.
[91] E.F.W. Seymour, R.M. Cotts and W.D. Williams, NMR measurement of hydrogen diffusion in β–palladium hydride, *Phys. Rev. Lett.* **35** (1975) 165.
[92] P.P. Davis, E.F. W. Seymour, D. Zamir, W.D. Williams and R.M. Cotts, Nuclear magnetic resonance study of hydrogen diffusion in palladium–silver alloys, *J. Less Common Metals* **49** (1976) 159–168.
[93] P. Kamakoti and D.S. Sholl, Ab initio lattice–gas modeling of interstitial hydrogen diffusion in CuPd alloys, *Phys. Rev. B* **71** (2005) 014301.
[94] Y.M. Koroteev, O.V. Gimranova and I.P. Chernov, Hydrogen migration in palladium: First-principles calculations, *Phys. Solid State* **53** (2011) 896–900.
[95] O. Yoshinari, Origin of 'Inverse Isotope Effect' of hydrogen diffusion in palladium, In *Defect and Diffusion Forum* **312** (2011) 295–300.
[96] R. Nazarov, T. Hickel and J. Neugebauer, Ab initio study of H-vacancy interactions in fcc metals: Implications for the formation of superabundant vacancies, *Phys. Rev. B* **89** (2014) 144108.
[97] J.H. Chun and K.H. Ra, The phase-shift method for the frumkin adsorption isotherms at the Pd/H_2SO_4 and KOH solution interfaces, *J. Electrochemical Soc.* **145** (1998) 3794–3798.

J. Condensed Matter Nucl. Sci. 17 (2015) 67–90

Research Article

O-site and T-site Occupation of α-phase PdH_x and PdD_x

Peter L. Hagelstein*

Massachusetts Institute of Technology, Cambridge, MA 02139, USA

Abstract

An important study of the solubility of hydrogen in α-phase PdH_x and deuterium in α-phase PdD_x over a wide temperature range was published by Clewley et al. (*J. Chem. Soc., Faraday Trans. 1: Phy. Chem. Condensed Phases* **69** (1973) 449–458). An analysis of the data based on an empirical solubility model based on O-site occupation allows for an understanding of the data at low temperature, but probably is not a good starting place for understanding the solubility at high temperature. We have applied a recently developed empirical model for both O-site and T-site occupation to this data set, and find good agreement between data and a basic version of the model which assumes that the O-site and T-site partition functions are taken to be harmonic oscillator partition functions. Even better agreement is obtained when a more realistic O-site partition function is used. A range of optimum models with different assumptions about the T-site partition function is considered, and it is found to be possible to select one that matches the T-site occupation at zero loading inferred from neutron diffraction measurements of Pitt and Gray (*Europhys. Let.* **64** (2003) 344). The O-site to T-site excitation energy is assumed independent of temperature in these models, and we obtain specific model values of 105.3 meV for α-phase PdD_x and 106.5 meV for α-phase PdH_x.
 ISSN 2227-3123

Keywords: Empirical model, Mean-field lattice gas model, Solubility, α-phase PdH_x and PdD_x, Tetrahedral occupation

1. Introduction

Even though palladium hydride has been studied for almost a century and a half [1–12], there remains much that we do not know about some very basic issues. For example, interstitial hydrogen is known to occupy octahedral sites in bulk FCC palladium hydride, but it has not been established experimentally where additional hydrogen might go under high loading conditions where all of the O-sites are occupied (see Ref. [13] and references therein). Recent calculations of the O-site to T-site excitation energy indicate that the energy might be sufficiently low [14–20] that one could reasonably expect that there would be a small but observable T-site occupation at elevated temperature. In this work we propose to study this issue by comparing an appropriate model for O-site and T-site occupation with an old but important experimental data set for α-phase PdH_x and PdD_x [21]. We are able to extract plausible values for the O-site to T-site excitation energy from this comparison, which are generally consistent with the recent calculations.

*E-mail: plh@mit.edu

 ISSN 2227-3123

The experimental data consists of low pressure solubility data for α-phase PdH_x and PdD_x, where the interstitial hydrogen and deuterium concentration is low. Early theoretical models relevant to this regime were studied by Fowler [22] and Lacher [23]. Subsequent modeling of solubility at both low and high pressure has been reported by many authors [24–33]. Hydrogen and deuterium solubility has been studied in many experimental works [34–52]. To our knowledge there has not been an earlier study of α-phase PdH_x or PdD_x in which T-site occupation was modeled and a comparison with experimental data reported.

To carry out such an analysis, we can make use of a model for interstitial O-site and T-site occupation that was recently used to model PdD and PdH at high loading [13]. In a sense this kind of model is at the same time very simple and very powerful; following the early work of Fowler [22] and of Lacher [23] we assume equilibrium between H_2 (or D_2) in the gas phase and interstitial H (or D) which can occupy O-sites, and now also T-sites. An equilibrium statistical mechanics model requires a knowledge of the energy levels in the gas and the solid, and also a knowledge of the various partition functions associated with both phases. Over the years most of the relevant pieces of the model that we need have been studied, so that for us the largest uncertainty is in the O-site to T-site excitation energy and T-site partition functions It is possible to develop an estimate for the excitation energy and assess model partition functions by optimizing the empirical model to the experimental data set.

While simple in concept, it has become clear through working with the model and data that there are many issues. If we compare the most basic version of the model based on 3D simple harmonic partition functions, then we obtain rather good fits of the experimental data, and we obtain estimates for the excitation energy in line with recent calculations. If we work with more sophisticated partition function models, then we can get a range of excitation energies depending on the details of the models. If we accept results from neutron diffraction experiments, then we can identify a specific partition function model for PdD_x which is at the same time a good fit for the solubility data and is also consistent with the neutron diffraction data.

2. O-site Occupation and α-phase PdH_x and PdD_x Data

Hydrogen and deuterium solubility in Pd in the α-phase was studied experimentally by Clewley et al. [21], where data was reported for a wide range of temperatures from below 200 K to more than 1200 K. In this section we consider a simple analysis of the data based on a picture in which the interstitial hydrogen or deuterium is restricted to octahedral sites. If tetrahedral site occupation were to occur, one might expect that it should impact the analysis only at elevated temperature since the O-site to T-site excitation energy is expect to be on the order of 100–300 meV. Consequently we expect an analysis carried out assuming only O-site excitation should give reliable results in the low temperature regime.

2.1. Equilibrium between gas phase and solid phase deuterium

It is possible to develop a model for O-site occupation of deuterium starting from a picture in which gas phase D_2 is in equilibrium with solid phase interstitial deuterium in palladium. Under these conditions the chemical potential of deuterium in the two phases are equal [24,39]

$$\mu_{\rm D}^{\rm (s)} = \mu_{\rm D}^{\rm (g)} = \frac{1}{2}\mu_{\rm D_2}. \tag{1}$$

This is equivalent to the equilibrium constraints worked with by Fowler [22] and by Lacher [23].

2.2. Gas phase chemical potential

The chemical potential of deuterium in gas phase D_2 is well known, and can be written as [32,53]

$$\mu_{D_2} = -E_D + \mu_{\text{nonideal}} - k_B T \ln z_{\text{rot}}. \tag{2}$$

Here E_D is the dissociation energy [54]

$$E_D\ [H_2] = 4.4780\ \text{eV}, \tag{3}$$

$$E_D\ [D_2] = 4.5561\ \text{eV}. \tag{4}$$

The nonideal gas contribution to the chemical potential is

$$\mu_{\text{nonideal}} = k_B T \ln \left[\frac{f}{k_B T} \left(\frac{2\pi\hbar^2}{M k_B T} \right)^{3/2} \right], \tag{5}$$

where f is the fugacity and M is the mass of the molecule. For the fugacity of H_2 and of D_2 we make use of the model for H_2 of Joubert [55]; in the low pressure regime the fugacity is well approximated by the pressure. For the rotational partition function we use [56]

$$\text{PdH} : z_{\text{rot}} = 1 \sum_{\text{even } l} \sum_n (2l+1)\ \mathrm{e}^{-E_{\text{nl}}/k_B T} + 3 \sum_{\text{odd } l} \sum_n (2l+1)\ \mathrm{e}^{-E_{\text{nl}}/k_B T}, \tag{6}$$

$$\text{PdD} : z_{\text{rot}} = 6 \sum_{\text{even } l} \sum_n (2l+1)\ \mathrm{e}^{-E_{\text{nl}}/k_B T} + 3 \sum_{\text{odd } l} \sum_n (2l+1)\ \mathrm{e}^{-E_{\text{nl}}/k_B T}. \tag{7}$$

These partition functions includes the nuclear spin degeneracy explicitly. For the molecular energy levels E_{nl} we made use of the fits of Urey and Rittenberg [57].

At the temperatures of interest we do not expect electronic excitation, so the electronic degeneracy is 1; in this case

$$\mu_e = -k_B T \ln z_e = 0, \tag{8}$$

so there is no electronic contribution to the gas phase chemical potential. We neglect molecular dissociation.

2.3. Solid phase chemical potential

For solid phase interstitial deuterium we can write [32,13]

$$\mu_D = E_O + \theta_O \frac{\partial E_O}{\partial \theta} - k_B T \ln \frac{1-\theta_O}{\theta_O} - k_B T \ln z_O, \tag{9}$$

where E_O is the O-site energy, which in general depends on the temperature and on the D/Pd loading. The O-site fractional occupation is θ_O (which is the ratio of the number of interstitial O-site deuterium atoms to the number of Pd atoms). We take the partition function of an occupied O-site to be

$$z_O\ [\text{PdH}] = 4 \left(\frac{1}{1 - \mathrm{e}^{-\hbar\omega_O[\text{PdH}]/k_B T}} \right)^3, \tag{10}$$

$$z_{\rm O}\ [{\rm PdD}] = 6\left(\frac{1}{1-\ {\rm e}^{-\hbar\omega_{\rm O}[{\rm PdD}]/k_{\rm B}T}}\right)^3. \tag{11}$$

Normally this partition function is that of a three-dimensional harmonic oscillator [25] referenced to the potential minimum [30,32]; here we take the reference energy of the O-site to include the zero-point contribution. The spin 1/2 proton degeneracy is 2; the deuteron spin degeneracy is 3; and the electronic spin degeneracy is 2. The O-sites are modeled as oscillators with energies [58]

$$\hbar\omega_{\rm O}\ [{\rm PdH}] = 69.0\ {\rm meV}, \tag{12}$$

$$\hbar\omega_{\rm O}\ [{\rm PdD}] = 46.5\ {\rm meV}. \tag{13}$$

2.4. Analysis of the O-site energy

It is possible to develop an estimate for the O-site energy in the limit of zero loading (at low temperature) from experimental data. To do so, we rearrange Eq. (9) according to

$$E_{\rm O} + \theta_{\rm O}\frac{\partial E_{\rm O}}{\partial\theta} = \mu_{\rm D} + k_{\rm B}T\ln\frac{1-\theta_{\rm O}}{\theta_{\rm O}} + k_{\rm B}T\ln z_{\rm O}. \tag{14}$$

At sufficiently low loading the linear term of the left hand side becomes sufficiently small that it can be neglected, so we may write

$$E_{\rm O}(\theta\to 0)\ \to\ \mu_{\rm D} + k_{\rm B}T\ln\frac{1-\theta_{\rm O}}{\theta_{\rm O}} + k_{\rm B}T\ln z_{\rm O}. \tag{15}$$

In general the loading fraction θ is made up of O-site and T-site contributions ($\theta_{\rm O}$ and $\theta_{\rm T}$); if there were no T-site occupation then $\theta\to\theta_{\rm O}$).

In Clewley et al. [21] data is presented for the parameter

$$p\frac{(1-\theta)^2}{\theta^2}. \tag{16}$$

as a function of $1/T$. At low pressure the loading becomes sufficiently small that the estimate above for the O-site energy at zero loading above becomes accurate. Hence we can work with the experimentally observed solubility data to infer a value of $E_{\rm O}(\theta\to 0)$ for each data point based on

$$E_{\rm O}(\theta\to 0)\ \to\ \mu_{\rm D} + k_{\rm B}T\ln\frac{1-\theta}{\theta} + k_{\rm B}T\ln z_{\rm O}. \tag{17}$$

In the experimental data there could be both O-site and T-site contributions to θ; so in writing this we propose to infer the O-site energy from data that may have both O-site and T-site contributions. The results are plotted as a function of T in Fig. 1. One observes that the data points are roughly linear at low temperature; but once the temperature rises above about 400 K the dependence of this parameter deviates considerably from its low temperature behavior. This deviation from linearity for us is an indication that new physics might be present.

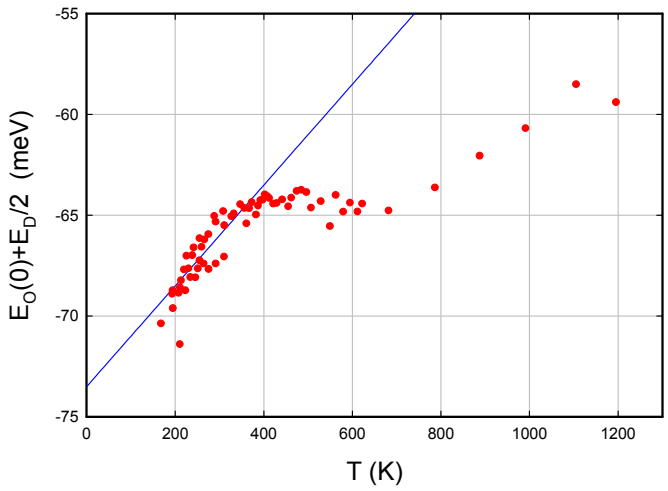

Figure 1. O-site energy at zero loading for α-phase PdD_x as a function of temperature estimated from the data of Clewley et al. [21] (red circles); linear fit to the data at low temperature (blue line).

2.5. Fermi level as a function of temperature

The increase in the O-site energy in the low temperature regime may be related to the change in the Fermi level with temperature. We recall that the Fermi level in a metal is determined by the charge neutrality constraint [56]

$$n_e = \int g(\epsilon) \frac{1}{1 + e^{(\epsilon-\mu_F)/k_B T}} d\epsilon, \tag{18}$$

where $g(\epsilon)$ is the density of states per unit volume and μ_F is the Fermi level. We have worked with the density of states of Mueller et al. [59] shown in Fig. 2. The resulting incremental Fermi level is shown in Fig. 3. This result is in good agreement with a similar computation of Fradin [60].

We have fit the incremental Fermi level as a function of T according to

$$\begin{aligned} \Delta\mu_F(T) &= \mu_F(T) - \mu_F(0) \\ &= a_0 + a_1 T + a_2 T^2 + a_3 T^3 + a_4 T^4 + a_5 T^5 + a_6 T^6 \end{aligned} \tag{19}$$

with T in Kelvin and with fitting coefficients given by

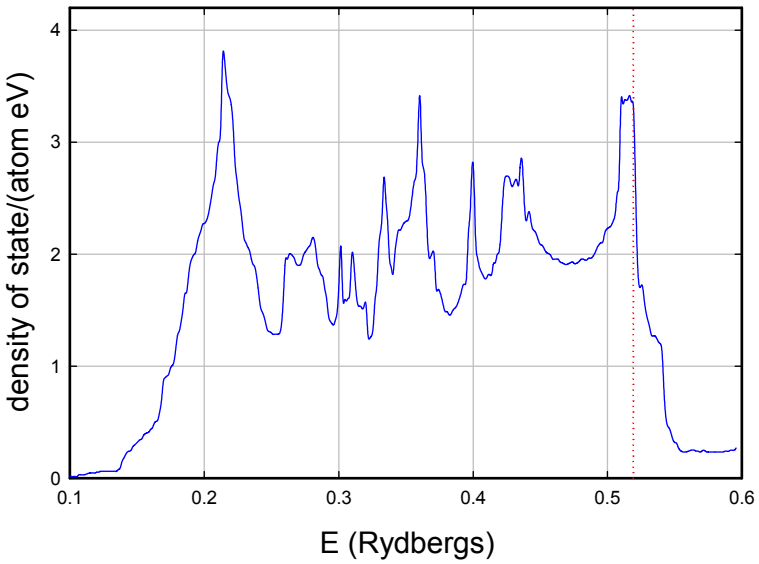

Figure 2. Density of state per unit volume for Pd from Mueller et al. [59] (blue line); Fermi level at $T = 0$ (red dotted line).

$$\begin{aligned}
a_0 &= 0.106352,\\
a_1 &= -0.0055007,\\
a_2 &= 0.000108379,\\
a_3 &= -1.53795 \times 10^{-7},\\
a_4 &= 1.24472 \times 10^{-10},\\
a_5 &= -5.12753 \times 10^{-14},\\
a_6 &= 8.53854 \times 10^{-18}.
\end{aligned} \tag{20}$$

2.6. Comparison of the O-site energy with data

We suspect that at low temperature the increase in the O-site energy at zero loading is dominated by the contribution of the incremental Fermi level. To pursue this we plot a shifted version of the data for both α-phase PdH_x and PdD_x with the incremental Fermi level in Fig. 4. Although there is much scatter in the data plotted this way, we conclude that there is a consistency between the electronic Fermi level shift and the O-site energies estimated from the data of Clewley et al. [21] below about 350 K.

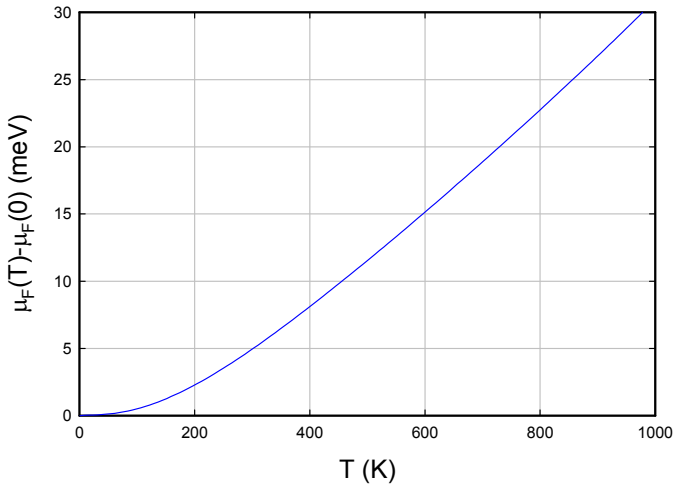

Figure 3. Incremental Fermi level for Pd as a function of temperature.

2.7. Interstitial partition function

Another interpretation of the data is possible, one which focuses on the partition function of interstitial hydrogen or deuterium. If we presume that the O-site energy is given by

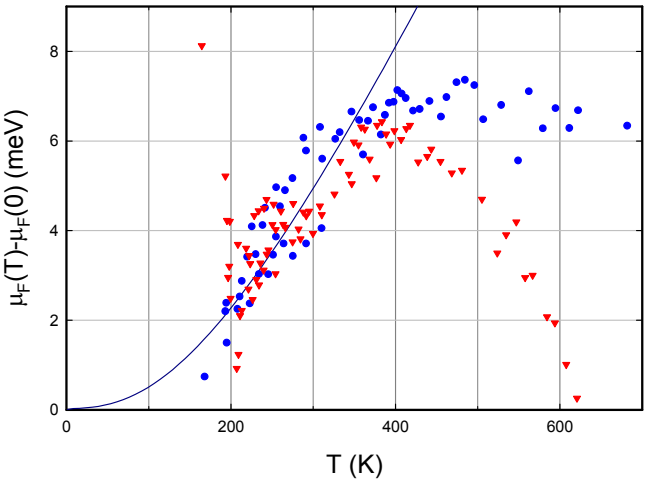

Figure 4. Shifted O-site energies for α-phase PdD_x (blue circles) and α-phase PdH_x (red triangles) as a function of temperature; also, incremental Fermi level (dark blue line) plotted as a function of temperature.

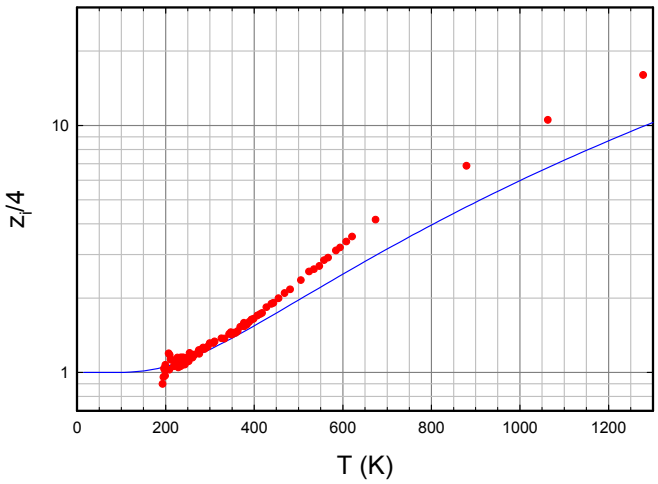

Figure 5. Scaled interstitial partition function as a function of temperature; experimental data of Clewley et al. for PdH_x represented as a scaled interstitial partition function as described in the text (red circles); analogous O-site partition function for a three-dimension simple harmonic oscillator (blue line).

$$E_{\rm O}(T) = E_{\rm O}(0) + \Delta\mu_{\rm F}(T) \tag{21}$$

as an ansatz, then we would be able to determine the partition function of the interstitials according to

$$z_{\rm i} = \left(\frac{\theta}{1-\theta}\right) \exp\left\{\frac{E_{\rm O}(0) + \Delta\mu_{\rm F}(T) - \mu_{\rm D}}{k_{\rm B}T}\right\}. \tag{22}$$

The idea here is that the θ from the experimental data may have both O-site and T-site contributions; we would use $z_{\rm O}$ for the O-site partition function, and $z_{\rm T}$ for the T-site partition function. In this equation $z_{\rm i}$ is the partition function of interstitial hydrogen or deuterium under conditions where both O-site and T-site occupation may be present. In this case we have experimental data points for θ at different temperatures, and if we assume a pressure then we can determine a corresponding value for the chemical potential. We can choose a value for $E_{\rm O}(0)$ to match the data at $T = 0$ so that $z_{\rm i}(0)$ goes to the appropriate statistical factor due to electronic and nuclear spin contributions.

In Fig. 5 is shown results for the data of Clewley et al. [21] for α-phase PdH_x analyzed in terms of the equivalent (and scaled) interstitial partition function, along with the analogous O-site partition function based on a 3D harmonic oscillator. The O-site energy at zero temperature for this plot is

$$E_{\rm O}(0) = -\frac{E_{\rm D}}{2} - 75.5 \text{ meV}. \tag{23}$$

The data plotted this way is interesting for a number of reasons. One is that at low temperature there is pretty good agreement, suggesting that the basic approach seems sound. And independent of any additional assumptions, if the O-site energy depends on temperature as in our ansatz, then the resulting partition function is already not too far from

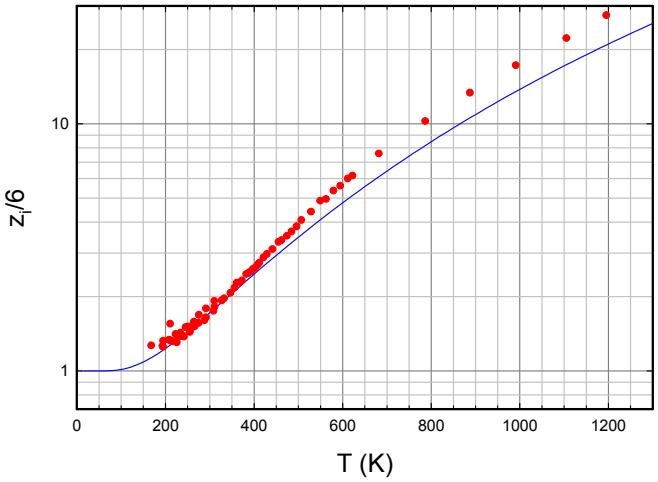

Figure 6. Scaled interstitial partition function as a function of temperature; experimental data of Clewley et al. for PdD_x represented as a scaled interstitial partition function as described in the text (red circles); analogous O-site partition function for a three-dimension simple harmonic oscillator (blue line).

that of a 3D harmonic oscillator over the entire temperature range. This is significant, as one would compute a very different partition function based on an embedded atom model potential, or based on the approach of Sazonov et al. [61].

The data plotted similarly for α-phase PdD_x is shown in Fig. 6. In this case the O-site energy at zero temperature is

$$E_O(0) = -\frac{E_D}{2} - 70.3 \text{ meV}. \tag{24}$$

Qualitatively the situation is very similar, except that in this case the deviation from the partition function of a 3D oscillator seems smaller (since the 3D oscillator partition function is larger in magnitude).

2.8. Discussion

One expects to be able to understand the solubility of hydrogen and deuterium in the α-phase at low temperature based on a simple picture with O-site occupation, and it is comforting that there is a reasonably good match between data and model in this regime. It would be possible to fit to a linear empirical model for the O-site energy; however, it is much more satisfying that the slope might be accounted for by the temperature dependence of the Fermi level.

It seems clear that this simple picture is not going to extend into the higher temperature regime without some modification. For both hydrogen and deuterium there is a substantial deviation in the inferred O-site energy of Fig. 4 once the temperature exceeds about 400 K. We also see that there is a significant difference in what happens at higher temperature in α-phase PdH_x as compared to α-phase PdD_x.

It is hard to imagine some effect cutting in at elevated temperature that would move the O-site energy as would be required to account for the results in Fig. 4. However, if we take the other point of view that the O-site energy changes only on account of the (smooth) change in the Fermi level, then we need to account for the temperature dependence of

the interstitial partition function of Figs. 5 and 6. In both cases one can imagine a scenario in which additional states at low energy would lead to additional contributions to the partition function. This prospect is pursued in Section 3.

3. Model Including Both O-sites and T-sites

Motivated by the discussion of Section 2 we are interested in whether the α-phase solubility data might be consistent with a small or modest amount of tetrahedral site occupation. Whether there should be any T-site occupation at all depends critically on how large the O-site to T-site excitation energy is. The results from embedded atom models, from density functional calculations, and from quantum chemistry calculations range between about 50 meV to about 300 meV. If the excitation energy were as low as 50 meV, then we would expect to see T-site occupation at modest temperature at low loading. On the other hand, if the excitation energy were near 300 meV then we would see very little T-site occupation. The best recent calculations give a low O-site to T-site excitation energy [14–20], and this provides us with motivation to compare model results against experimental data to check for consistency.

We have been interested recently in the development and application of models for both O-site and T-site occupation to understand what happens in PdH and PdD at high loading [13]. With experience gained from the earlier work we are motivated to apply the model to α-phase PdH_x and PdD_x.

3.1. Model for O-site and T-site occupation

From our earlier work on modeling O-site and T-site occupation [13], we can write

$$\mu_D = E_O + \theta_O \frac{\partial E_O}{\partial \theta} + \theta_T \frac{\partial E_T}{\partial \theta} - k_B T \ln \frac{1-\theta_O}{\theta_O} - k_B T \ln z_O, \tag{25}$$

$$\mu_D = E_T + \theta_T \frac{\partial E_T}{\partial \theta} + \theta_O \frac{\partial E_O}{\partial \theta} - k_B T \ln \frac{2-\theta_T}{\theta_T} - k_B T \ln z_T. \tag{26}$$

In the α-phase if the pressure is made sufficiently low the first-order terms can be neglected and the model reduces to

$$E_O \;\rightarrow\; \mu_D + k_B T \ln \frac{1-\theta_O}{\theta_O} + k_B T \ln z_O, \tag{27}$$

$$E_T \;\rightarrow\; \mu_D + k_B T \ln \frac{2-\theta_T}{\theta_T} + k_B T \ln z_T. \tag{28}$$

Since we do not have estimates for θ_O and θ_T separately from experiment, we cannot use these relations directly to determine the O-site and T-site energies. On the other hand it should be possible to estimate E_O and E_T by comparing different versions of the model against experiment to see which provides the best match.

3.2. Partition functions

For the discussion of this section we will make use of the 3D oscillator partition functions described in the previous section for O-site occupation. Similarly, for the T-sites we will use

$$z_T\,[\mathrm{PdH}] = 4\left(\frac{1}{1-\;\mathrm{e}^{-\hbar\omega_T\,[\mathrm{PdH}]/k_B T}}\right)^3, \tag{29}$$

$$z_{\rm T}\ [{\rm PdD}] = 6\left(\frac{1}{1-\ {\rm e}^{-\hbar\omega_{\rm T}\ [{\rm PdD}]/k_{\rm B}T}}\right)^3 \tag{30}$$

and determine values for $\hbar\omega_{\rm T}$ [PdD] and $\hbar\omega_{\rm T}$ [PdH] from optimization.

3.3. Boundary condition at low temperature and ansatz

We have seen that the O-site energy $E_{\rm O}(T)$ temperature dependence is given by the Fermi level shift at low temperature. We will take as an ansatz in our discussion that this also holds at higher temperature; hence

$$E_{\rm O}(T) = E_{\rm O}(0) + \Delta\mu_{\rm F}(T). \tag{31}$$

Since the lattice expands a little as the temperature increases, we might expect that the oscillator energy should decrease. There may be other more subtle effects coming in as well. The idea here is that it may be that these effects altogether are relatively small, and by neglecting them we can focus on T-site occupation. Whether this approach in general is a good one or not will depend ultimately on the results obtained.

3.4. Simple empirical model and optimization

With a specification of the O-site energy, we adopt a similar strategy for the O-site to T-site excitation energy and write

$$\Delta E(T) = \Delta E(0). \tag{32}$$

It would reasonably be expected that terms linear in temperature should not be present in this kind of model, as we would not expect deviations at low temperature from the parts of the model already included. Higher-order terms are simply neglected for this discussion.

This model has three free parameters altogether that can be chosen to minimize a measure of the error given by

$$I = \frac{\displaystyle\sum_{i=1}^{N} w_i \left[\ln\left\{p_i\left(\frac{1-\theta_i}{\theta_i}\right)^2\right\}_{\rm exp} - \ln\left\{p_i\left(\frac{1-\theta_i}{\theta_i}\right)^2\right\}_{\rm model}\right]^2}{\displaystyle\sum_i w_i}. \tag{33}$$

There are many more data points at the lower temperatures, so we have weighted the data points at high temperature higher to compensate.

3.5. Results for α-phase PdD_x

Optimization of the model parameters leads to

$$E_{\rm O}(0) = -\frac{E_{\rm D}}{2} - 70.73\ {\rm meV}, \tag{34}$$

$$\Delta E(0) = 101.81\ {\rm meV}, \tag{35}$$

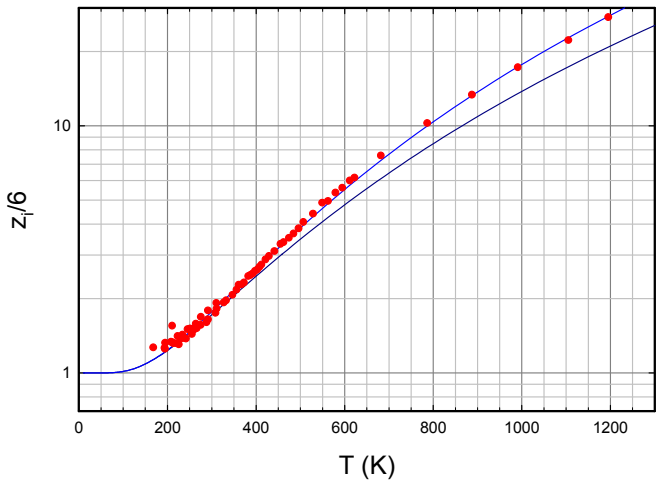

Figure 7. Scaled interstitial partition function versus temperature for α-phase PdD_x; data of Clewley et al. [21] (red circles); 3D oscillator O-site partition function; optimized three-parameter model partition function including O-site and T-site occupation.

$$\hbar\omega_{\rm T}\ [{\rm PdD}] = 66.62\ {\rm meV}. \tag{36}$$

The associated error for this model is

$$I = 0.00480. \tag{37}$$

A comparison of the results for this model and the data of Clewley et al. [21] is shown in Fig. 7. One observes that the model results match well with experiment.

3.6. Input from neutron diffraction experiments

Neutron diffraction experiments seeking tetrahedral occupation in PdD_x were reported by Pitt and Gray [62]. Experiments run at elevated temperature gave positive results for T-site occupation at 309°C. Based on the results given for O-site and T-site occupation separately, the O-site to T-site excitation energy can be determined according to

$$E_{\rm T} - E_{\rm O} = k_{\rm B}T\left\{\ln\left(\frac{2-\theta_{\rm T}}{\theta_{\rm T}}\frac{\theta_{\rm O}}{1-\theta_{\rm O}}\right) + \ln\frac{z_{\rm T}}{z_{\rm O}}\right\}. \tag{38}$$

Results from this analysis are shown in Fig. 8, along with the results from a quadratic least squares fit. The extrapolated value for zero loading is

$$\Delta E(582\ {\rm K}) = 41.6\ {\rm meV}. \tag{39}$$

This value is much lower than the 101.81 meV number obtained from the data of Clewley et al. [21]; both numbers are "low", consistent with the low excitation energies computed in the recent literature, but they do not seem so consistent with each other at this point.

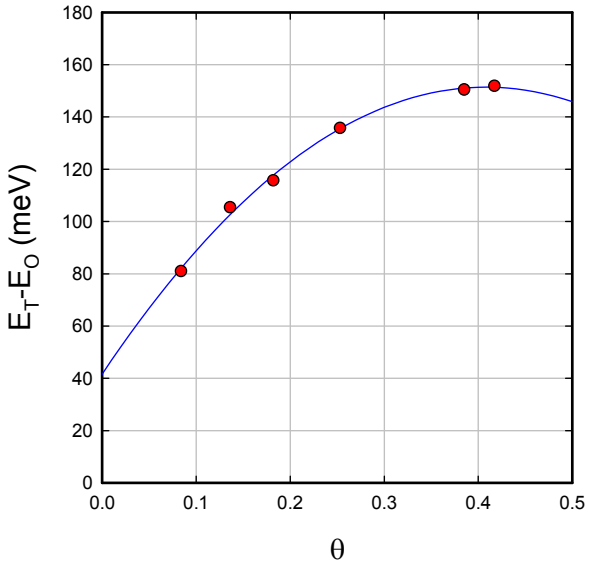

Figure 8. O-site to T-site excitation energy estimated from the neutron diffraction data of Pitt and Gray [62] as a function of loading (red circles); least squares quadratic fit (blue line).

3.7. Result for α-phase PdH_x

A similar optimization for α-phase PdH_x produces

$$E_{\rm O}(0) = -\frac{E_{\rm D}}{2} - 75.09 \text{ meV}, \tag{40}$$

$$\Delta E(0) = 93.24 \text{ meV}, \tag{41}$$

$$\hbar\omega_{\rm T} \text{ [PdH]} = 77.93 \text{ meV}. \tag{42}$$

The error in this case is a bit larger

$$I = 0.00542. \tag{43}$$

A comparison of this fit against the data of Clewley et al. [21] is shown in Fig. 9. The agreement is pretty good.

3.8. Zero-point energy difference

If α-phase PdH_x and α-phase PdD_x were otherwise the same, then we might expect $\Delta E(0)$ to be larger in α-phase PdH_x by the difference in the zero-point energies, which was estimated to be 21.1 meV [13] from the calculations of Ke and Kramer [14]

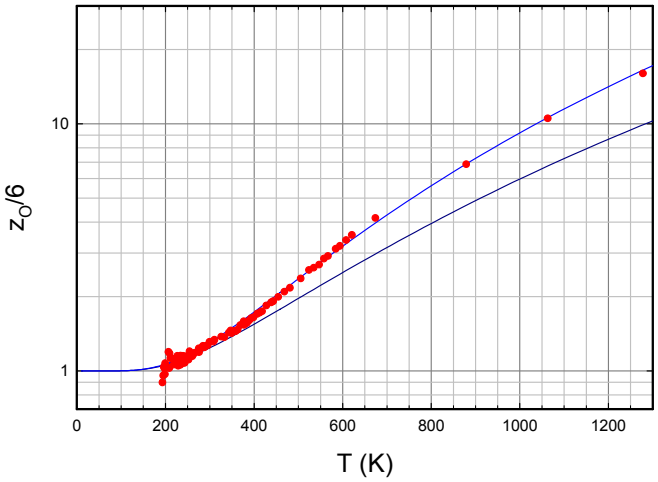

Figure 9. Interstitial partition function versus temperature for α-phase PdH_x; data of Clewley et al. [21] (red circles); 3D oscillator O-site partition function; optimized three-parameter model partition function including O-site and T-site occupation.

$$\left[\Delta E(0)\right]_{\rm PdH} = \left[\Delta E(0)\right]_{\rm PdD} + 21.1 \text{ meV}. \tag{44}$$

The O-site to T-site excitation energies obtained from the optimization of the simple models above are close, but reversed. One would like better agreement, but it would be too much to argue for inconsistency in this case.

3.9. Discussion

We are very much encouraged by the results from optimization of the simple empirical model outlined in this section. Based on the general approach we would expect the model to be most relevant at low temperature; however, the optimizations discussed here are based on global fits over the entire temperature range. The O-site to T-site excitation energies inferred from this analysis are not as close as we might like with results from neutron diffraction measurements, and are reversed relative to what we expect due to zero-point contributions. Neither of these at this point are major inconsistencies.

The model results are shown against $p(1-\theta)^2/\theta^2$ as a function of 1000 K/T in Fig. 10. The results look very good.

4. Improved Empirical Model

Without question there is a some significant success in the application of simple empirical models with both O-site and T-site occupation to the data set of Clewley et al. [21] from the results of Section 3. However, we are motivated to attempt a similar analysis with better models, in the hope of improving consistency with the neutron diffraction data and with the zero-point contribution to the excitation energy. An added benefit is that we will gain some intuition on how sensitive the results are to details of the model used.

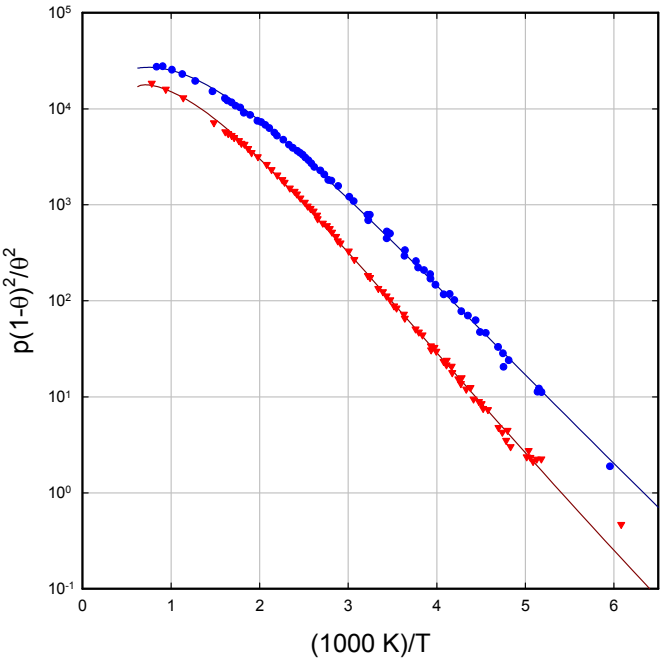

Figure 10. Plot of $p(1-\theta)^2/\theta^2$ for α-phase PdD_x as a function of (1000 K)/T; data set of Clewley et al. [21] for PdH_x (red circles); optimized three-parameter empirical model for PdH_x (red line); data set of Clewley et al. [21] for PdD_x (blue circles); optimized three-parameter empirical model for PdD_x (blue line).

One issue that we might recognize in this discussion is that the excited states as observed from inelastic neutron scattering experiments deviate from those of a three-dimensional harmonic oscillator potential; we can work with a model that is in better agreement with levels that have been observed. We have little guidance from experiment as to what kind of potential we are dealing with for T-site occupation. Due to the relatively low T-site occupation the model is less sensitive to the details. In what follows we will optimize the parameters of the model for the T-site partition function.

4.1. O-site excited state energy levels

The excited state energy levels in PdH from Ross et al. [63] are shown in Fig. 11. Also plotted is a fit based on

$$E_n = \hbar\omega_O n^s \tag{45}$$

with s least squares fit to the data ($s = 1.195$). We include the zero-point energy in the specification of the O-site ground state energy used in the empirical model. This suggests that we might improve the O-site partition function by evaluating it directly with scaled energies

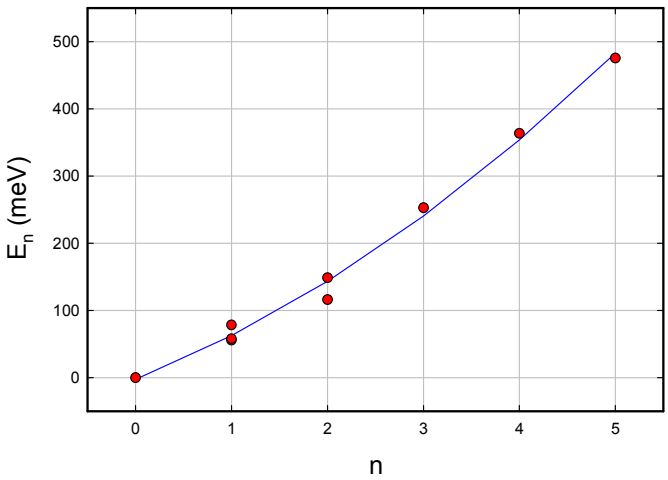

Figure 11. O-site energy levels as a function of the number of quanta for α-phase PdH_x from Ross et al. [63] (red circles); empirical fit (blue line).

$$z_{\rm O}\,[{\rm PdH}] = 2 \times 2 \times \left[\sum_n \exp\left\{ -\frac{E_n}{k_{\rm B}T} \right\} \right]^3 . \tag{46}$$

This approach is one of the simplest possible that includes non-SHO effects. In the models discussed in this section, we have used this approach for the O-site with $s_{\rm O} = 1.2$; for the T-site partition function we will work with different values for $s_{\rm T}$.

4.2. Optimization in the case of α-phase PdD_x

We have optimized a version of the model against the data of Clewley et al. [21] as described in the previous section for different values of $s_{\rm T}$ with the results listed in Table 1. The error is reduced as $s_{\rm T}$ is increased up to a value of 1.636 which is the optimum value if $s_{\rm T}$ is optimized along with the other parameters. We recall that a value of $s = 1$ corresponds to a parabolic potential well in 3D and $s = 2$ corresponds to a square well in 3D; a value of $s = 1.6$ would then imply a T-site well more like a square well than a parabolic well.

Table 1. Fitting parameters for O-site to T-site model for α-phase PdD_x.

$E_{\rm O} + \frac{E_{\rm D}}{2}$ (meV)	$\Delta E(0)$ (meV)	$\hbar\omega_{\rm T}$ [PdD] (meV)	$s_{\rm T}$	I
−70.71	84.9	50.9	1.0	0.00492
−70.90	96.7	39.0	1.2	0.00399
−71.02	107.3	30.1	1.4	0.00361
−71.09	116.7	23.3	1.6	0.00347
−71.10	118.0	22.3	1.636	0.00346

Table 2. Fitting parameters for O-site to T-site model for α-phase PdH_x.

$E_O + \frac{E_D}{2}$ (meV)	$\Delta E(0)$ (meV)	$\hbar\omega_T$ [PdD] (meV)	s_T	I
−75.05	90.4	66.8	1.0	0.00548
−75.21	99.6	53.8	1.2	0.00487
−75.31	108.2	43.7	1.4	0.00464
−75.39	116.1	35.6	1.6	0.00458
−75.39	117.1	34.7	1.627	0.00458

We see that the O-site to T-site excitation energy that produces the best fit with the experimental data increases with the T-site excited state parameter s_T.

4.3. Optimization in the case of α-phase PdH_x

We have optimized a version of the model against the data of Clewley et al. [21] as described in the previous section, with results given in Table 2. One sees a similar trend that the error decreases as s_T increases, this time up to an optimum value of s_T of 1.627.

The excitation energy for PdH_x is seen to increase with s_T similarly to the earlier results for PdD_x.

4.4. Checking consistency with neutron diffraction measurements

We recall that the O-site to T-site excitation energy can be estimated from the neutron diffraction data from

$$E_T - E_O = k_B T \left\{ \ln\left(\frac{2-\theta_T}{\theta_T} \frac{\theta_O}{1-\theta_O} \right) + \ln \frac{z_T}{z_O} \right\}.$$

In our empirical model the excitation energy is assumed independent of temperature, so $E_T - E_O$ here can be compared against our $\Delta E(0)$. The O-site and T-site occupations are given numerically in Pitt and Gray (2002). However, with different models for the O-site and T-site partition functions the ratio of z_T/z_O is now model dependent. In order to check for consistency we need to re-evaluate the excitation energy for the different models. The results are given in Table 3. The empirical model is consistent with the neutron scattering data for $s_T = 1.36$, at an excitation energy of 105.1 meV.

4.5. Results

In the case of α-phase PdD_x we can specify an empirical model which has a lower error than what was found in the previous section, and which is also consistent with the neutron diffraction data. It seems reasonable to assume a similar value for s_T for α-phase PdH_x. The model parameters are listed in Table 4.

Table 3. Comparison of model O-site to T-site excitation energy and excitation energy from neutron diffraction data for different values of s_T.

s_T	model: $\Delta E(0)$ (meV)	data: $E_T - E_O$ (meV)
1.0	84.9	124.1
1.2	96.7	111.7
1.4	107.3	104.0
1.6	116.7	98.9

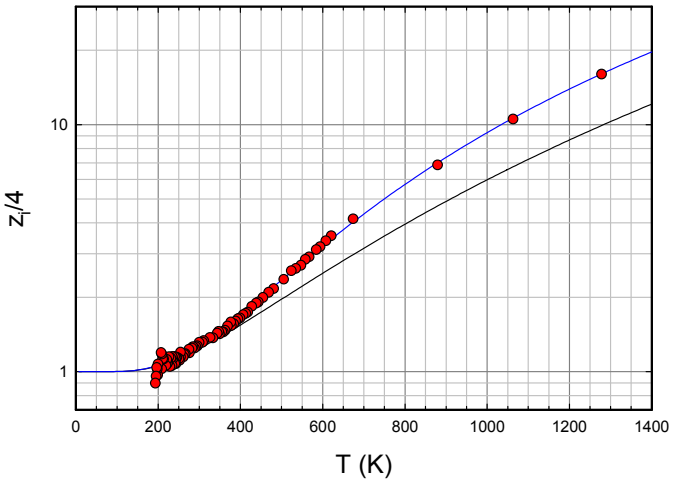

Figure 12. Scaled interstitial partition function versus temperature for α-phase PdH_x; data of Clewley et al. [21] (red circles); 3D oscillator O-site partition function; optimized model partition function including O-site and T-site occupation.

In Figs. 12 and 13 we show the interstitial partition functions for α-phase PdH_x and PdD_x. In both cases the agreement is excellent. In Fig. 14 the data is plotted as in Clewley et al. [21] as $p(1-\theta)^2/\theta^2$ as a function of 1000 K/T; the agreement is again excellent.

In Fig. 15 are shown the O-site and T-site relative occupations

$$\frac{\theta_O}{\theta} = \frac{\theta_O}{\theta_O + \theta_T}, \qquad \frac{\theta_T}{\theta} = \frac{\theta_T}{\theta_O + \theta_T}. \tag{47}$$

The T-site values seem high at elevated temperature; however, if the neutron scattering data of Pitt and Gray [62] are correct, then such high values are needed for consistency. It may be that this data is compromised due to the presence of a substantial number of monovacancies; if so then the T-site occupation would be overestimated. We note that it is straightforward to construct empirical models that fit the data of Clewley et al. [21] very nearly as well that predict a lower T-site occupation. In essence, the data of Clewley et al. [21] seems consistent with substantial T-site occupation, but additional input from experiment is required to determine more precisely how much T-site occupation is present.

5. Discussion and Conclusions

This study was motivated initially by an interest in estimating the O-site to T-site excitation energy at zero loading in order to develop an improved model for PdH and PdD at high loading. We had available a model for both O-site and

Table 4. Fitting parameters for O-site to T-site models for α-phase PdD_x and PdH_x.

	$E_O + \frac{E_D}{2}$ (meV)	$\Delta E(0)$ (meV)	$\hbar\omega_O$ (meV)	s_O	$\hbar\omega_T$(meV)	s_T	I
PdD_x	−71.00	105.3	46.5	1.2	31.6	1.36	0.00366
PdH_x	−75.30	106.5	69.0	1.2	45.5	1.36	0.00467

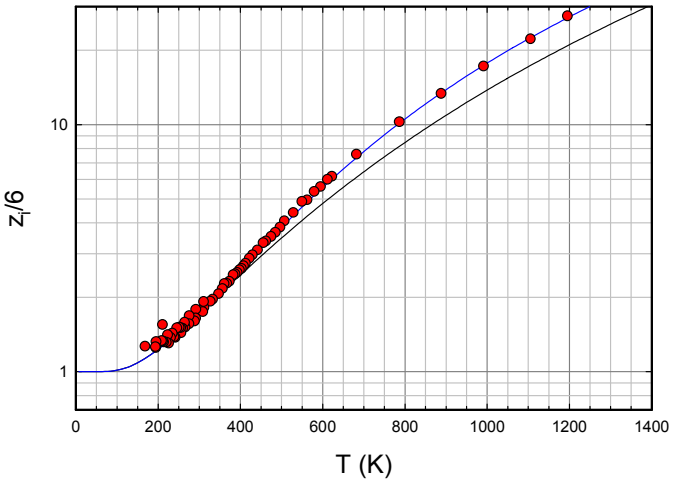

Figure 13. Scaled interstitial partition function versus temperature for α-phase PdD_x; data of Clewley et al. [21] (red circles); 3D oscillator O-site partition function (black line); optimized model partition function including O-site and T-site occupation (blue line).

T-site excitation, one which we had experience with, and also some confidence in. What made this study possible was the data set published be Clewley et al. [21] and an ability to scan it so that we could work with it in digitized form. There was no reason to believe a priori that it would be possible to extract much from the data, other than some evidence either for or against there being signs of T-site occupation.

However, in the course of the study it began to become clear that a model with both O-site and T-site occupation was very relevant to the data, and that interpreting the data based on a model with O-site occupation alone would require some awkward assumptions. We tried a very large number of different approaches an empirical models while studying the problem. A key insight which changed our approach was the recognition that it was possible to account for the approximate linear dependence of the O-site energy at low temperature by the Fermi level shift. With this dominant term included explicitly, it began to emerge that additional corrections were higher order and likely small. This suggested the ansatz that we might be able to understand the system by discarding all temperature dependence other than the Fermi level shift in a model for $E_O(T)$.

Once the ansatz was adopted, the data seemed to make sense in terms of relatively simple models. Improving the O-site partition function led to better agreement with the data. We had considered the possibility that all model parameters could be extracted directly from the data in a brute force optimization. It would have been very powerful to have been able to extract the O-site excited state spectrum directly from the data set. Unfortunately there are too many degrees of freedom present, and the overall mathematical optimum leads to a picture that is very much not physically compelling. However, with input from inelastic neutron scattering measurements it was possible to assign solid values to some of the model parameters, and then optimize against the data to determine others.

If we make use of a simple version of the empirical model based on partition functions for 3D harmonic oscillators, then immediately we are able to fit the data well based on physically reasonable model parameters. The O-site and T-site excitation energies that result are 101.81 meV for PdD_x and 93.24 meV for PdH_x. Although there are some minor issues with respect to consistency with neutron diffraction data and the zero-point energy difference, the results

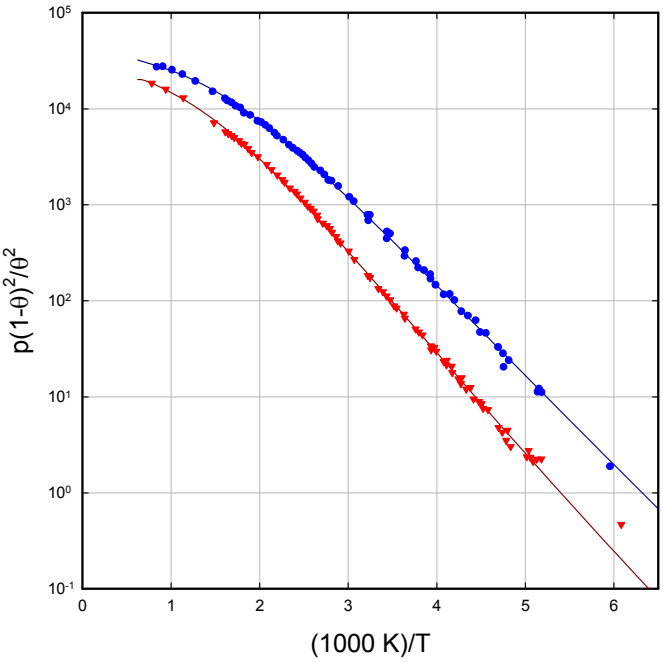

Figure 14. Plot of $p(1-\theta)^2/\theta^2$ for α-phase PdD_x as a function of (1000 K)/T; data set of Clewley et al. [21] for PdH_x (red circles); optimized empirical model for PdH_x (red line); data set of Clewley et al. [21] for PdD_x (blue circles); optimized empirical model for PdD_x (blue line).

are both interesting and probably worth taking seriously. The excitation energies are close to the best numbers from recent theoretical models.

Based on this strong initial result, we were motivated to explore further and see whether it might be possible to extract more from the experimental data set of Clewley et al. [21]. The key issue in this case has to do with the O-site and T-site partition functions. Based on inelastic neutron scattering experiments, we know that the excited state energies of O-site PdH do not scale with energy as a 3D simple harmonic oscillator. Consequently, we might expect to do better if we use a more realistic partition function for the O-sites; as discussed above we end up with smaller errors when we do. We have much less to rely on in the case of the T-site partition function. In this case we can make use of the data set to optimize, and we find a relation between the T-site energy level scaling parameter s_T and the excitation energy. The optimization of s_T in α-phase PdD_x leads to a value of 1.36, which suggests that the T-site is further from being a spherical harmonic oscillator than the O-site. Without analogous input for α-phase PdH_x we adopted the same s_T, even though there is good reason to believe it might be different. Optimization with the resulting non-SHO models leads to estimates for the excitation energy at zero loading of 105.3 meV for PdD_x, and 106.5 meV for PdH_x. We had hoped for a difference in excitation energy between the two cases consistent with the zero-point energy difference (21.1 meV); the energies we found are nearly the same, a result which is compatible with the low prediction based on the zero-point energy.

Perhaps the biggest issue is the substantial T-site occupation fraction, implied by the neutron diffraction data of Pitt

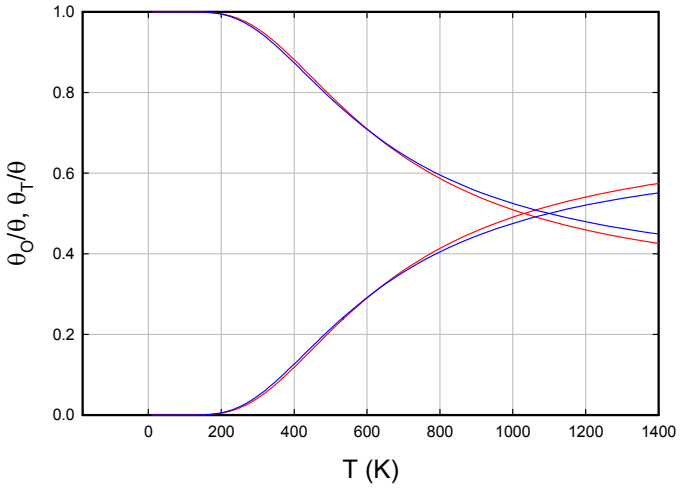

Figure 15. Fractional O-site occupation for α-phase PdH_x (lower red line) and PdD_x (lower blue line), and fractional T-site occupation for α-phase PdH_x (upper red line) and PdD_x (upper blue line).

and Gray [62], and predicted by the empirical models especially at elevated temperature. One should expect significant T-site occupation based on the theoretical estimates from modern structure calculations. However, this is one issue that those familiar with metal hydrides in general, and PdH and PdD in particular, are unlikely to accept without additional confirming experimental data.

The model O-site to T-site excitation energy for α-phase PdD_x depends on what is assumed about the T-site partition function, which is not available at present independently from experiment. If in the future α-phase solubility measurements are done in which the O-site and T-site occupation is determined individually, from the results we would be able to eliminate much uncertainty about excitation energies and partition functions. At present an estimate of 105.3 meV for the excitation energy for α-phase PdD_x seems most consistent with the data we have; but values in the range of 90-110 meV seem possible. The uncertainty is a bit larger for α-phase PdH_x.

Acknowledgments

Assistance from Florian Metzler is acknowledged, who made use of the online digitizer program WebPlotDigitizer of Ankit Rohagti (http://arohatgi.info/WebPlotDigitizer) to digitize the data sets from Clewley et al. [21]. We would like to thank Industrial Heat for support for some of the research reported here.

References

[1] Y. Ebisuzaki and M. O'Keeffe, The solubility of hydrogen in transition metals and alloys, *Progress Solid State Chem.* **4** (1967) 187–211.

[2] E. Wicke, H. Brodowsky and H. Züchner, Hydrogen in palladium and palladium alloys, in *Hydrogen in Metals, Vol. 2*, Springer, Berlin, 1978, pp. 73–155.

[3] W. A. Oates and T. B. Flanagan, The solubility of hydrogen in transition metals and their alloys, *Progress Solid State Chem.* **13** (1981) 193–272.

[4] T.B. Flanagan, Thermodynamics of metal–hydrogen systems, in *Metal Hydrides*, Springer, Berlin, 1981, pp. 361–377.
[5] E. Wicke, Some present and future aspects of metal–hydrogen systems, *Zeitschrift für Physikalische Chemie* **143** (1985) 1–21.
[6] N.A. Gokcen, Interstitial Solutions, in *Statistical Thermodynamics of Alloys*, Springer, Berlin, 1986, pp. 149–193.
[7] L. Schlapbach, *Hydrogen in Intermetallic Compounds I.*, Springer, New York, 1988.
[8] R.Lässer, Properties of protium, deuterium and tritium in selected metals, in *Tritium and Helium-3 in Metals*, Springer, Berlin, 1989, pp. 48–107.
[9] T. B. Flanagan, and W. A. Oates, The palladium–hydrogen system, *Ann. Rev. Materials Sci.* **21** (1991) 269–304.
[10] Y. Fukai, *The Metal–Hydrogen System* Springer, New York, 1991.
[11] F.D. Manchester, A. San-Martin and J.M. Pitre, The H–Pd (hydrogen–palladium) system, *J. phase Equilibria* **15** (1994) 62–83.
[12] J.M. Joubert and S. Thiébaut, Thermodynamic assessment of the Pd-–H-–D-–T system, *J. Nucl. Materials* **395** (2009) 79–88.
[13] P.L. Hagelstein, An empirical model for octahedral and tetrahedral occupation in PdH and in PdD at high loading, *J. Condensed Matter Nucl. Sci.*, (in press).
[14] X. Ke and G.J. Kramer, Absorption and diffusion of hydrogen in palladium–silver alloys by density functional theory, *Phy. Rev. B* **66** (2002) 184304.
[15] P. Kamakoti and D.S. Sholl, A comparison of hydrogen diffusivities in Pd and CuPd alloys using density functional theory, *J. Membrane Sci.* **225** (2003) 145–154.
[16] S.Z. Baykara, Theoretical evaluation of diffusivity of hydrogen in palladium and rhodium, *Int. J. Hydrogen Energy* **29** (2004) 1631–1636.
[17] N. Ozawa, T.A. Roman, H. Nakanishi, H., Kasai, N.B. Arboleda Jr. and W.A. Dino, Potential energy of hydrogen atom motion on Pd (111) surface and in subsurface: A first principles calculation, *J. Appl. Phys.* **101** (2007) 123530.
[18] H, Grönbeck and V.P. Zhdanov, Effect of lattice strain on hydrogen diffusion in Pd: A density functional theory study, *Phy. Rev. B* **84** (2011) 052301.
[19] T.P. Senftle, M.J. Janik and A.C. van Duin, A reaxff investigation of hydride formation in palladium nanoclusters via Monte Carlo and molecular dynamics simulations, *J. Phy. Chem. C* **118** (2014) 4967–4981.
[20] R. Nazarov, T. Hickel and J. Neugebauer, Ab initio study of H-vacancy interactions in fcc metals: Implications for the formation of superabundant vacancies, *Phy. Rev. B* **89** (2014) 144108.
[21] J.D. Clewley, T. Curran, T.B. Flanagan and W.A. Oates, Thermodynamic properties of hydrogen and deuterium dissolved in palladium at low concentrations over a wide temperature range, *J. Chemical Soc., Faraday Trans. 1: Phy. Chem. in Condensed Phases* **69** (1973) 449–458.
[22] R.H. Fowler and C.J. Smithells, A theoretical formula for the solubility of hydrogen in metals, *Proc. Roy. Soc. London. Ser. A, Mathematical and Phy. Sci.* **160** (1937) 37–47.
[23] J.R. Lacher, A theoretical formula for the solubility of hydrogen in palladium, *Proc. Roy. Soc. London. Ser. A, Mathematical and Phy. Sci.* **161** (1937) 525–545.
[24] A. Harasima, T. Tanaka and K. Sakaoku, Cooperative phenomena in Pd–H system I, *J. Phy. Soc. Japan* **3** (1948) 208–213.
[25] T. Tanaka, K. Sakaoku and A. Harasima, Cooperative phenomena in Pd–H system II, *J. Phy. Soc. Japan* **3** (1948) 213–218.
[26] A. L. G. Rees, Statistical mechanics of two-component interstitial solid solutions, *Trans. Faraday Soc.* **50** (1954) 335–342.
[27] R.V. Bucur and M. Crisan, Interprétation mécanique-statistique de l'isotherme de solubilité de l'hydrogène en phase d'hydrure pour les métaux palladium, vanadium, niobium et tantale, *J. Phys. and Chem. of Solids* **28** (1967) 995–1000.
[28] R. Burch, Theoretical aspects of the absorption of hydrogen by palladium and its alloys. Part 1. A reassessment and comparison of the various proton models, *Trans. Faraday Soc.* **66** (1970) 736–748.
[29] T. Hashino and S. Naito, A contribution to the thermodynamics of the interstitial solid solution of hydrogen in metals, *J. Chemical Phys.* **64** (1976) 1016–1021.
[30] H. Ogawa, A statistical-mechanical method to evaluate hydrogen solubility in metal, *J. Phy. Chem. C* **114** (2010) 2134–2143.
[31] V. Tserolas, M. Katagiri, H. Onodera and H. Ogawa, Thermodynamical Modeling of PC Isotherms for Metal Hydride Materials, *Trans. Materials Res. Soc. Japan* **35** (2010) 221–226.
[32] P.O. Orondo, A theoretical model of interstitial hydrogen: pressure-composition-temperature, chemical potential, enthalpy and entropy, MIT Ph.D. Thesis, 2012.
[33] C. Wadell, T. Pingel, E. Olsson, I. Zoric, V.P. Zhdanov and C. Langhammer, Thermodynamics of hydride formation and decomposition in supported sub-10 nm Pd nanoparticles of different sizes, *Chemical Phys. Lett.* **603** (2014) 75–81.

[34] K.A. Moon, Pressure-composition-temperature relations in the palladium–hydrogen system, *J. Phy. Chem.* **60** (1956) 502–504.
[35] D.H. Everett and P. Nordon, Hysteresis in the palladium+hydrogen system, *Proc. Roy. Soc. London A: Mathematical, Phy. and Eng. Sci.* **259** (1960) 341–360.
[36] T.B. Flanagan, Absorption of deuterium by palladium, *J. Phy. Chem.* **65** (1961) 280–284.
[37] J.W. Simons and T.B. Flanagan, Absorption isotherms of hydrogen in the α-Phase of the hydrogen–palladium system, *J. Phy. Chem.* **69** (1965) 3773–3781.
[38] R. Burch and N.B. Francis, N.B. Pressure against composition isotherms and thermodynamic data for the α-phase of the palladium/hydrogen system, *J. Chemical Soc., Faraday Trans. 1: Phy. Chem. in Condensed Phases* **69** (1973) 1978–1982.
[39] T.B. Flanagan and J.F. Lynch, Thermodynamics of a gas in equilibrium with two nonstoichiometric condensed phases. Application to metal/hydrogen systems, *J. Phy. Chem.* **79** (1975) 444–448.
[40] M.J.B. Evans and D.H. Everett, Thermodynamics of the solution of hydrogen and deuterium in palladium, *J. Less Common Metals* **49** (1976) 123–145.
[41] C. Labes and R.B. McLellan, Thermodynamic behavior of dilute palladium–hydrogen solid solutions, *Acta Metallurgica* **26** (1978) 893–899.
[42] C. Picard, O.J. Kleppa and G. Boureau, A thermodynamic study of the palladium–hydrogen system at 245–352^o C and at pressures up to 34 atm, *J. Chemical Phys.* **69** (1978) 5549–5556.
[43] T.B. Flanagan, Enthalpy and entropy changes for non-stoichiometric hydride formation, *J. Less Common Metals* **63** (1979) 209–223.
[44] O.J. Kleppa and R.C. Phutela, A calorimetric-equilibrium study of dilute solutions of hydrogen and deuterium in palladium at 555 to 909 K, *J. Chemical Phys.* **76** (1982) 1106–1110.
[45] R. Lässer and K.H. Klatt, Solubility of hydrogen isotopes in palladium, *Phy. Rev. B* **28** (1983) 748.
[46] R. Lässer, Solubility of protium, deuterium, and tritium in the α phase of palladium, *Phy. Rev. B* **29** (1984) 4765.
[47] R. Lässer and G.L. Powell, Solubility of H, D, and T in Pd at low concentrations, *Phy. Rev. B* **34** (1986) 578.
[48] W.A. Oates, R. Laesser, T. Kuji and T.B. Flanagan, The effect of isotopic substitution on the thermodynamic properties of palladium–hydrogen alloys, *J. Phys. Chem. Solids* **47** (1986) 429–434.
[49] E. Wicke and J. Blaurock, New experiments on and interpretations of hysteresis effects of Pd–D_2 and Pd–H_2, *J. Less Common Metals* **130** (1987) 351–363.
[50] T.B. Flanagan, W. Luo and J.D. Clewley, Calorimetric enthalpies of absorption and desorption of protium and deuterium by palladium, *J. Less Common Metals* **172** (1991) 42–55.
[51] O. Beeri, D Cohen, Z Gavra and M.H. Mintz, The interpretation of hydrogen isotope effects and their relation to microscopic energy related parameters by simplified statistical thermodynamic models, *Physica Scripta* **T94** (2001) 88.
[52] W. Luo, D. Cowgill, R. Causey and K. Stewart, Equilibrium isotope effects in the preparation and isothermal decomposition of ternary hydrides $Pd(H_xD_{1-x})_y$ ($0 < x < 1$ and $y > 0.6$), *The J. Phy. Chem. B* **112** (2008) 8099–8105.
[53] E.A. Crespo, S. Claramonte, M. Ruda and S.R. de Debiaggi, Thermodynamics of hydrogen in Pd nanoparticles, *Int. J. Hydrogen Energy* **35** (2010) 6037–6041.
[54] W. Kolos and L. Wolniewicz, Improved theoretical ground-state energy of the hydrogen molecule, *J. Chemical Phys.* **49** (1968) 404–410.
[55] J.-M. Joubert, A Calphad-type equation of state for hydrogen gas and its application to the assessment of Rh–-H system, *Int. J. Hydrogen Energy* **35** (2010) 2104.
[56] P.L. Hagelstein, S.D. Senturia and T.P. Orlando, *Introductory Applied Quantum and Statistical Mechanics*, Wiley, 1984.
[57] H.C. Urey and D. Rittenberg, Some thermodynamic properties of the H1H2, H2H2 molecules and compounds containing the H2 atom, *J. Chemical Phys.* **1** (1933) 137–143.
[58] C. Elsässer, K.M. Ho, C.T. Chan and M. Fähnle, Vibrational states for hydrogen in palladium, *Phy. Rev. B* **44** (1991) 10377.
[59] F.M. Mueller, A.J. Freeman, J.O. Dimmock and A.M. Furdyna, Electronic structure of palladium, *Phy. Rev. B* **1** (1970) 4617.
[60] F.Y. Fradin, Effect of structure in the electronic density of states on the temperature dependence of the electrical resistivity, *Phy. Rev. Lett.* **33** (1974) 158.
[61] A.B. Sazonov, A.V., Bochkarev and E.P. Magomedbekov, The band structure of solid solutions of hydrogen isotopes in palladium at low temperatures, *Russian J. Phy. Chem. Z. Fizicheskoi Kimii* **78** (2004) 218–224.

[62] M.P. Pitt and E. M. Gray, Tetrahedral occupancy in the Pd–D system observed by in situ neutron powder diffraction, *EuroPhys. Lett.* **64** (2003) 344.

[63] D.K. Ross, V.E. Antonov, E.L. Bokhenkov, A.I. Kolesnikov, E.G. Ponyatovsky and J. Tomkinson, Strong anisotropy in the inelastic neutron scattering from PdH at high energy transfer, *Phy. Rev. B* **58** (1998) 2591.

J. Condensed Matter Nucl. Sci. 17 (2015) 91–95

Research Article

On the Path Leading To The Fleischmann–Pons Effect

Stanislaw Szpak*

3498 Conrad Ave, San Diego, CA 92117, USA

Abstract

Processes leading to the excess enthalpy production, the Fleischmann–Pons effect, are identified. The thermodynamic treatment [1] is extended to include self-organization. Discussion is limited to cells employing cathodes prepared by the co-deposition process.
 ISSN 2227-3123

Keywords: Plasma, Self-organization, Transmutation

1. Introduction

The Pd//D_2O,LiOD//Pt electrochemical cell, operating in the deuterium evolution substance producing mode generates more energy than it consumes, the Fleischmann–Pons (F–P) effect. This excess energy is attributed to nuclear reaction(s). When employing the F–P protocol, the nuclear activity starts several days after the completion of charging. It is assumed that within this time period the polarized Pd/D–D_2O system is put into such a state that when triggered by a stimulus, which may be either internal or external to the system, initiates the nuclear activity. At first there was no interest in the examination of the incubation period, even though events that occur within this time period are critical and may lead to better understanding of the nature of the F–P effect. An extension of Fleischmann et al. [1] thermodynamic treatment by including self-organization led me to believe that a satisfactory model of the pre-nuclear active state can be constructed.

2. Background Information

A brief summary of selected experimental work is presented to provide support for the interpretation of the conclusion derived from the thermodynamic considerations. The supporting material covers (i) the Pd+D co-deposition and (ii) localized heat sources (hot spots).

*E-mail: fgordon@san.rr.com

 ISSN 2227-3123

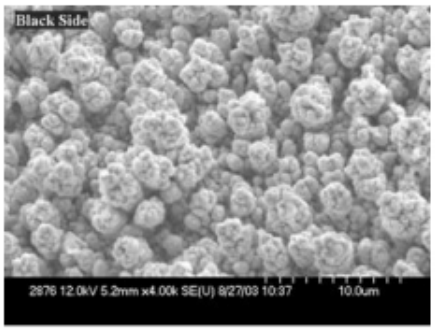

Figure 1. SEM of the Pd/D co-deposited material.

2.1. Co-deposition

One of the conditions for the occurrence of nuclear activity is the high D/Pd atomic ratio. The needed high D/Pd atomic ratio is assured if the working electrode is prepared by Pd+D co-deposition, a process in which the Pd^{2+} ions are electro-deposited in the presence of evolving deuterium. Electrodes prepared by co-deposition represent a convenient research tool because (i) they retain all features of "massive" electrodes, e.g. positive feedback and life-after-death [1], (ii) the D/Pd atomic ratios exceeding unity are obtained within seconds, (iii) the intensity of the F–P effect is higher and (v) if applied correctly then the reproducibility is 100% [2].

Figure 1 shows the structure of the Pd+D deposit employed in experimental work presented here. It is noted that the cell performance depends to a degree on the deposit morphology which, in turn, is governed by the the rates of the Pd^{2+} and D^{+}ions reduction.

2.2. Hot spots

Hot spots represent fast reactions which release thermal energy in very short time. That is to say, they resemble mini-explosions. Qualitatively, the localized heat sources lead to the following conclusions: (a) transition from non-reactive to reactive state occurs at discrete sites, (b) heat producing reactions are fast, (c) a large number of reacting particles is confined in a small volume. Quantitatively, the information derived from hot spots is as follows: (i) formation of domains having the volume of a sphere having radius of a few hundred Angstroms, in which 10^9 fast reactions occur [3], (ii) the energy released is on the order of 0.1 kJ/g and must have been occurred on at time scale of less than 10 ns involving milligrams of total mass [4].

3. Processes Leading to the F–P Effect

The content of the quote *"It should be entirely general line of attack in the study of all types of systems and processes to begin with a thermodynamic analysis and to exhaust the possibilities of thermodynamic reasoning before introducing models and assumptions of a mechanical or molecular nature."* [5] is most certainly applicable to the study of the nature of the F–P effect. It was this advice that led to the extension of the Fleischmann et al. [1] treatment by adding the concept of self-organization and including processes and/or reactions that are necessary in arriving at the identity of the pre-nuclear active state.

3.1. Self-organization

Fleischmann et al. [1] noted that nuclear reactions in a host lattice are affected by coherent processes and that ... *there are appropriate thermodynamic conditions for the formation of large clusters of hydrogen nuclei or of regions of the lattice containing ordered arrays of hydrogen nuclei at high H/Pd ratios*, resulting in the ... *formation of clusters of deuterons dispersed in the palladium lattice that would lead to the formation of ordered domains having high D/Pd ratios*. The appropriate conditions can be expressed in terms of self-organization which means that that there exists a volume of element within the system having dimensions much larger than the characteristic molecular dimensions but smaller than the total volume of the system. Within this volume fluctuations behave coherently thus modifying its microscopic behavior. At far from equilibrium, new structures, involving coherent behavior are formed and can be maintained only through a sufficient flow of energy [6].

An operating Pd/D//D_2O LiCl//Pt represents a system that satisfies the conditions necessary for self-organization, namely (i) system not in equilibrium, (ii) energy flow is assured, (iii) volume element is identified (hot spot). It is the volume element, located in the reaction space, where coherent processes take place and where the number of participating species can be estimated.

3.2. Charge transfer kinetics

Regardless of the cathode structure, (solid or Pd+D co-deposited), when the Pd//D_2O, LiCl//Pt cell operates in its substance producing mode, the cathode charge transfer reaction is

$$D_2\ O + e^- \rightarrow D_{ads} + OD^- \tag{1}$$

followed by deuterium absorption

$$D_{ads} \rightarrow D_{lattice}. \tag{2}$$

As written, Eq. (1) represents unbounded particles. But in the real world, particles interact with environment which, in turn, leads to identification of a number of statements that are relevant to the understanding the F–P effect. Using thermodynamic arguments, Fleischmann [7] concluded that:

(i) The expression $\Delta(\Phi_m - \Phi_s)F$ is responsible for (a) compression of D^+ into the lattice, (b) formation of clusters of D^+ which will be initiated at special sites, e.g. possibly at octahedral sites which would distort so that these sites would then be described as as parts of dislocation loops.
(ii) $D^+_{lattice}$ is viewed as an high density, low ion temperature plasma existing in an high electron concentration.
(iii) Electron density in the clusters is highly asymmetric.

3.3. Effect of D_2 evolution–production of defects

On smooth surfaces, in the absence of gas evolution, the charge transfer current density is uniformly distributed throughout the electrode surface. The evolving gas changes the cell current distribution from uniform to localized. The development of localized high current density is illustrated using Vogt's model [8] and shown in Fig. 2. In this model, at a distance from the charge transfer surface, the cell current is uni-directional. Close to the surface there is a stagnant layer of gas bubbles of various sizes and "empty" spaces arising from coalescence and growth of gas bubbles. This, in turn, changes the uni-directional current to the multi-dimensional high current density at the "empty" sites and causes the development of stresses which generate vacancies and other lattice defects.

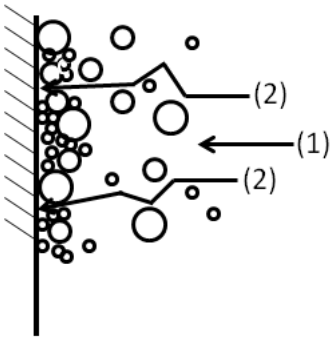

Figure 2. Effect of gas evolution on cell current distribution.

Dislocation loops and other lattice defects, e.g. vacancies, are generated by the action of the evolving deuterium. If dislocation loops can be created at will, then it would be possible to control the cell output.

4. The Path to the Pre-nuclear Active State, the π State

The path leading to the pre-nuclear active state, the π state, involves the following logically connected processes: (i) deuterium gas evolution which causes development of lattice defects (energy required 1–2 eV), (ii) lattice defects attract (draw in) deuterons and electrons (open volume effect), (iii) merging of lattice defects forms domains having high D/Pd atomic ratios (containing plasma). Incidentally, because of the porous structure of the co-deposited Pd/D deposits, cf. Fig. 1, the number of lattice defects would be larger resulting in better performance.

Reiterating, the π state, arises from coherent processes occurring during the incubation period which, for the electrodes prepared by the co-deposition, is few seconds. No information defining the structure of the plasma, except of its asymmetric D^+/e^- ratios, is available The structureless plasma can be modified by placing the operating cell in a external magnetic field.

5. Cell in an External Magnetic Field

Placement of an operating cell in an external magnetic field results in (a) change of the structure of the Pd/D deposit. Figure 3 shows the shape change of the co-deposited film. Evidently, when placed in an external magnetic field, the globules (cf. Fig. 1) are replaced by "pancake-like" structures.

The EDX analysis of selected flattened globules, Fig. 3a, shows the transmutation to new elements, namely Fe, Cr and Al. It is noteworthy that the same new elements were found in two separate runs, Figs 3a and b. Moreover, as illustrated in Fig. 3b, the EDX analysis of two closely placed flattened globules shows that they are identical.

The act of transmutation provides some insight into the nature and composition of the π state. Taking as the starting point the sequence of events which symbolically can be written

$$(!) + \pi - \pi^* \rightarrow \alpha \rightarrow X, \tag{3}$$

where (!) is the triggering mode, π^* is the compressed π state, $\alpha = X^* - [\alpha^{2+}, p^+, \gamma-, X-]$ denotes the nuclear active state and X is the stable element. For the proposed transmutation path to be realistic, two conditions must be

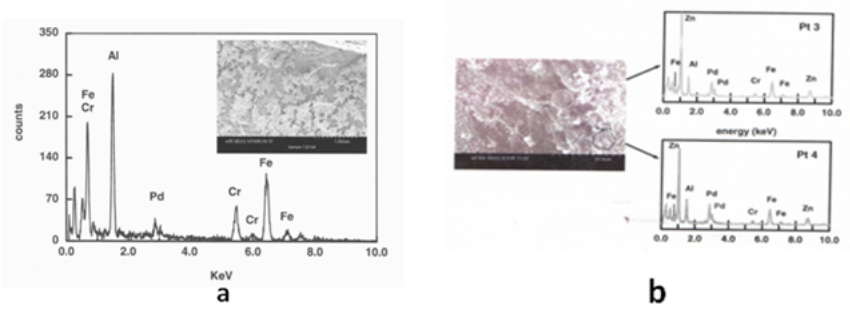

Figure 3. Selected examples of transmutation in an external magnetic field.

met: (i) the density of the molecular structure must be close or equal to the density of a nuclear substance and (ii) the dense state, the $\pi - \pi^*$ transition, must be created instantly, e.g. by either molecular collapse or a fast chain reaction.

6. Concluding Remarks

The formation of the π^* state is due to a complex interaction of kinetic and thermodynamic quantities. The formation of new structures is always the result of an instability which may be due to either internal or external fluctuations to the system, These fluctuations are always followed by the response which may bring the system to its original conditions or may produce a new structure.

The path leading to the formation of the π^* state is based on thermodynamic reasoning and supported by empirical data. Transmutation to three stable elements seem to indicate that in the presence of magnetic field, definite structure may be formed within the compressed plasma.

The nature of the "ignition" of the nuclear event is still unclear. The short-lived, randomly distributed in time and space hot spots favor the internal fluctuations as the source of process(es) leading to the ignition. This observation was taken as the starting point in the mechanism proposed by Dr F. Gordon, namely that the Pd lattice, distorted by dense plasma, responds non-linearly to internal fluctuations thus leading to localized energy spikes [9].

References

[1] M. Fleischmann, S. Pons and G. Preparata, *Il Nuovo Cim.* **107A** (2004) 143.
[2] S. Szpak, *J. Cond. Matter* **14** (2014) 68.
[3] S.R. Chubb, private communication, 2004.
[4] L. Wood, private communication (letter to F. Gordon, October 2000).
[5] P. van Rysselberghe, The thermodynamic structure of electrochemistry, *Modern Aspects of Electrochemistry*, Plenum Press, 1966.
[6] G. Nicolis and I. Prigogine, *Self-Organization in Non-Equilibrium Systems*, Wiley, New York, 1977, ISBN 0-471-02401-5.
[7] M. Fleischmann, An overview of cold fusion phenomena, in ICCF-1.
[8] H. Vogt, Electrochim Acta, **26** (1981) 1311.
[9] F. Gordon, private communication, 2015.

J. Condensed Matter Nucl. Sci. 17 (2015) 96–110

Research Article

Cold Nuclear Fusion in Metal Environment

E.N. Tsyganov*
Cold Fusion Power International, USA

M.D. Bavizhev
LLC "Radium", Moscow, Russian Federation

M.G. Buryakov, V.M. Golovatyuk and S.P. Lobastov
Joint Institute for Nuclear Research (JINR), Dubna, Russian Federation

S.B. Dabagov
P.N. Lebedev Physical Institute of the Russian Academy of Sciences, National Research Nuclear University "MEPhI", Moscow, Russian Federation

Abstract

This paper discusses the mechanism of cold fusion with deuterium and other elements implanted in the potential sites of conductive crystals. Cold fusion in metals becomes possible due to the fact that the implantation of atoms in a crystal guides them to their p excitation levels, which are determined primarily by the positioning of free conduction electrons in a zone of potential sites. The excitation energy of the p-states is about 10–14 eV. The excited atoms' orientation in the crystal is not random but dictated by the crystal lattice's electrostatic potentials. Calculations show that the transparency of the Coulomb potential barrier, for example, in the case of DD-fusion, increases by about 60 orders of magnitude if two deuterium atoms meet each other in the minima of the conductor's potentials in the *crisscross* orientation. Most of the papers are devoted to the process of DD-fusion in the electrolytic saturation by deuterium in crystals, a process that is extensively studied in these experiments. This paper also briefly comments on other experimental results related to cold fusion.
 ISSN 2227-3123

Keywords: Deuterium, Excess power, Nickel, Palladium, Platinum

1. Introduction

There has been talk about the transition to controlled thermonuclear fusion for over 60 years. However, despite the initial expectation that the problem would soon be solved, a solution has not materialized yet. Technical difficulties

*E-mail: edward.tsyganov@coldfusion-power.com

 ISSN 2227-3123

related to obtaining sustainable superhot plasma ($\sim 10^{9\circ}$C) and the damaging effects of the enormous neutron flux arising as a result of thermonuclear reactions have pushed the solution of this problem to the distant and uncertain future.

Fleischmann and Pons reported [1] an experimental result in which significant heat was observed in the electrolytic saturation of palladium crystal deuterium; this heat could not be quantitatively explained by chemical reactions. The authors concluded in these experiments that they were detecting nuclear DD-fusion occurring at room temperature. The orthodox physics community quickly decided that these experiments must be incorrect. However, after numerous subsequent confirmations, scientists appeared confident that the problem of controlled nuclear fusion had been solved. The most serious studies have been conducted by a group led by McKubre [2]. Nevertheless, the results of cold fusion experiments carried out in the past 25 years have either been completely ignored or met with great skepticism by the orthodox community of nuclear physicists. The two main objections put forward against the results of these experiments are as follows.

(1) Numerous attempts have been unsuccessful in providing a scientific explanation for how, in the process of cold fusion, the so-called Coulomb barrier is overcome.
(2) In DD cold nuclear fusion, in contrast to thermonuclear fusion, there are practically no other nuclear products except ^{4}He. This phenomenon has no clear explanation.

In the following sections, we have tried to answer these objections.

The heat release in cold fusion reactions is about 10^6 times greater than in any chemical reaction. Thus, we have discovered a new physical phenomenon that will undoubtedly change the whole course of human civilization. Some of the practical applications of this phenomenon (for ships, aircraft, and spacecraft) are simply not available for large cyclopean tokamaks or other hypothetical systems using conventional nuclear fusion.

2. Experiments on DD Fusion using Low-energy Accelerators

It has been shown in experiments with DD fusion accelerators that if the deuterium atom target is located in a conducting crystal, the fusion reaction at low energies is much more probable than in the case of free deuterium atoms. These experiments provide a direct explanation of the phenomenon of cold fusion.

Describing the collisions of atoms, one must properly modify the expression of the probability of penetration through the potential barrier, written for the collision of "naked" nuclei, because atomic electrons screen the repulsive effect of nucleic charges. Within the Born–Oppenheimer approximation, Assenbaum [3] and others have shown that introducing the so-called "electron screening potential" for a collision of free atoms is equivalent to introducing in expression of the transparency for the Coulomb barrier $P = \mathrm{e}^{2\pi\eta}$, where $2\pi\eta = 31.41/E_{\mathrm{eff}}^{1/2}$, $E_{\mathrm{eff}} = E + U_{\mathrm{e}}$, an additional energy $U_{\mathrm{e}} = 27$ eV. In experiments at accelerators [4–13], the electron screening potential reaction of DD fusion in conducting crystals suddenly appeared to be very large – equal to $U_{\mathrm{e}} \sim 300 - 700$ eV. Figure 1 shows the results of astrophysical function $S(E)$ from [11] for the case in which target deuterium atoms are embedded into the platinum crystal. Instead of approaching a value of about 50 keV-b with decreasing incident deuteron energy, as happens when deuterium targets are embedded in a substrate of semiconductors, insulators, or amorphous materials, the value of $S(E)$ begins to increase sharply.

The presence of the crystal's conduction electrons, grouped in the conductor lattice's potential sites, results in a ban for the hydrogen atoms' s states to occupy these sites. The excitation of a hydrogen atom's electron shell by only 10 eV translates to a deuterium atom in the state 2p, 3p, etc. and effectively removes the ban. This means that if one crystalline site in a conductive crystal contains two deuterium atoms, the distance between these atoms' nuclei is equal to 1/10–1/20 of the nominal sizes of unexcited atoms. This drastically increases the probability of a fusion reaction.

We considered the processes of cold DD fusion in Refs. [14–18].

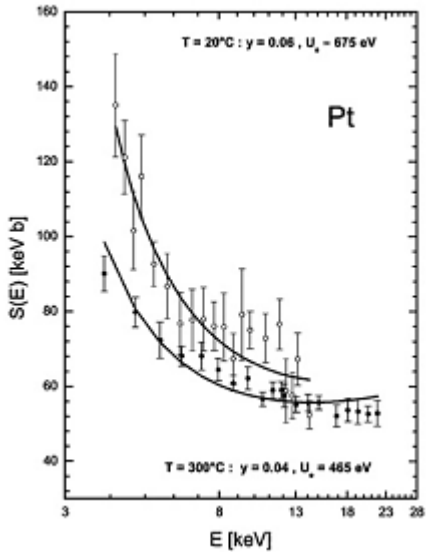

Figure 1. The astrophysical function value $S(E)$ in the case in which the target deuterium atoms are imbedded into the platinum crystal. At room temperature, the data fit well with the screening potential of 675 eV.

3. Physics of Cold DD Fusion

A diagram of a hydrogen atom's electron levels is shown schematically in Table 1.

Table 1. Scheme of a hydrogen atom's electronic excitation levels.

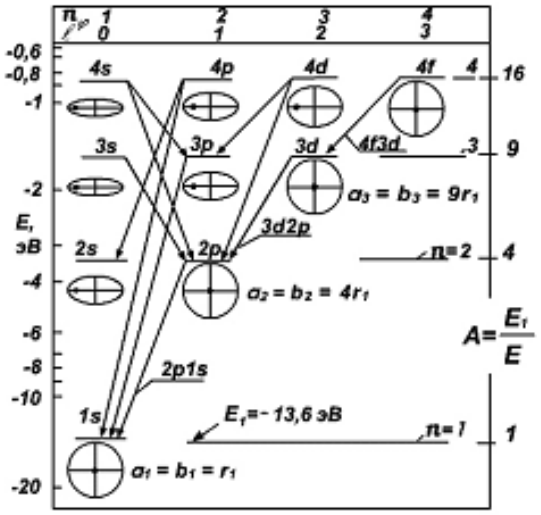

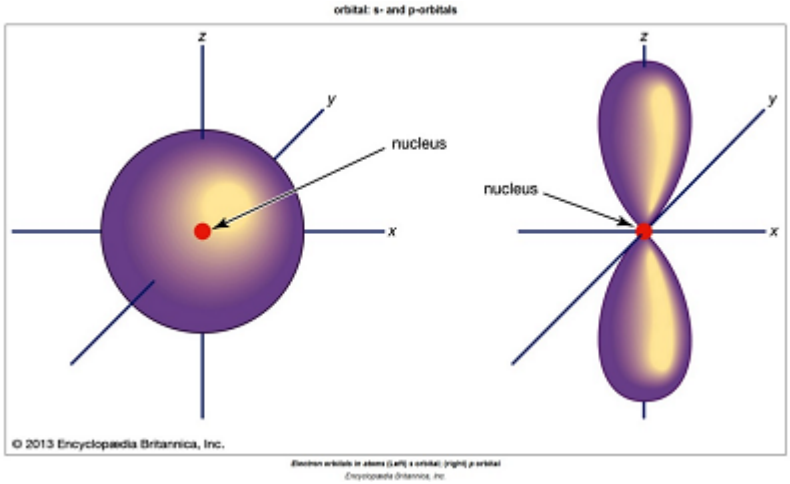

Figure 2. The hydrogen atom orbitals 1s (left) and 2p (right). This figure is taken from the Encyclopædia Britannica, 2013 [19]. The presented contours include 95% of the electron's possible positions.

We are interested in the second vertical column with the quantum numbers $n = 2$ and $l = 1$, and in particular, the levels 2p and 3p. Figure 2 [19] schematically illustrates the free hydrogen atom's electron density in the states 1s and 2p.

Winter [20] has developed an interesting representation of the free hydrogen atom's various orbitals. Figure 3 shows the function of hydrogen's electron density by the solution of the Schrödinger equation in the states 2p and 3p. Figure 4 shows the fcc crystal structure, of nickel, palladium, and platinum. Large circles indicate the atoms' location in the host crystal; small circles indicate the location of the deepest octahedral potential sites in the structure. The parameters of all octahedral sites are identical.

When the ratio of impurity atoms and deuterium atoms in a host crystal does not exceed the ratio of D/Pd ~ 0.9, the cold fusion process does not occur, as deuterium's impurity atoms are located in different octahedral sites and are quite distant from each other. However, when one such potential site has two deuterium atoms in an electron excitation state of 2p or above, the probability of penetration through the potential barrier of DD fusion increases sharply.

One of the cold fusion skeptics' most convincing arguments relates to these experiments' lack of nuclear decay products in the resulting compound nucleus. It was believed that "no neutrons – no fusion." However, a large international team of physicists, currently totaling about 200–300 people, continues to work in this direction. These researchers have considerable experience in cold fusion. The leading group of physicists working in this direction is led by M. McKubre [2]. Figure 5 shows a graph of excess heat (in watts), depending on the current, from these electrochemical experiments [21].

McKubre et al. [22] have demonstrated the success of cold fusion experiments in the *yes–no* embodiment vs. deuterium concentration in the palladium crystal (Fig. 6). After exceeding the ratio of D/Pd $\sim$ 0.9, experimenters

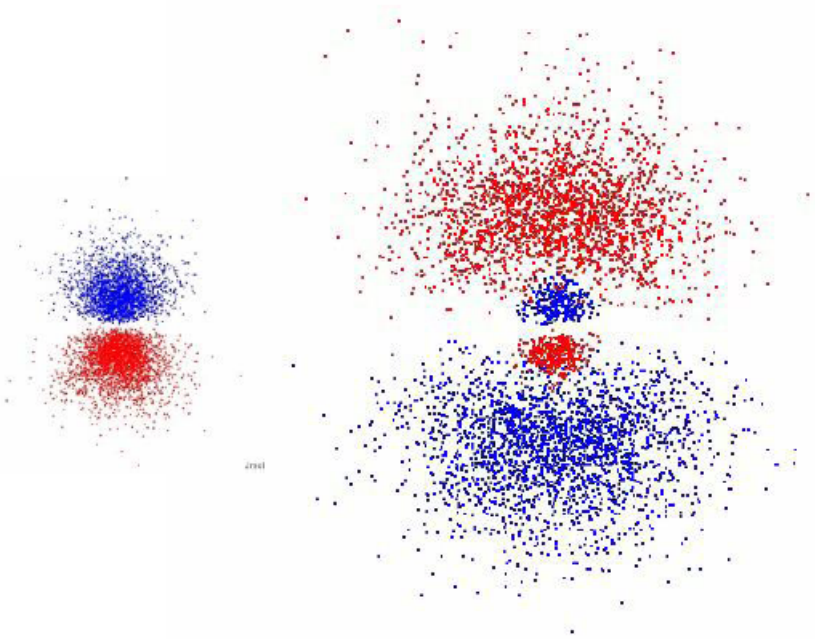

Figure 3. The functions of hydrogen's electron density in the states 2p (left) and 3p (right), from Winter [20]. Red and blue mark the density obtained for the positive and negative values, respectively, of the wave function ψ.

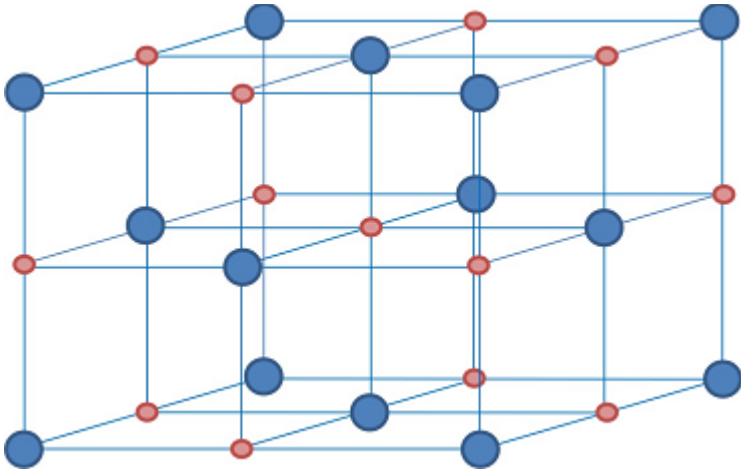

Figure 4. The crystalline structure of fcc (nickel, palladium, platinum). Small circles indicate the locations of the structure's deepest octahedral potential sites.

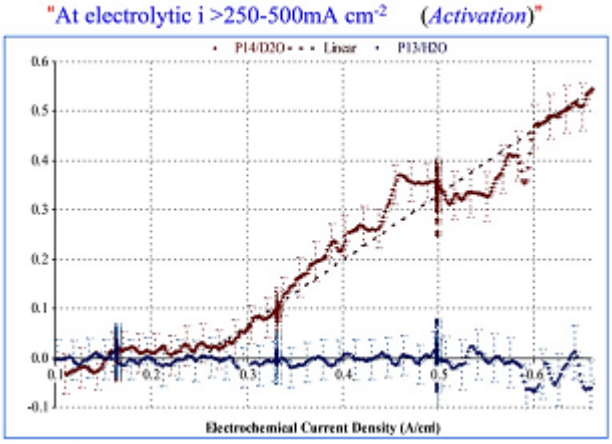

Figure 5. Excess heat (in watts) depending on electrochemical current in the experiments of McKubre et al. [21].

consistently observe DD fusion. In [16], we calculated the electric field in the volume of fcc crystals. Figure 7 shows the shape of the octahedral potential site in a platinum crystal.

The left-hand side portion of Fig. 8 shows the *XY* projection for the empty octahedral site. The center of the figure shows a possible arrangement of a single deuterium atom in the 2p state in this site. The right-hand side of the figure shows a possible combination of two such atoms in the same site. The color scale characterizes the electric field's potential in the cell of the crystal of platinum. The reader should keep in mind that there are some zero quantum vibrations of 2p deuterium atoms; this, however, does not deny their average location in the conductive crystal cell.

Figure 9 shows the arrangement of two deuterium atoms in the 2p state in one crystallographic site along the vertical axis Z. Figure 10 schematically illustrates the mechanism of a deuterium atom transition to the 2p state during its implantation in a conductive crystal. Thus, the target deuterium atoms implanted into metals are no longer in the base 1s state, as the cloud of free electrons in the atom causes the implanted atom's electrons to take excited p states.

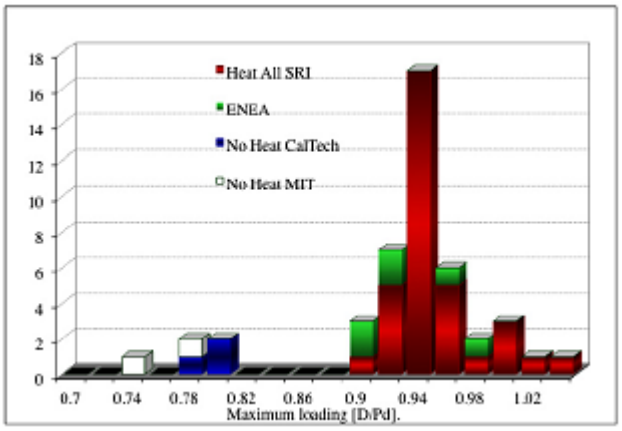

Figure 6. The success of cold fusion experiments, depending on the concentration of deuterium in the palladium crystal, from [22].

Table 2. Characteristics of cold fusion for palladium and platinum.

Crystal type	Screening potential (eV)	Oscillation frequency (ν, s^{-1})	Transparency ($e^{-2\pi\eta}$)	Reaction rate (λ, s^{-1})
Palladium	300	0.74×10^{17}	1.29×10^{-25}	0.95×10^{-8}
Platinum	675	1.67×10^{17}	2.52×10^{-17}	4.2

The screening potential of 300–700 eV in experiments on DD fusion at accelerators shows that incident deuterium atoms are also in the p states during their movement in a conducting crystal. These processes allow for the two deuterium nuclei in the crystal potential site cell to be close enough without feeling a strong Coulomb repulsion.

Figure 11 presents the sizes of different hydrogen orbitals, in particular 2p and 3p [23]. Note again, Figs. 2, 3, 9 and 11 are valid exactly only for separated atoms, and could be distorted during chemical bonding. We used them here as the first approximations. Figure 12 shows the Coulomb barrier transparency of the potential electron screening U_e for DD cold fusion.

$$P = e^{-2\pi\eta}(2\pi\eta = 31.41/E_{\text{eff}}^{1/2}, E_{\text{eff}} = E + U_e).$$

For cold fusion ($E \cong 0.040$ eV), the ratio of the deuterium atoms' Coulomb barrier transparency in the same crystal platinum site to the corresponding value for the transparency of the free deuterium molecule is $Pt/D_2 \cong 10^{65}$. Thus, the metal crystal penetration of deuterium nuclei through the Coulomb barrier becomes practically possible due to the system's zero quantum vibration of the system. Table 2 (taken from [15]) shows the characteristics of cold DD fusion for palladium and platinum crystals.

The pioneering work of Arata [24] was very fruitful; the detailed experiments of Swartz and Hagelstein [25] should be also mentioned here. Unfortunately, the brevity of this review does not allow further detail on these studies.

Below, we will show that the relaxation of the excited compound nucleus ^{4}He* can be successfully explained by the exchange of this object with the crystal environment through the so-called *virtual photons*. This process has remained an intriguing mystery over the last 25 years.

4. The Discharge of ^{4}He* Excess Energy by Virtual Photons

We have shown that the presence of free electrons in these crystals' saturated metal causes deuterium atoms to firmly occupy 2p orbitals or higher. When all octahedral sites are already filled with such deuterium atoms, sites with more than one such atom begin to appear. In this case, the probability that the DD system will penetrate the potential barrier increases dramatically. As we noted above, the rate of DD fusion in platinum crystals in such a site may reach 4 s^{-1}.

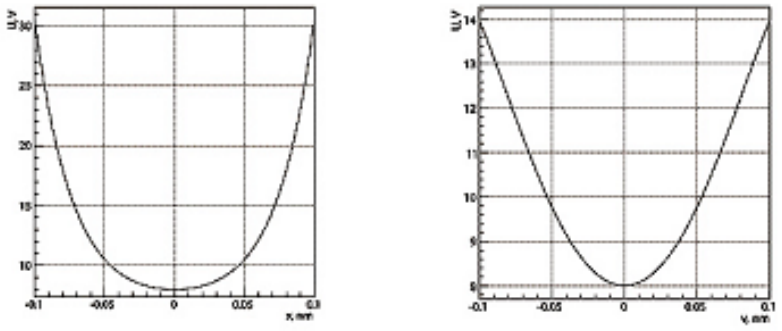

Figure 7. Electric potential behavior in the vicinity of an octahedral potential site in platinum crystal. The potential (in volts) at $Z = 0$ is shown in the crystal cell's horizontal plane (left) and diagonal plane (right).

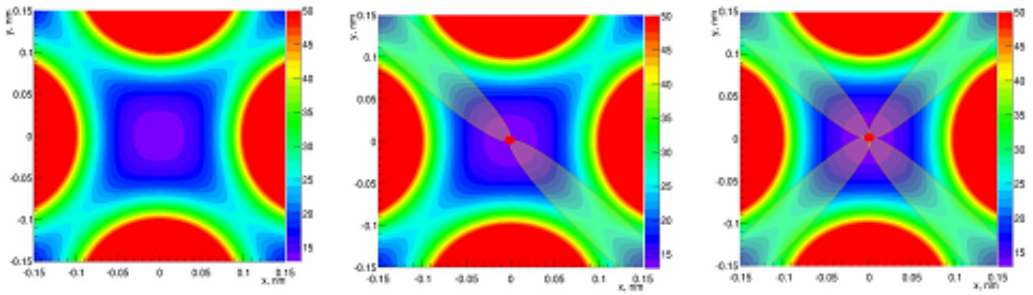

Figure 8. Left: the potential distribution in the empty octahedral site in the *XY* projection; center: a possible location of a single deuterium atom in the 2p state in this site; right: a possible combination of two such atoms in the same site. The color scale represents the electric field potentials in the platinum crystal cell.

Due to the very small (thermal) excitation energy of the compound nucleus reaction DD$\rightarrow{}^4$He*, the compound nucleus's orbital angular momentum equals zero, which eliminates the possibility of real gamma ray emission. Figure 13 shows the potential well of strong interactions for the reaction DD$\rightarrow{}^4$He*. Deuterons that have already penetrated into the potential well are still separated by the residual Coulomb barrier, the value of which, apparently, can reach hundreds of electron-volts. The nuclear decay rate of the compound nucleus ^{4}He*, by the standard nuclear decay channels ^{3}H+p and ^{3}He+n, is significantly decreased. In this case, the exchange by the virtual photons with the external environment is still possible, as the spin of the virtual photons can be *directed along the time axis*. This residual Coulomb barrier acting between deuterium nuclei already in the potential well of the strong interactions can significantly slow down the rate of conventional nuclear decay channels.

In accordance with Fig. 13, we assume that the deuteron's penetration rate through the residual Coulomb barrier in the strong interactions' potential well is much less than $10^{-15}\mathrm{s}^{-1}$ because of the very small (thermal) excitation energy of ^{4}He*. During this time, the excess energy of the excited nucleus ^{4}He* is completely entrained into the environment.

Figure 14 shows the energy transfer of the excited ^{4}He* state to surrounding electrons in the conducting crystal by virtual photons. In order for this mechanism to work, the ^{4}He* metastable state must exist.

It can be assumed that after the fusion, the Coulomb barrier acts inside the strong interactions' potential well, and neutrons no longer have a retention factor, so they can almost freely move from one proton to another. However, the fact that this reaction is "almost free," not "completely free," means that extra energy of about 2 MeV is needed for

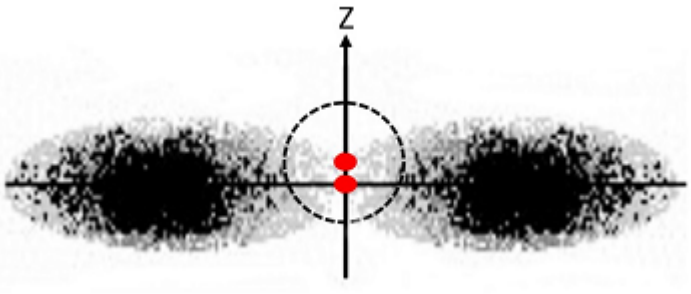

Figure 9. Location of two deuterium atoms in the 2p state in the same crystallographic site along vertical axis Z.

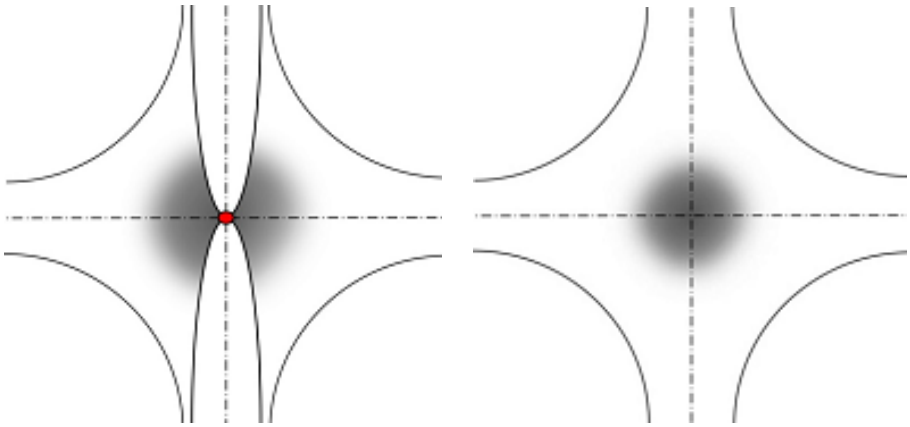

Figure 10. The conducting crystalline cell. A simple cubic structure is used as a didactic example. The shaded area shows the free electrons' location. The crystal's free conduction electrons do not completely leave their positions; as a result of this compromise process, a deuterium atom transits from the 1s state to the 2p state.

this process. Recall that in this case the kinetic energy of the deuterons in the strong interactions' potential well is very small, much less than 1 eV. The left-hand side of Fig. 15 shows Feynman's representation of a hydrogen atom. The right-hand side shows virtual photons carrying away the excess excitation energy in the reaction DD→^{4}He*, as it could have been represented by Feynman.

Figure 16 illustrates the process of transferring the electron energy to the environment. Figure 17 demonstrates changes of the compound ^{4}He* nucleus during transition to the ground state ^{4}He. The spatial separation of two deuterons in the intermediate nucleus ^{4}He* produced in cold fusion must be large enough to ensure that the deuterons' residual Coulomb repulsion significantly delays the discharge ^{4}He*→^{4}He with virtual photons. This is dictated by the distance between the intermediate nucleus and the nearest electrons in the crystal lattice.

5. Design of the Experiment

A calorimetric approach does not allow us to understand in detail the specific mechanism of DD cold fusion. A special experiment is needed to shed light on the energy transfer mechanism in DD fusion without nuclear decay. We have

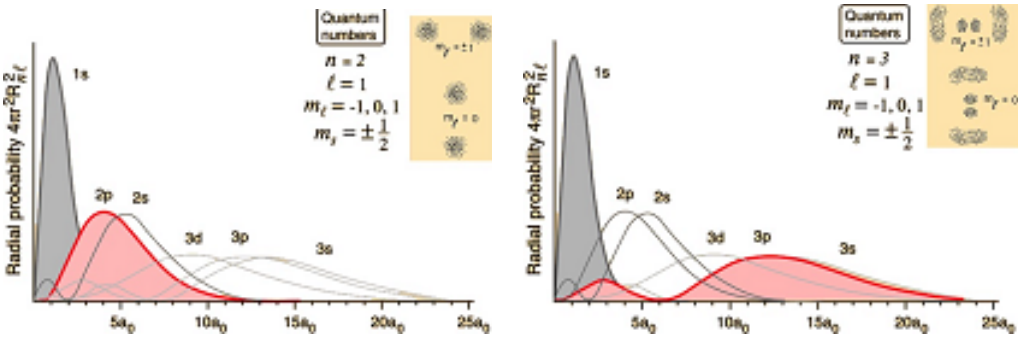

Figure 11. Radial probability for 2p and 3p states.

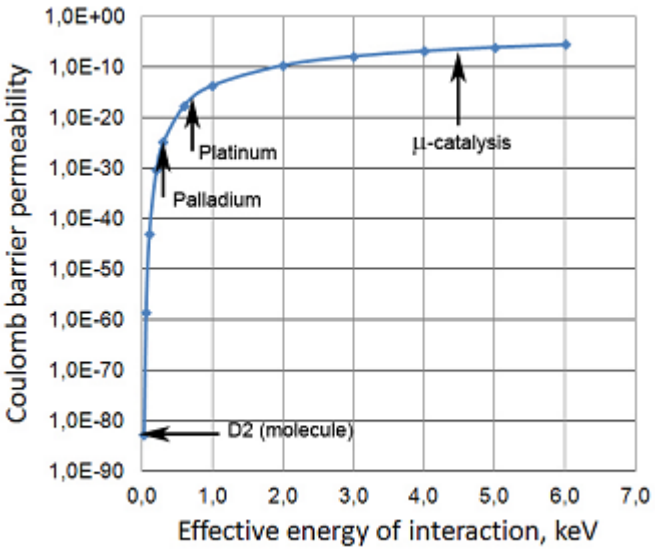

Figure 12. Coulomb barrier transparency for $E = 0$ in the potential U_e electron screening process of DD cold fusion.

formulated such proposals in Ref. [16]. As noted above, the effect of conduction electrons and the lattice of metallic crystals (suppression of 1s orbitals, excitation of 2p orbitals and these orbitals' definite spatial orientation in a crystal lattice) can significantly change the Coulomb potential barrier. The effective screening distance in this case could be an order of magnitude less than for non-excited atoms.

We calculated the *process using the energy of the individual emission electron* of 60 keV. In Fig. 18, we show the experiment's geometry, which would allow us to obtain additional information on cold DD fusion in conductive crystals.

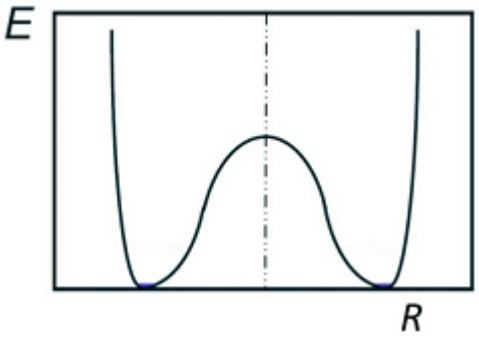

Figure 13. Schematic representation of the bottom of the potential well of the strong interactions for cold DD fusion in conductive crystals. The thermal excitation energy of ^{4}He* is about 0.040 eV.

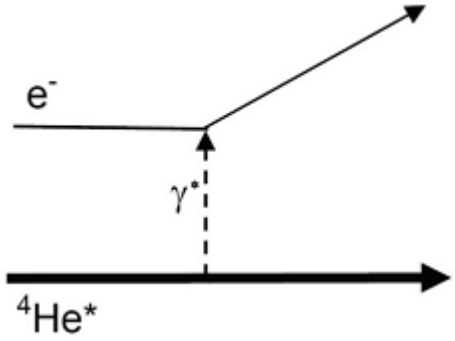

Figure 14. Scheme of excess energy discharge of the intermediate nucleus ^{4}He* by a series of successive virtual photon exchanges between the nucleus and the environment.

At the preliminary stage of the experiment, we plan to measure the total energy of the electrons emitted from only one side of the palladium crystal. Sixteen semiconductor silicon detectors were placed on one side of the palladium crystal and included in the *coincidences*.

Total detected energy was calculated using a Monte-Carlo simulation (Geant4). For a detailed simulation of low-energy electromagnetic interactions [26], we used the Livermore Physics model (G4EmLivermorePhysics) of the GEANT4 package. We used the database and Livermore EPDL and EEDL.

It was assumed that, as a result of the fusion process occurring in a relatively short time (about 10^{-15} s), approximately 10^3 electrons enter into the detector with the energy of 60 keV; the total released energy is 24 MeV. Palladium foil is not an active element; this means that part of the electrons' energy resulting from the DD fusion is fading from the measurement. Calculations allowed the optimization of palladium foil thickness and detector geometry.

Figure 19 shows the results of calculations for the one-sided detector arrangement and the radiation of electrons with energy of 60 keV. Event selection can be done by triggering multiple detector coincidences on one side of the palladium foil.

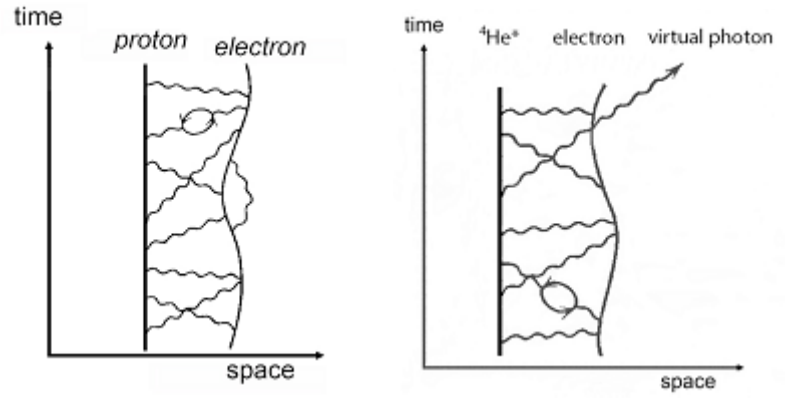

Figure 15. Left: Feynman's diagram of a hydrogen atom's steady state. Right: the virtual photons of the excited state ^{4}He* in DD cold fusion, as they could have been represented by Feynman.

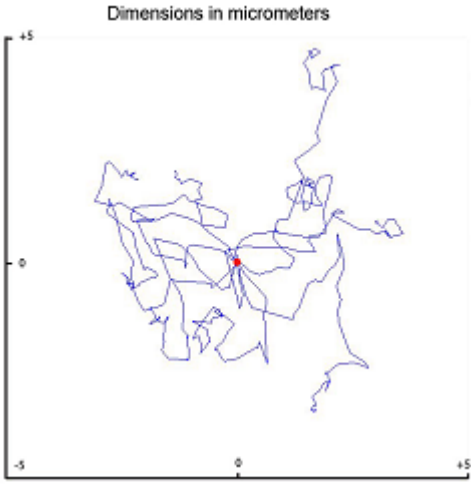

Figure 16. The trajectories of the first 10 electrons, generated to describe the cold DD fusion process in palladium using the Monte Carlo method [16]. Dimensions are in micrometers.

About 75% of the Monte-Carlo events were completely absorbed in the sample palladium. The resulting energy spectrum extends to about 14 MeV, which is explained by the backscattering of electrons in palladium fraction at angles up to 180°.

In the case when the detectors are located on one side of the Palladium, the maximum detected energy is about half of the decay energy of ^{4}He*. In our view, these measurements are conclusive evidence that excitation energy is transferred from the compound nucleus ^{4}He* to the host crystal by means of virtual photons.

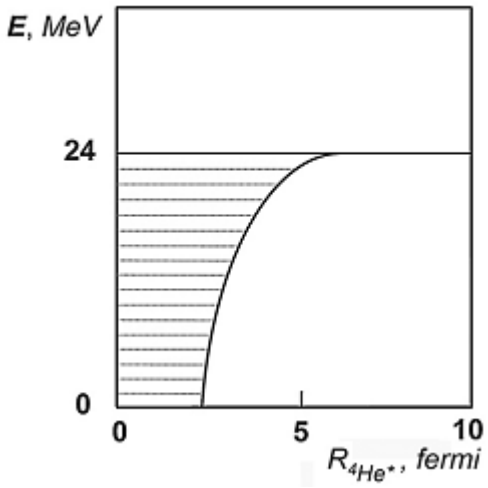

Figure 17. The size of the intermediate compound nucleus ^{4}He* during discharge of the excited nucleus's excessive binding energy. The horizontal scale is quite conditional.

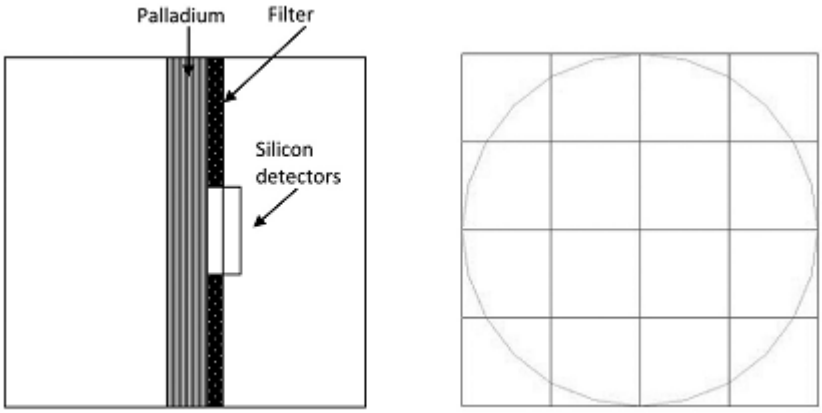

Figure 18. One-sided experimental scheme. Several silicon semiconductor detectors are located on one side of the palladium crystal and included in the coincidences. The left-hand side shows the detector; the right-hand side shows the mutual arrangement of the holes in the filter and the detectors.

6. Discussion

The scientific community's adaptation of new knowledge has never been easy. The current paradigm in nuclear physics does not support such effects as cold fusion even though this phenomenon does not contradict the fundamental laws of nature. This is complicated by the fact that attempts to find a solution to controlled thermonuclear fusion, which have taken place for more than half a century, have gone too far.

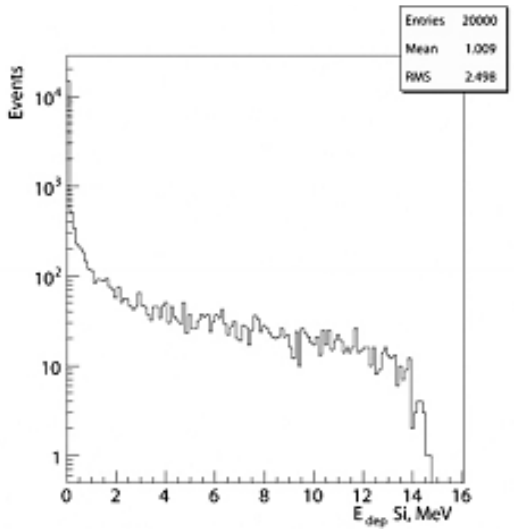

Figure 19. The total energy of the emitted electrons with energies up to 60 keV in the detectors located on one side of palladium. The thickness of the palladium foil was set at 20 μm.

The most advanced attempt in this direction is the international project ITER – Tokamak. Currently, the project, which is in the construction stage, is enormous and extremely expensive. Realists estimate that construction of the reactor and the possible start-up will be completed no earlier than 35–50 years from now. This project is considered as pure research, and if it can work, it will only do so in a cyclic mode. After its launch, the construction of an even more gargantuan structure – Industrial Tokamak DEMO – is planned. Huge financial and material costs will continue for another half-century.

The global fuel and oil–gas industries welcome these projects. Such a development could lead to climate change, the reduction of the global population, and other social cataclysms.

Cold fusion is a viable alternative to this tragic scenario. We believe that, in the coming years, there will be public recognition of cold fusion and that this research will cause radical changes in the practical applications of nuclear research.

Acknowledgements

One of the authors (E.T.) thanks Dr. A.G. Parkhomov for discussion.

References

[1] M. Fleischmann, S. Pons and M. Hawkins, *J. Electroanal. Chem.* **201** (1989) 301.
[2] M.C.H. McKubre, F. Tanzella, P. Tripodi et al., in: F. Scaramuzzi (Ed.), *Proc. of the 8th Int. Conf. on Cold Fusion*, Lerici (La Spezia), Italian Physical Society, Bologna, Italy, 2001, p. 3; M.C.H. McKubre, Condensed Matter Nuclear Science, in *Proc. of the 10th Int. Conf. on Cold Fusion*, P.L. Hagelstein and S.R. Chubb (Eds.), Cambridge, MA, USA, 21–29 August, 2003, World Scientific, Singapore, 2006. Michael C. H. McKubre and Francis L. Tanzella, Cold Fusion, LENR, CMNS, FPE: One Perspective on the State of the Science Based on Measurements Made at SRI, *J. Condensed Matter Nucl. Sci.* **4** (2011) 32–44.
[3] H.J. Assenbaum, K. Langanke and C. Rolfs, *Z. Phys. A – Atomic Nuclei* **327** (1987) 461–468.
[4] H. Yuki, T. Satoh, T. Ohtsuki, T. Yorita, Y. Aoki, H. Yamazaki and J. Kasagi, D+D reaction in metal at bombarding energies below 5 keV, *J. Phys. G: Nucl. Part. Phys.* **23** (1997) 1459–1464.
[5] J. Kasagi, H. Yuki, T. Itoh, N. Kasajima, T. Ohtsuki and A. G. Lipson*, Anomalously enhanced d(d,p)t reaction in Pd and PdO observed at very low bombarding energies, *the Seventh Int. Conf. on Cold Fusion*, Vancouver, Canada, ENECO Inc., Salt Lake City, UT, 1998, p. 180.
[6] H. Yuki, J. Kasagi, A.G. Lipson, T. Ohtsuki, T. Baba, T. Noda, B.F. Lyakhov and N. Asami, Anomalous enhancement of DD reaction in Pd and Au/Pd/PdO heterostructure targets under a low energy deuteron bombardment, *JETP Let.* **68**(11) (1998) 10 December.
[7] J. Kasagi, H. Yuki, T. Baba and T. Noda, Low energy nuclear fusion reactions in solids, *8th Int. Conf. on Cold Fusion*, 2000, Lerici (La Spezia), Italy: Italian Physical Society, Bologna, Italy.
[8] A.G. Lipson, G.H. Miley, A.S. Roussetski, and A.B. Karabut, Strong enhancement of dd-reaction . . . , *ICCF-10*, 2003.
[9] C. Rolfs, Enhanced electron screening in metals: a plasma of the poor man, *Nucl. Phys. News* **16** (2) (2006).
[10] F. Raiola, (for the LUNA Collaboration), B. Burchard, Z. Fulop et al., *J. Phys. G: Nucl. Part. Phys.* **31** (2005) 114.
[11] F. Raiola, (for the LUNA Collaboration), B. Burchard, Z. Fulop et al., *Eur. Phys. J. A* **27** (2006) 79.
[12] A. Huke, K. Czerski, P. Heide, G. Ruprecht, N. Targosz and W. Zebrowski, *Phys. Rev. C* **78** (2008) 015803.
[13] K. Czerski, A. Huke, P. Heide et al., *J. Phys. G* **35** (2008) 014012.
[14] E.N. Tsyganov, Preprint LNF–11/03 (P), April 6, 2011.
[15] E.N. Tsyganov, *Yadernaya Fizika* **75**(2) (2012) 174–180 (in Russian); E.N. Tsyganov, *Phys. Atomic Nuclei* **75**(2) (2012) 153–159.
[16] E.N. Tsyganov, V. M. Golovatyuk, S. P. Lobastov, M. D. Bavizhev, S. B. Dabagov. Nuclear Instruments and Methods in Physics Research B. 2013. vol. 309, p. 95–104.
[17] E.N. Tsyganov, M.D. Bavizhev, V.M. Golovatyuk, S.B. Dabagov and S.P. Lobastov, *Eng. Phys.* **9** (2013) 3–17 (in Russian).
[18] E.N. Tsyganov, *Eng. Phys.* No. 6 (2014) 6–13.

[19] Encyclopædia Britannica, 2013.
[20] M.J. Winter, Department of Chemistry, The University Sheffield S3 7HF, UK, http://winter.group.shef.ac.uk/orbitron/
[21] C.H. Michael McKubre et al., *J. Condensed Matter Nucl. Sci.* **4** (2011) 32–44.
[22] C.H. Michael McKubre et al., *J. Condensed Matter Nucl. Sci.* **8** (2012) 187.
[23] Tutorial http://hyperphysics.phy-astr.gsu.edu/hbase/hydwf.html
[24] Y. Arata and Y. Zhang, The establishment of solid nuclear fusion reactor, *J. High Temp. Soc.* **34**(2) (2008) 85.
[25] M. Verner, G., M. Swartz and P. Hagelstein, Summary report: 'Introduction to Cold Fusion'–IAP course at the Massachusetts Institute of Technology, *Current Sci.* **108**(4) (2015) 653, http://www.currentscience.ac.in/Volumes/108/04/0653.pdf
[26] Recent Improvements in Geant4 Electromagnetic Physics Models and Interfaces. Joint International Conference on Supercomputing in Nuclear Applications and Monte Carlo 2010 (SNA and MC2010), Hitotsubashi Memorial Hall, Tokyo, Japan, October 17–21, 2010; G4EmLivermorePhysics Package.

J. Condensed Matter Nucl. Sci. 17 (2015) 111–115

Research Article

Silica Favours Bacterial Growth Similar to Carbon

N. Vasanthi* and S. Anthoni Raj

RomVijay Biootech Pvt. Ltd., Pondicherry 607402, India

Lilly M. Saleena

Department of Bio-informatics, SRM University, Kattangulathur 603403, India

Abstract

Silicate solubilising bacteria were isolated from soil, river water, pond sediment and talc mineral. The isolates were characterised and found to belong to the genera *Bacillus* and *Pseudomonas* sp. Some of the isolates are also identified by 16S r RNA sequencing. Both *Bacillus* and *Pseudomonas* isolates solubilised magnesium trisilicate under in vitro conditions either in the presence or in the absence of glucose. *Bacillus megaterium* isolated from soil solubilised talc, feldspar and magnesium trisilicate by releasing silica in solution. This also exhibited growth exclusively on silicate in the absence of a carbon source and after removal CO_2 in the head space of the flask containing medium. *Bacillus mucilaginosus*, a silicate solubilising species, exhibited growth on acid washed sand (pure quartz) and also in silicic acid in the absence of carbon source revealing the capability of the bacteria to utilise silica or silicate for its growth. The carbon analysis by SEM with EDAX revealed the presence of carbon in cells grown exclusively on silica suggesting the biological transmutation of silica to carbon. The ability of silicate solubilising bacteria to grow exclusively on silica or silicate in the absence of carbon reveals not only their ecological survival in a carbon-free environment in earth but also their likely survival in other celestial bodies.
 ISSN 2227-3123

Keywords: Biological transmutation, Ecological survival, Silicate mineral utilisation, Silicate solubilising bacteria

1. Introduction

Silicate solubilising bacteria (SSB) are of recent interest as they have been found to solubilise potassium and silica in the soil silicate minerals [1,2]. Silicon is accepted as agronomically a beneficial element for crop plants, which absorbs silicon in the form of *ortho* silicic acid only which is very low (0.1–0.6 mM) in soil solution [3]. It is surprising to see a larger accumulation of silicon in the form of silica in plants when its availability is very low in soil as the entire soil is made up of polymerized silicates that are insoluble in water. Hence the SSB is advocated to solubilise silica in situ in the soil. In an earlier study, SSB was found to grow on sand and in silica in the absence of a carbon source [4]. Therefore, the growth and silicate solubilisation potential of selective isolates were tested on certain silicate minerals

*E-mail: n.vasanthi@hotmail.com

 ISSN 2227-3123

Table 1. Solubilisation of silica (SiO_2 mg l^{-1}) from magnesium trisilicate by bacterial isolates in the presence and absence of carbon source*.

SSB isolates	Silicate medium without carbon DAI				Silicate medium with carbon DAI			
	0	5	10	15	0	5	10	15
Control	0.8	1.5	1.5	1.5	0.8	1.0	1.0	1.0
Bacillus flexus	0.8	5.1	3.5	0.3	0.8	4.0	1.1	1.4
Bacillus sp	0.8	3.5	7.9	8.2	0.8	4.0	1.6	0.2
Bacillus sp	0.8	6.6	8.7	7.9	0.8	6.9	1.2	1.7
Bacillus mucilaginosus	0.8	5.7	7.2	11.2	0.8	4.0	5.2	8.7
Pseudomonas sp	0.8	6.0	8.2	9.9	0.8	6.0	7.4	8.0

DAI–Days after inoculation; glucose @ 0.1%*.

either in the presence or in the absence of a carbon source. Since the dissolution was observed even in the absence of carbon, perhaps the CO_2 trapped in the head space air in the flask might have favoured growth. A detailed experiment is undertaken after eliminating CO_2, and the results are reported.

2. Materials and Methods

Basal medium (glucose 1.0 g; $(NH_4)_2$ SO_4 1.0 g; KCl 0.2 g; K_2HPO_4 0.1 g; $MgSO_4{\cdot}7H_2O$ 0.2 g; Distilled water 1l; pH 7.0) was prepared and dispensed in 100 ml quantities and insoluble magnesium trisilicate was added at 0.25% concentration. The flasks were sterilized, inoculated with a loopful of silicate solubilising isolates of *Bacillus* and *Pseudomonas*. A similar set of flasks containing basal medium devoid of glucose was similarly inoculated and the flasks were incubated at room temperature (30±2°C) for 2 weeks. At periodical intervals, the culture filtrate was centrifuged to remove the cells and debris and the dissolved silica content was determined in the supernatant as followed in the method of Imaizumi and Yoshida [5]. The ability of *Bacillus megaterium,* another silicate solubilising bacteria to solubilise different silicates is also tested in basal medium supplemented with talc, feldspar and magnesium trisilicate separately at 0.25% level. Since this bacterium solubilised all silicates and dissolution was investigated in magnesium trisilicate with 0.1% glucose and without glucose wherein the CO_2 was excluded by drawing air into the flask aseptically bubbled through alkali. The trace of CO_2 was trapped by suspending vials containing sterile alkali inside the flasks. In order to ascertain the utilization of pure silica by *Bacillus mucilaginosus,* the acid washed sand free from organic matter, were pulverised and sieved through BSS 44 and the precipitated silicic acid (Loba chemicals) were added separately at 0.25% level in the basal medium with and without glucose. The flasks were inoculated with a suspension of 0.1 ml *Bacillus mucilaginosus* (ca 300×10^8 cells/ml). The cell growth was found to be in the carbon containing silicate medium reduced after 7 days due to a low pH level. The cell grown exclusively in silica was subjected to SEM with EDAX (F E I Quanta FEG 200 - High Resolution Scanning Electron Microscope) to detect the carbon content.

Table 2. In vitro dissolution of silica (SiO_2 mg l^{-1}) from different silicate minerals by *Bacillus megatherium* in the presence and absence of carbon source.

Treatment	Silicate medium without carbon DAI			Silicate medium with carbon DAI		
	0	8	16	0	8	16
Control	1.3	1.3	1.3	1.2	1.2	1.2
Talc	2.4	1.9	3.0	3.0	1.3	3.6
Feldspar	5.1	1.9	6.3	4.1	3.8	5.8
Magnesium trisilicate	5.9	5.1	0.4	6.6	6.2	7.5

DAI–Days after inoculation; glucose @ 0.1%.

Table 3. Growth of *Bacillus megaterium* in silica medium in the presence and absence of CO_2.

Treatments	0 DAI		8 DAI		16 DAI	
	SiO_2 (mg l^{-1})	Bacterial count $\times 10^6$	SiO_2 (mg l^{-1})	Bacterial count $\times 10^6$	SiO_2 (mg l^{-1})	Bacterial count $\times 10^6$
Silicic acid alone	2.3	14	3.2	5	3.4	49
Silicic acid + glucose 0.1%	2.3	14	2.8	4	3.7	67
Silicic acid-air devoid of CO_2	2.3	15	1.8	4	0.8	21
Silicic acid + glucose 0.1% +air	2.3	14	2.1	14	1.5	29

DAI–Days after inoculation; carbon as glucose @ 0.1%.

3. Results and Discussion

Dissolution of silica was observed in silicate containing medium and also in silicate containing glucose medium. The silicate solubilising bacterial isolates from different sources from talc, pond sediment, sugarcane field soil and river water belonging to the genera *Bacillus* and *Pseudomonas* solubilised magnesium trisilicate in vitro. Some of the isolates like talc, sugarcane field soil were characterised by 16S r RNA sequencing are found to be *B.flexus*, *B. megaterium*, *B. mucilaginosus*. *Bacillus* sp isolated from river water and pond sediment of solubilised more silica in carbon-free silicate medium than in glucose containing medium. It is likely that these organisms can thrive in river water and pond sediment with very low nutrient content which might have an inherent higher solubilisation potential than those isolated from other sources. The *Bacillus* sp isolated from talc and the field soil effectively solubilised silicate in the presence of glucose. The solubilisation by *Pseudomonas* sp was nearly the same with regard to the absence and presence of glucose (Table 1).

The *Bacillus megaterium* solubilised different silicate minerals like talc and feldspar (Table 2). However, solubilisation was relatively higher in magnesium trisilicate. A reduction in dissolved silica was observed in the initial stages of incubation. It is likely that this might be due to utilization of silica by the bacterium for its growth.

Bacillus mucilaginous was found to grow exclusively on silicate and in the absence of carbon source. Bacterial multiplication was observed in flasks, where the CO_2 was excluded (Table 3). This bacterium grows well in acid washed sand and silicic acid in the presence and absence of glucose. It is of interest to note that multiplication continued in silica was unabated, whereas in combination with glucose, the growth was arrested after initial multiplication (Table 4). The growth of bacteria on silicic acid and acid washed sand indicates their capability to utilize silica for its cellular build up (Table 5). All of these have conclusively shown that silica can serve as a substrate for the growth of bacteria. This has an environmental significance as the bacteria can survive on soil silicates even when utilizable carbon is absent. The retardation of growth in media containing both silica and glucose on prolonged incubation suggests that the acids formed might inhibit the growth of bacteria. Since organic acids were implicated in silicate dissolution [6] their accumulation might have limited its growth. Carbon and silicon are similar in structure and function and silicon is considered as an analogue of carbon. Both share several properties in common and the dioxides of both carbon and

Table 4. Growth of *Bacillus mucilaginosus* on pure sand and silicic acid with and without carbon source.

0 DAI		8 DAI		16 DAI	
	SiO_2 (mg l^{-1})	Bacterial count $\times 10^5$	SiO_2 (mg l^{-1})	Bacterial count $\times 10^7$	SiO_2 (mg l^{-1})	Bacterial count $\times 10^7$
Silicic acid alone	2.4	296	9.1	350	9.9	350
Silicic acid + glucose 0.1%	2.4	294	10.2	*	9.6	*
Sand alone	0.9	295	4.4	438	2.8	438
Sand+ glucose 0.1%	0.9	295	4.4	*	2.8	*

DAI–Days after inoculation.
*No viable cells.

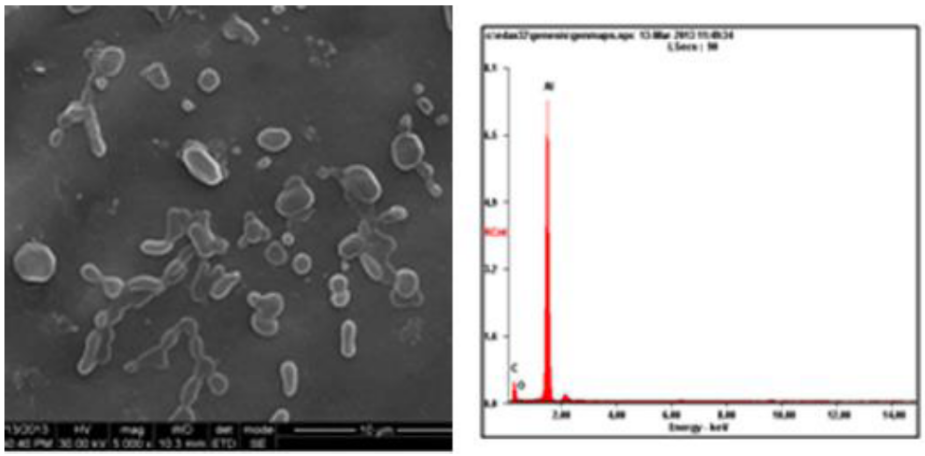

(a) Sand alone

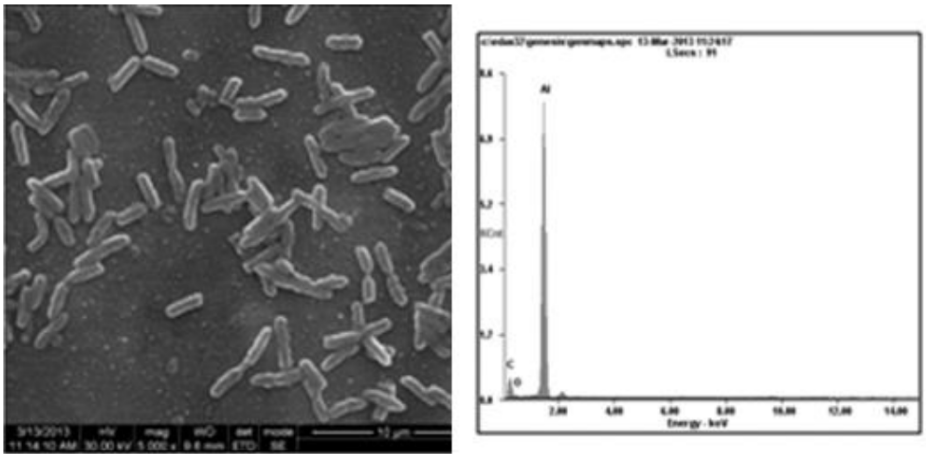

(b) Glucose alone

Figure 1. Bacteria grow under the presence and absence of carbon source the image shown with SEM with EDAX analysis (sand grown cells are slightly different in their morphology).

silicon are available in large quantities on this planet. But carbon alone forms the backbone of all organic forms. The utilisation of silicon for growth is observed in this study even though a slight morphological variation was observed in bacterial cells. The SEM with EDAX analysis also revealed the presence of carbon in bacterial cells which were grown in silica containing medium (Fig. 1). Although carbon compounds are abundant in living organisms and it is the basis for life, silicon compounds might have played a role in the development of primitive forms of life when earth was inhospitable for the development of carbon based life, as carbon compounds appeared very late.

Many living organisms are known to accumulate silicon since bacteria contain about 180 mg Si/kg of dry matter [7]. Silicon was found to exert a growth accerlating effect on bacteria [8]. Das and Chattopadyay [9]reported that

Table 5. Growth of *Bacillus mucilaginosus* on pure pulverized quartz in the presence and absence of any carbon source.

Treatments	0 DAI			3 DAI			7 DAI			10 DAI		
	pH	SiO_2	Bacterial count $\times 10^5$	pH	SiO_2	Bacterial count $\times 10^{16}$	pH	SiO_2	Bacterial count $\times 10^{20}$	pH	SiO_2	Bacterial count $\times 10^{20}$
Quartz	7.2	0.9	228	7.0	1.2	278	7.0	1.3	1256	7.0	0.69	206
Quartz+glucose 0.1%	7.2	0.8	227	3.0	0.6	572	3.0	0.6	43	3.0	0.41	*
Quartz+glucose 0.2%	7.2	0.8	227	3.0	1.9	203	3.0	0.6	30	3.0	0.60	*

DAI–Days after inoculation; SiO_2 expressed in mg l^{-1}.
* No viable cells.

Mycobacterium tuberculosis is capable of utilizing silicate facultatively in the absence of carbon. The formation of silicic acid in esterified cell wall of bacteria was also reported [9]. It is also likely that silicon might have been converted to carbon by biological transmutation or by nucleido – biological reactions which is common in life forms. The transmutation of potassium in chickens to meet their calcium requirement for egg shells by pecking up micas containing potassium is well known. The existence of biological transmutations is also well established [10,11]. The present study shows that gram positive *Bacillus* and gram negative *Pseudomonas* utilize silicate exclusively which is an immense significance in their ecological survival, where carbon compounds are lacking in the natural environment. In the search for extraterrestrial life on other planets also the phenomenon of utilising silicon *in lieu* of carbon becomes significant as the bacteria can occur in a carbon-free environment.

References

[1] H. Zhou, X. Zong, F. Liu, G. Qiu and Y. Hu,. Screening, identification and desilication of a silicate bacterium, *J. Cent. South Univ. Technol*. **3** (2006) 337–341.

[2] X.F. Sheng, F. Zhao, L.Y. He, G. Qiu and L. Chen, Isolation and characterization of silicate mineral solubilising *Bacillus globisporus* Q12 from the surfaces of weathered feldspar, *Can. J. Microbiol*. **54** (2008) 1064–1068.

[3] J.A. McKeague and M.G. Cline, Silica in soil solution I. the form and concentrations of dissolved silica in aqueous extracts of some soil, *Can J. Soil Sci*. **43** (1963) 70–82.

[4] N. Vasanthi, L.M. Saleena and S. Anthoni Raj, Concurrent release of secondary and micronutrient by a *Bacillus* sp, *American-Eurasian J. Agric and Environ. Sci*. **12** (2012) 1061–1064.

[5] K. Imaizumi and S.Yoshida, Edapinological studies on silicon supplying power of paddy soils, *Bull. Nat. Instt. Agric. Sci.* **8** (1958) 261–304.

[6] R.B. Duff and D.M. Webley, 2-*ketogluconic* acid as a natural chelator produced by soil bacteria, *Chem. nd Ind.* (1959)1376–1377.

[7] H.J.M. Bowen, *Environmental Chemistry of the Elements*, Academic Press, London, Vol. 7, 1979, p. 147.

[8] M. Tajirna, The effect of silicon on the growth of *Staphylococcus aureus*, *Nippon Jibiinkoka Gakkai Kaiho* **93** (1990) 630.

[9] S. Das and U.K. Chattopadhyay, 2000. Role of silicon in modulating the internal morphology and growth of *Mycobacterium tuberculosis*. *Ind. J. Tub*. **47** (200) 87–91.

[10] J.P. Biberain, Biological transmutations: Historical perspective, *J. Condensed Matter Nucl Sci*. **7** (2012) 11–25.

[11] C.L. Kervran, *Biological Transmutations*, Swan, New York, 1972, Michel Abehsera translator.

J. Condensed Matter Nucl. Sci. 17 (2015) 116–123

Research Article

Thermal Analysis of Explosions in an Open Palladium/Deuterium Electrolytic System

Wu-Shou Zhang*

Beijing National Laboratory for Molecular Sciences, Institute of Chemistry, Chinese Academy of Sciences, P.O. Box 2709, Beijing 100190, Republic of China

Xin-Wei Zhang

Institute of Applied Physics and Computational Mathematics, P.O. Box 8009, Beijing 100088, Republic of China

Da-Lun Wang, Jian-Guo Qin and Yi-Bei Fu

Institute of Nuclear Physics and Chemistry, China Academy of Engineering Physics, P.O. Box 213, Mianyang 621900, Republic of China

Abstract

An explosion occurred in an open Pd/D electrolytic system at a low current density of 62 mA cm^{-2}. The average power was greater than 6.7 W (65 W cm^{-3} Pd or 430% of input power), and the incubation time was less than half an hour before the explosion. Thermal analysis indicates that the power of the explosion was 5.1–5.5 kW (or 50–53 kW cm^{-3} Pd), and the event developed in 2–17 s. It is concluded that this explosion was most probably caused by low energy nuclear reactions taking place in the Pd tube cathode rather than by chemical reactions.
 ISSN 2227-3123

Keywords: Cold fusion, CMNS, Explosion, Pd/D electrolytic system, Pd tube, LENR

1. Introduction

Since anomalous heat was announced by Fleischmann and Pons [1], there has been a great deal of research on Pd/D electrolytic systems [2]. Some explosions in various types of electrolytic cells have been reported [3–6]. The accident at SRI International was the most famous one; it was determined that this explosion was probably caused by deuterium and oxygen recombination [3]. However, data from explosions occurring in other labs indicate that some rapid exothermic reactions rather than chemical processes induced these phenomena [4–6]. In a previous paper, we summarized three explosions in our Pd/D electrolytic experiments which occurred in April 1991 [4]. After similar events take place

*E-mail: wszhang@iccas.ac.cn/zhangwushou@hotmail.com; Tel.: 86-10-6255 4276; Fax: 86-10-6255 9373.

 ISSN 2227-3123

again and again [5,6], it becomes incumbent upon a researcher to pay attention and analyze the results in detail. We did this and found some interesting features, which are presented here.

2. Electrolytic Cell and Explosions

The electrolytic system included a measuring cylinder with spout and foot ($\phi_{\text{out}}25.5 \times \phi_{\text{in}}23 \times 186$ mm^3, 77 m1, made of simple glass, not heat-resistant glass); $\sim$ 0.4 M LiOD heavy water electrolyte ($\sim$ 39 m1 of D_2O with 0.3 wt.% of ^{6}LiD, $\sim$ 9.4 cm of liquid height); a Pd tube[a] (ϕ_{out} 1.67 $\times$ ϕ_{in} 1.07 $\times$ 80 mm^3, 0.103 cm^3, A_{out} = 4.20 cm^2, 1.3 g) cathode with the bottom end open, connected to a Ti wire lead inserted at the top end and mechanically clamped; a Pt mesh anode with a Pt wire lead, a round rubber plug platform holding the electrodes (ϕ_{top} 27 $\times$ ϕ_{bottom} 21 $\times$ 22 mm^3, 15.5 g) being inserted about 12 mm into the measuring cylinder for sealing, except a blowhole ($\sim$ ϕ 3 mm) to allow gas to escape freely, as shown in Fig. 1. Both the cathode and anode were immersed in the electrolyte before electrolysis. The cell was placed in a 1-liter glass beaker filled with 530 ml of light water, with the water level about 10 cm; the bath beaker was covered with a plastic annular lid. A thermometer was fixed at the lid; the sensor head of the thermometer was approximately halfway between the sidewalls of the electrolytic cell and bath beaker, and 2 cm above the beaker bottom, as shown in Fig. 1. The room temperature in the early morning of this season was 22°C; we will set this value as the bath temperature just before the explosion, because the record of the temperature was lost.

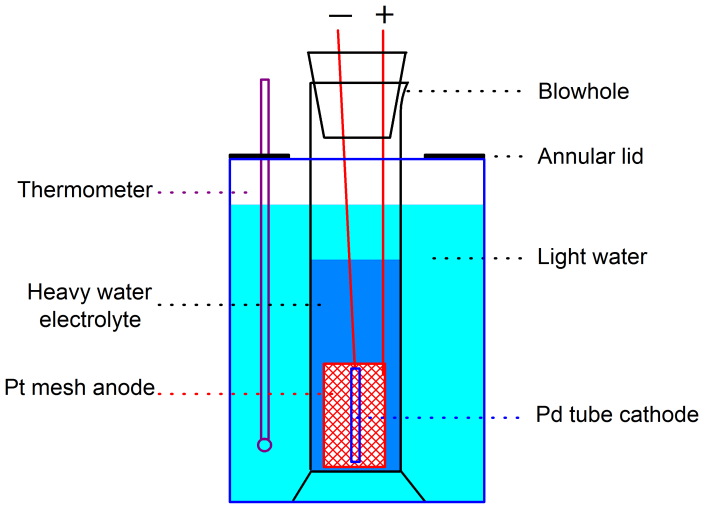

Figure 1. Schematic of experimental set-up.

Three explosions happened in this Pd/D electrolytic system in April 1991. In these explosions, the rubber plug with the electrodes in it flew off about 1.5–3 m away, and electrical wires and alligator clips used to connect the DC

[a]We measured the inner diameter of a Pd tube from the same batch as that used in this paper. It was 1.07 mm, and not 0.67 mm as listed in Ref. [4].

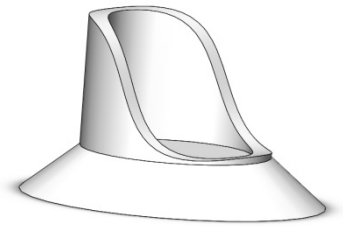

Figure 2. Artist's view of the fracture surface of the broken cell, based on memory.

power to the cell were left on the lab table. The ankle of cell broke as illustrated in Fig. 2. D_2O in the cell mixed with H_2O in the bath in the last case[b]. Because nobody was present at the scene of any of the explosions, there was no direct observation on any case except the last one having some records later as described below.

In the last event, the potentiostatic electrolysis with cell voltage of 7.5 V had continued for more than 50 h before the explosion. The applied current at the 50th hour of electrolysis was 0.26 A (or 62 mA cm^{-2}), which was slightly less than at the start. Voltage, current and bath temperature were manually recorded every hour and they were stable before the explosion. An experimenter (Da-Lun Wang) left the lab after the data recording at the 50th hour and came back half an hour later; the explosion took place during this period. It was found that the bath temperature had risen by 5°C. The rubber plug and the attached electrodes flew 2–3 m away and fell onto the floor. At the same time, one area in the middle-upper part of the Pd tube bulged out but the backside of this protruding section was not concave and the electrode was still as straight as before. This means this damage was not caused by any external force after the explosion but by an internal cause during the process. It was believed that the first two explosions were weaker than the last one because the cell remained intact and it only fell against the sidewall of the bath beaker in the first two. After these two cases, the plug was pressed firmly into the cell and this gave rise to a more violent explosion the third time. The last event will be discussed in detail.

3. Explosion Analysis

Firstly, we estimate the effect of electrolysis on thermal behaviors of this system. It is easy to determine that about 4.4 ml or 4.9 g of heavy water (a column of water in the cell $\sim$ 1.1 cm high) was consumed after 50 h of electrolysis; the height of electrolyte level in the cell was, therefore, 8.3 cm[c]. The heating power of electrolysis just before the explosion was: $P = I \times (U - 1.53\ \mathrm{V}) = 1.55$ W, where 1.53 V is the thermoneutral potential for D_2O electrolysis. The temperature difference across the cell wall was:

$$\Delta T = \frac{Pt}{\kappa S} = 0.32^{\circ}\mathrm{C} \ll 5^{\circ}\mathrm{C}, \tag{1}$$

[b]The statement that "the bottom of cell was blown out" in Ref. [4] is not accurate.
[c]However, it is not sure if the cathode broke the meniscus of heavy water or not because all parts of cell were lost in home moving of lab afterwards.

where $t = 0.125$ cm, the thickness of glass sidewall; $\kappa = 9$ mW cm^{-1} K^{-1}, thermal conductivity of glass; $S = 66$ cm^2, the conduction area of the sidewall with the height of electrolyte level (8.3 cm). Therefore, the electrolysis power did not heat up the cell to a significant temperature rise before the explosion.

Based on the above conclusion and temperature measurement, the minimum excess energy released before the explosion would be the absorption heat of 530 ml of water and 34.6 ml of heavy water with a 5°C temperature rise: ΔQ = 12 kJ. The heat dissipation after the explosion is omitted here.

Secondly, a simulation test conducted after the explosion showed that it takes 2.1 kgf to blow out the plug. This corresponds to an excess pressure Δp = 0.5 bar. That is to say, the minimum pressure in the gas column of the cell was 1.5 bar just before the explosion. Four possible situations might lead to such high pressure and explosion; we consider the first three of them trivial:

(1) **Blowout of sealed cell.** Provided the system was completely closed due to a mistake in the assembly process before electrolysis, the cell would explode due to inner pressure increasing. However, it would only have needed 7 min to attain the pressure of 1.5 bar, not the 50 h it actually took. Furthermore, the blowhole of the cell was clean without any deposit of solute. There was no process which could seal the cell during electrolysis and heat up the bath water effectively; therefore, the possibility that the cell was sealed can be excluded.

(2) **Chemical explosion by D_2 + O_2 recombination.** The volume of the gas column above the electrolyte in the cell head space just before the explosion was 38 cm^3, the related heat production ΔQ_{chem} can be calculated using the optimal D_2/O_2 mixing ratio:

$$\mathrm{D_2} + \frac{1}{2}\mathrm{O_2} = \mathrm{D_2O} + 294.6 \text{ kJ mol}^{-1},$$

ΔQ_{chem} = 0.31 kJ, which is much less than the actual value 12 kJ and could not heat up the bath water too. The following discussion also rules out the explosive recombination because the steam flow purged the D_2+O_2 mix. Therefore the real explosion could not be caused by any chemical reaction.

(3) **Short-circuit of electrodes.** This possibility can be excluded for three reasons. Firstly, the electrode leads were hard wires and connections of lead-electrode were strong; a short-circuit could not happen during electrolysis. Secondly, unlike what happens with utility AC power, a short-circuit of DC power would change the constant-voltage mode to the constant-current mode, and the supplied power would be lower than before; therefore, the heating power in the cell could not rise. Thirdly, even if the DC power supplied the cell with the maximum output power (e.g. several tens of watts), it could not reach 5.1–5.5 kW of thermal power, which is the amount deduced below.

(4) **Heat burst in the Pd tube cathode.** Because these prosaic reasons cannot explain the explosion, the only likely explanation was that a heat burst of low energy nuclear reactions (cold fusion) took place in the tube cathode; the released energy heated the heavy water to the boiling point and high vapor pressure developed in a short time; the vapor could not escape the cell effectively and the explosion occurred.

We can estimate that the minimum temperature rise in the cell just before the explosion was 75°C using parameters of the excess energy ΔQ = 12 kJ and the remaining electrolyte volume of 34.6 ml, provided the excess heat only transferred to the bath water of 530 ml (in other words, we assume it was adiabatic). Based on the initial temperature 22°C, the electrolyte would be greater than 97°C, very close to the boiling point of heavy water, 101°C. This also indicates that the electrolyte was boiling during the explosion.

The boiling point of heavy water is 113°C at a pressure of 1.5 bar [7][d]; the vapor density ρ = 0.966 mg cm^{-3} and

[d]The boiling point of electrolyte shifted upward 0.45°C due to 0.4 M LiOD is neglected here to be conservative [8].

vaporization heat $\Delta H = 2012$ J g^{-1} correspondingly. Based on Bernoulli's law, the steam velocity escaping through the cell's blowhole in such conditions is

$$\nu_{\text{hole}} = \sqrt{\frac{2\Delta p}{\rho}} = 330 \text{ m s}^{-1}. \tag{2}$$

This value is close to the speed of sound in air. The explosive power can be estimated by two methods: one is the kinetic calculation described previously [4] and the other is a thermal transfer analysis here.

There are two limits, one is the adiabatic approximation, i.e. the excess heat was produced so fast that the heat loss was only carried by the steam across the blowhole; the corresponding power is

$$P_{\text{ad}} = \frac{\pi\phi_1^2\rho\nu_{\text{hole}}}{4}\Delta H_{T_0\to T} \tag{3}$$

with $\Delta H_{T_0\to T} = 2264$ J g^{-1}, the enthalpy change of D_2O from liquid at 22°C (T_0), 1 bar to vapor at 113°C (T), 1.5 bar [7]. Using parameters ϕ_1 = 0.3 cm, ρ = 0.966 mg cm^{-3} and v_{hole} = 330 m s^{-1}, we obtain the steam power through the blowhole is

$$P_{\text{ad}} = 5.1 \text{ kW}. \tag{4}$$

Another limit is the isothermal approximation, i.e., the assumption that the temperature rise of the cell was so slow that a stable temperature distribution was reached between the cell and its environment, and the temperature field in the cell was uniform. With this approximation the thermal power just before the explosion would be

$$P_{\text{iso}} = \frac{\pi\phi_1^2\rho\nu_{\text{hole}}}{4}\Delta H + \alpha A(T - T_0). \tag{5}$$

The first term on the right-hand side of Eq. (5) is similar to Eq. (3) except $\Delta H_{T_0\to T}(2.246$ J g$^{-1})$ being replaced with the vaporization heat ΔH (2 012 J g^{-1}) at 113°C and 1.5 bar, it is 4.5 kW. The second term on the right-hand side of Eq. (5) is the cell's convection heat loss on the outer surface of sidewall immersed in water with area A = 80 cm^2, T = 113°C and T_0 = 22°C. α is the heat transfer factor:

$$\alpha = cRa^n\frac{\alpha}{h}, \tag{6}$$

where the constants c and n depend on the magnitude of Rayleigh number *Ra* [9]:

$$Ra = \frac{g\beta(T - T_0)h^3}{\nu\alpha} \tag{7}$$

with the gravitational acceleration g = 979.75 cm s^{-2}, the height h = 10 cm and water's parameters at temperature of $(T + T_0)/2$ [10,11]: the thermal expansion coefficient $\beta = 5.61 \times 10^{-4}$ K^{-1}, the kinematic viscosity $\nu = 4.32 \times 10^{-3}$ cm^2 s^{-1}, the thermal conductivity λ = 6.65 mW cm^{-1} K^{-1} and the thermal diffusivity $\alpha = 1.62 \times 10^{-3}$ cm^2 s^{-1}. We obtain the Rayleigh number *Ra* = 7.3×10^9. The corresponding constant are c = 0.1 and n = 1/3 for $10^9 < Ra < 10^{13}$ [9]. The heat transfer factor is α = 0.129 W cm^{-2} K^{-1} and the convection power in water is 960 W. On the other hand, the convection power in air is only 0.3 W and radiation power is only 11 W, we neglect them consequently. Therefore the thermal power just before the explosion under the isothermal approximation is

$$P_{\text{iso}} = 4.5 + 0.96 \approx 5.5 \text{ kW}. \tag{8}$$

These two different estimations give close amplitudes of explosion intensity; the actual power should be a value between these two approximations

$$P = 5.1 \text{ to } 5.5 \text{ kW}. \tag{9}$$

The explosion power density is

$$\frac{P}{V_d} = 50 \text{ to } 53 \text{ kW cm}^{-3} \text{ Pd}, \tag{10}$$

where V_{Pd} = 0.103 cm^3, the volume of Pd tube. Of course, this is only the minimum amplitude provided that the rate of anomalous reaction was uniform in the whole sample. Because of the localization characteristic of excess heat production as observed that one area of the Pd tube being strongly distorted after the explosion (see Section 2), the actual power density should be much greater than the value in Eq. (10). Considering the reaction region was confined in a length equal to the diameter of the Pd tube, the corresponding volume is 2.2×10^{-3} cm^3, then the local explosive power density is

$$\frac{P}{V_{\text{Pd . local}}} = 2.3 \text{ to } 2.5 \text{ MW cm}^{-3} \text{ Pd}. \tag{11}$$

Of course, the above values only characterize the explosive phase. It needs time to warm the cell from the bath temperature to the boiling point; we can estimate the lower limit of time for excess heat accumulation from total heat and the explosion power with the adiabatic approximation

$$t > \frac{\Delta Q}{P_{\text{ad}}} = 2.4 \text{ s}. \tag{12}$$

However, the electrolyte would boil away under this high power in a short time; we can estimate the time to boil dry is

$$t_{\text{dryout}} = \frac{m\Delta H_{T_0 \to T}}{P_{\text{ad}}} = 17 \text{ s} \tag{13}$$

with m = 38 g, the mass of electrolyte at 50 h of electrolysis. This means that a high power in the order of kilowatts could not continue for tens of seconds; otherwise, the cell would dry out and explosion would not occur. The time of thermal run-away should be

$$2.4 \text{ s} < t_{\text{run-away}} < 17 \text{ s}. \tag{14}$$

Referring to Mizuno's explosion [5], the developing time of cell's temperature increase from the ambient value to the boiling point was only $\sim$ 17 s. It seems the corresponding time in our cases also is in the same order of magnitude.

The upper limit of incubation time should be half an hour as described in Section 2. Using this time scale, we obtain the lower limit of excess power is 6.7 W or 430% of input power, the corresponding power density is

$$\frac{\bar{P}}{V_d} = 65 \text{ W cm}^{-3} \text{ Pd}. \tag{15}$$

4. Discussion

We can reconstruct the explosion process based on the above analysis. We can infer that the explosive process was probably caused by low energy nuclear reactions. At first, one local region of Pd tube electrode met some unknown criteria to produce intense cold fusion. The exothermic reaction released energy and heated up the cathode and the surrounding electrolyte. The positive feedback between temperature and reaction rate promoted the excess power to increase exponentially with time. After about ten seconds, the excess power was so great that the temperature at the nuclear reaction region (< 1 mm^3) of Pd tube rose to more than one thousand Celsius degrees and the metal lattice distorted strongly as observed afterwards due to thermo-stresses; the surrounding heavy water vaporized, and the electrolyte boiled. When the excess power was so high that the cell produced steam which could not escape through the cell's blowhole efficiently, the inner pressure rose rapidly and exceeded the threshold value, 1.5 bar. At that moment, the excess power reached 5.1–5.5 kW. The explosion followed: The plug was ejected, the D_2O temperature dropped instantly from 113 to 101°C, the ankle of cell was broken due to thermo-stresses in the wall of cell as illustrated in Fig. 2. All three of these processes happened at almost the same time, so we will not deal with them separately. The remaining electrolyte in the cracked cell mixed with the water in the bath and the mixture's temperature rose by 5°C. It must be pointed out that because some hot heavy water escaped in the form of vapor as shown in Eqs. (3) and (5), the value of 12 kJ is an underestimate of the actual energy release. On the other hand, although the D_2O bubbles probably ejected liquid out of the cell, which might fall back in the water bath; however, this effect only slightly modified the overall heat of 12 kJ, but it did not qualitatively changed the conclusion.

When we review this explosion 24 years later, it reveals more details that were omitted at that time.

Firstly, the system was operated at a current density of 62 mA cm^{-2}, which was lower than the well known threshold value of 100–150 mA cm^{-2} for excess heat production [2]. Excess heat at low current densities of 44–53 mA cm^{-2} were also reported by one of the authors 9 years after this explosion [12]. These facts indicate the requirement of current density for excess heat production may be lower than previously thought.

Secondly, although the loading ratio of deuterium in the cathode was not measured in this experiment, the D/Pd was probably not high for two reasons: (i) The current density applied here was less than in most cold fusion experiments that produce excess heat; (ii) The tube cathode had only the outer surface polarized during electrolysis. The inner surface had much low current density due to deuterium gas formation and high resistance of electrolyte in the tube. This means that deuterium absorbed on the outer surface would be desorbed on the inner surface. Therefore, the loading ratio of deuterium in the tube electrode was probably less than that of a solid electrode with the same area of outer surface. These facts may indicate that the threshold value of the loading ratio for excess heat production is not a necessary condition as reported later [12].

After these explosions, a video recorder was installed to monitor the electrolytic cell and obtain more information on explosions. However, no explosion ever occurred after that.

Obviously, the explosion here is similar to that in a W–H_2O electrolytic system observed by Mizuno [5]. The same features are the prominent excess heat and probably the rapid development time.

There was also an explosion in a Pd/D electrolytic system at SRI International [3]. Because it was a closed system and parameters are complex, we cannot reach a clear conclusion as here. Biberian reported the explosion in a similar open Pd tube/D electrolytic cell at low current [6]; we tend to conclude this was the same event as we experienced.

Acknowledgments

Thanks to Jed Rothwell, Profs. J.-P. Biberian and J. Dash for valuable discussions. Thanks to the referee for important and detailed advices. Thanks to Ms. Haina Zhao for the illustrative drawing. This work was supported by NSFC (21153003, 20973185) and 973 program of MOST in China (2009CB226113).

References

[1] M. Fleischmann, S. Pons and M. Hawkins, *J. Electroanal. Chem.* **261** (1989) 301; errata, *J. Electroanal. Chem.* **263** (1989) 187.

[2] E. Storms, *The Science of Low Energy Nuclear Reaction*, World Scientific, Singapore, 2007.

[3] S.I. Smedley, S. Crouch-Baker, M.C.H. McKubre and F.L. Tanzella, *Proc. 3rd Int. Conf. Cold Fusion*, Nagoya, Japan, Oct. 21–25, 1992; *Frontiers of Cold Fusion,* H. Ikegami (Ed.), Universal Academy Press, Tokyo, Japan, 1993, p. 139.

[4] X.-W. Zhang, W.-S. Zhang, D.-L. Wang, S.-H. Chen, Y.-B. Fu, D.-X. Fan and W.-J. Chen, *Proc. 3rd Int. Conf. Cold Fusion*, Nagoya, Japan, Oct. 21–25, 1992; *Frontiers of Cold Fusion,* (H. Ikegami (Ed.), Universal Academy Press, Tokyo, Japan, 1993, p. 381.

[5] T. Mizuno and Y. Toriyabe, *Proc. 12th Int. Conf. Cold Fusion*, Yokohama, Japan, Nov. 27–Dec. 2, 2005; *Condensed Matter Nuclear Science*, A. Takahashi, K.-I. Ota and Y. Iwamura, (Eds.), World Scientific, Singapore, 2006, p. 65.

[6] J.-P. Biberian, *J. Condensed Matter Nucl. Sci.* **2** (2009) 1.

[7] http://nuclear.ntua.gr/apache2-default/codes/heavy_calculus.html.

[8] M.H. Miles, H.D. Arman, J.D. Carrick, C.K. Gren, K.A. Haggerty, H.Y. Kim, A.G. Ky, J.E. Markham, C.F. Meeks and D.E. Noga, *Proc. 9th Int. Conf. Cold Fusion*, Beijing, May19–24, 2002, p. 246.

[9] C.Y. Warner and V.S. Arpaci, *Int. J. Heat and Mass Transfer* **11** (1968) 397.

[10] U. Grigull, J. Straub, P. Schiebener (Eds.), *Steam Tables in SI Units*, 2nd Edn., Springer, Berlin, 1984.

[11] http://www.engineeringtoolbox.com/water-thermal-properties-d_162.html

[12] Z.-L. Zhang, W.-S. Zhang, M.-H. Zhong and F. Tan, *Proc. 8th Int. Conf. Cold Fusion*, Lerici (La Spezia), Italy: Italian Physical Society, Bologna, Italy, 2000, p. 91.